GROWTH, CHARACTERIZATION AND LASER PROCESSING OF HGMNTE AND OTHER NOVEL, MERCURY-TELLURIDE BASED SEMICONDUCTORS

Frederick G. Moore
B.A. Physics -- B.A. Mathematics
Lewis and Clark College, 1983

A dissertation submitted to the faculty
of the Oregon Graduate Center
in partial fulfillment of the
requirements for the degree
Doctor of Philosophy
in
Applied Physics

January, 1989

The dissertation "Growth, Characterization and Laser Processing of HgMnTe and Other Novel, Mercury-Telluride Based Semiconductors" by Frederick G. Moore has been examined and approved by the following Examination Committee:

Russell E. Kremer, Advisor
Adjunct Associate Professor
Crystal Specialties

John C. Abele
Adjunct Associate Professor
Lewis and Clark College

Paul R. Davis
Professor

Rajendra Solanki
Associate Professor

ACKNOWLEDGEMENTS

Thanks go to a number of people who were directly involved with my research and writing of this tome. To Russ Kremer and John Abele for their support, assistance and timely readings of numerous drafts of this document. Lisa Sargent and John Hunt were of significant help as was Jerry Boehme whose patience and expertise helped me through several panic-stricken incidents of equipment failure. The library staff was particularly helpful and routinely performed miracles in obtaining (translated) versions of articles that appeared in obscure Soviet and Czechoslovakian journals. Harry Dietrich (Naval Research Labs) and the people at the National Research Council provided the carrot which motivated me to complete this task in a reasonable time-frame. Special thanks go to Yuan Tang for his help with Hall measurements. Lastly, I wish to thank my wife Sara, to whom this dissertation is dedicated, for her moral support, sense of humor and periodic reality checks. I could not have accomplished this without her.

To Sara

Table of Contents

List of Figures

List of Tables

ABSTRACT

GROWTH, CHARACTERIZATION AND LASER PROCESSING OF HGMNTE AND OTHER NOVEL, MERCURY-TELLURIDE BASED SEMICONDUCTORS

Frederick G. Moore, Ph.D.

Oregon Graduate Center, 1989

Supervising Professor: Russell E. Kremer

$Hg_{1-x}Cd_xTe$ is the material of choice for fabrication of infrared detectors in the 8-14 μm and 3-5 μm regions. Alternative approaches to growth and processing, and alternative Hg-Te based materials offer promise for easier fabrication, and possible superior performance of infrared detectors. An investigation was undertaken to study the application of laser processing techniques to several alternative Hg-Te materials and HgCdTe.

Bulk growth of HgATe (A = Cd, Mn, Mg, Ca, Sr, Ba, Be) produced material for subsequent investigation. Samples were prepared and then underwent initial characterization including mass density measurements, X-ray measurements of lattice parameter, FTIR measurements of bandgap, Hall and resistivity measurements, and a novel surface measurement based on the Seebeck Effect giving information about carrier type, density and mobility.

Representative samples were annealed in a mercury overpressure to reduce the density of mercury vacancies. Hall measurements done on samples tracked changes in electrical properties caused by these anneals. Samples were then exposed to a CW CO_2 laser in a study giving mercury loss as a function of exposure time, and laser power. Mercury loss was measured directly using EDX techniques and indirectly using a reflectivity experiment detecting the onset of surface melting which corresponds to the onset of significant mercury loss.

Samples attached to a LN_2 stage and exposed to the laser for extended periods experienced electrically significant mercury diffusion laterally within the material. This relocation was measured qualitatively with the aforementioned Seebeck technique and is correlated with theoretical models of temperature rise during laser exposure, and to sample preparation procedures.

Using data obtained from mercury loss and diffusion studies, a laser annealing procedure was developed for use on ion implanted samples of HgMnTe. Hall measurements were done before and after implantation and an improvement in the electrical properties of the implanted/annealed layer was documented.

The materials investigated are finally compared with regard to lattice parameter, dE_{gap}/dx relationships, Hall data and reflectivity/mercury loss data. This information is compared against similar information obtained for HgCdTe and the relative strengths and weaknesses detailed.

CHAPTER 1

Introduction

1.1 Background

The practical applications of II-VI HgTe based ternaries, apart from their interesting physical properties, have made the family the focus of much attention. The general composition of these compounds is denoted $Hg_{1-x}A_xTe$ with $0 \leq x \leq 1$ or more briefly HgATe, where A is typically, though not always, a member of column II of the periodic table. The best known of these materials is HgCdTe which has become the workhorse in much of infrared detection technology. Cadmium is completely miscible in HgTe[1] and by adjusting the composition the bandgap of the resulting material will range from that of CdTe, $E_g^{CdTe} \approx 1.6eV$ to that of HgTe, $E_g^{HgTe} \approx -0.3eV$.[2] With a negative bandgap energy at most temperatures and pressures HgTe is thus a semimetal. The practical upshot of this, is that infrared detectors may be fabricated out of a material whose peak response can be adjusted over a wide range of wavelength by varying the parameter x. The range of bandgap energies available in HgCdTe corresponds, using the standard relationship, $E_g = \frac{hc}{\lambda}$, to a wavelength range from $\lambda = 0.5\mu m$ to $\lambda = \infty$, the former corresponding to $x = 1$ (CdTe), and the latter to $x \leq 0.07$ (semimetallic HgCdTe with $E_g \leq 0$).

The fabrication of devices from HgATe compounds, has reached a high level of complexity. Hybrid arrays of photovoltaic and photoconductive sensors are commonly produced[3,4] and set industry standards for performance. The production of these devices requires high quality starting material and control over its electrical properties. Other processing requirements include the fabrication of p-n junctions and the application of contacts. The large mercury concentration in these materials along with the ionicity of CdTe[5] complicates what, in silicon or even gallium-arsenide, would be standard procedures.

HgCdTe is mechanically weak and suffers from a loss of mercury at even slightly elevated temperatures or in vacuum.[6,7] The vapor pressure of mercury rises rapidly with temperature, as shown in figure 1-1.[8] Bulk growth furnace temperatures of between 650C and 800C are commonly used, resulting in pressures as high as 100 atmospheres. This is one reason that large diameter samples of bulk material cannot be produced. Larger ampoules, typically quartz, cannot withstand the large internal pressures.

The traveling heater method, which uses lower growth temperatures has been seen to be promising[9] and has produced 30-40 millimeter diameter ingots with good uniformity. Still, segregation, both radial and axial have been documented in HgCdTe[10] as well as HgMnTe.[11,12] Tellurium precipitates are also a problem in the bulk growth of HgCdTe.[13-15]

There has been work done indicating that the already weak Hg-Te bond is further weakened by the addition of cadmium.[16,17] This results in mercury

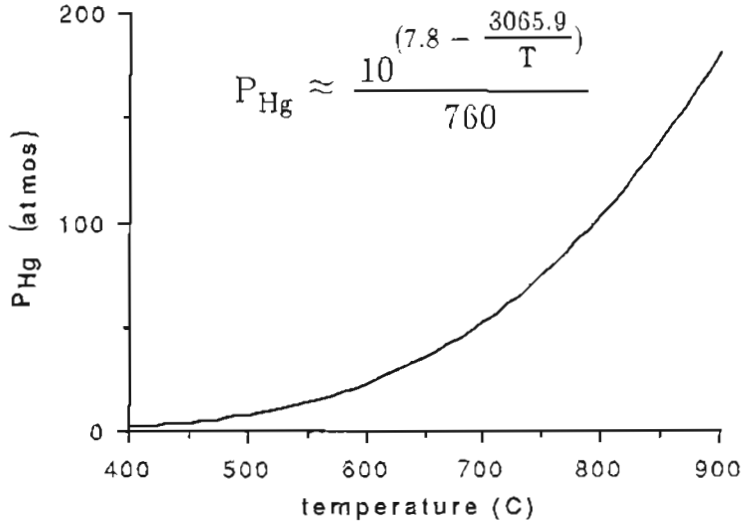

Figure 1-1 Vapor pressure of mercury as a function of temperature including the range over which HgATe bulk growth occurs. Typical temperatures for these growths are between 650-800 degrees, corresponding to pressures between 30 and 100 atmospheres.

vacancies being the dominant point defect.[5,18] Similar research shows that the addition of other elements, for instance zinc, in the place of cadmium will actually strengthen the Hg-Te bond.[17] Unfortunately, theoretical work still lags far behind experiment with II-VI materials. Further, the semi-analytical methods used for calculating bond strengths are ill suited for other materials such as HgMnTe.

Manganese has a partially filled D shell. These electrons, spatially confined to the vicinity of occupied manganese sites in the lattice, interact strongly with the valence electrons and complicate what would otherwise be a manageable analysis. These complications are especially important in light of theoretical predictions relating to several II-VI materials including HgCdTe.[2] This recent work suggests that even a material having a filled D shell, for example cadmium in HgCdTe, influences the material's overall bandstructure by way of its D orbital electrons. Thus the electronic properties of HgCdTe are influenced not only by its valence electronic structure but also by what are normally considered to be core electrons.

1.2 Scope

A number of alternative materials have been proposed to HgCdTe. With some of them associated properties such as magnetic behavior[19-21] offer the potential for new classes of applications. None of the alternative II-VI materials are as well understood as HgCdTe, undoubtedly some never will be. Still there exists the potential for developing materials that, for some applications, may prove superior to HgCdTe. Table 1-1 gives a collection of

information compiled from a variety of sources[22-25] about the materials that will be included in this investigation. Notice that only two of the materials besides HgTe occur naturally in the zincblende structure. CdTe, one of these binaries has a lattice parameter close to that of HgTe, while the little studied binary BeTe[26] has a lattice parameter significantly smaller than HgTe. Two other materials, MgTe and MnTe tend to the wurtzite structure. Investigations of HgMnTe[23] have managed to predict a psuedo-zincblende lattice parameter for MnTe, a_o, by extrapolating $a_o(x)$ of the ternary HgMnTe to the extreme of $x=1$ and this value is given as 6.34 Å. The same work has shown that HgMnTe only forms good zincblende structure up to a composition of $x\approx 0.35$. The other nominally wurtzite material, MgTe, is thought to form zincblende material with HgTe up to $x\approx 0.2$. For HgMgTe, this investigation has, through bandgap and lattice parameter measurements, been able to deduce a psuedo-zincblende lattice parameter for HgMgTe having a value of 6.769 Å. Details of this latter determination are given in chapter three.

Lastly there are three materials naturally occurring in the NaCl structure. There is some disagreement as to the actual lattice parameter of these binaries. This is indicated by the multiple entries listed in table 1-1. Without knowing an effective zincblende lattice parameter for the binary material it is difficult to calculate material composition, or x-value, from density measurements. It is hoped that the last three materials will prove amenable to FTIR techniques, giving a measure of bandgap which in turn can be correlated to composition and thus used to generate a relationship for $\rho(x)$.

TABLE 1-1
Crystal Structure and Lattice Parameter
for Constituent Binary Compounds

material	crystal structure	lattice parameter (å)	reference
HgTe	Zincblende	6.462	22
CdTe	Zincblende	6.481	22
MgTe	Zincblende*	6.769	**
MnTe	Zincblende*	6.34	23
BeTe	Zincblende	6.54	24
MgTe	Zincite	a=4.52, c=7.33	22
MnTe	Zincite	a=4.09, c=6.70	24
BaTe	NaCl	6.986	24
		7.00	25
CaTe	NaCl	6.350	25
SrTe	NaCl	6.47	24
		6.66	25

*MnTe and MgTe do not occur in the ZnS structure naturally. These fictitious values are obtained by extrapolating $a_o(x)$ relationships in HgMnTe and HgMgTe to the extreme of x=1.

**This investigation, chapter three.

The materials of interest in table 1-1 fall into three basic categories:

- those that are not true II-VI materials: for example HgMnTe,
- those that are IIA-VI materials: for example HgMgTe,
- those that are IIB-VI materials: for example HgCdTe.

After HgCdTe the best known materials are HgMnTe and HgMgTe. Substantial literature is available on the first material, both in terms of its basic physical properties[19,20] and its application for infrared devices.[21] Somewhat less has been published on the latter material.[27,28] For the remaining materials containing calcium, beryllium, barium, and strontium only limited theoretical information is available on the binary telluride compounds.

There have been band structure calculations made for these binaries,[2,29,30] and except for BeTe, the remaining materials have substantially larger bandgaps than does CdTe. Moreover, their binary crystal structure, again excepting BeTe, is not zincblende.[24]

Predictions may be made as to their basic structural properties when formed as a psuedo-binary compound with HgTe. The lattice parameters for the binaries are given in table 1-1, and may be calculated for the compounds assuming Vegard's law[31] holds. The predicted bandgap relationship assumes a linear variation between the relationships for the two constituent binaries. Thus:

$$E_g^{HgATe}(x) = E_g^{HgTe} - \left(E_g^{HgTe} - E_g^{A}\right) \cdot x. \qquad 1.1$$

These relationships are presented in table 1-2 and again are from various sources.[2, 26-28]

Experimentally, in HgCdTe the bandgap variation as a function of composition can be modeled as a higher order polynomial,

$$E_g = a_0 + a_1 x + a_2 x^2 \cdots \qquad 1.2$$

Typically the ratio of the higher order coefficients to the linear coefficient are significantly less than unity. In the case of HgCdTe[32] we have:

$$\frac{a_2}{a_1} \approx 0.25 \, . \qquad 1.3$$

It will be assumed that for other materials the $E_g(x)$ relationship is, likewise, reasonably linear. HgMnTe is a good example of this and other considerations that will be made in working with lesser known alternative materials.

As already mentioned MnTe does not form in the zincblende structure. However, investigations suggest that HgMnTe does form good, zincblende material for $x \leq 0.35$.[19] With this in mind, one may develop a relationship $E_g(x)$ for HgMnTe valid only when $0 \leq x \leq 0.35$. Further, it is useful to use lattice parameter studies of $a_o(x)$ to extrapolate a lattice constant for MnTe ($x = 1$) supposing that it did form in the zincblende structure.[23] X-ray powder diffraction work to be described in chapter three will be used to do this for HgMgTe.

In device fabrication the composition and hence the bandgap of the material is fixed by the intended application. In this investigation comparisons are made between materials of (approximately) equivalent bandgap.

TABLE 1-2
Bandgap (E_g) of Binaries and $E_g(x)$ for Psuedobinaries

Material	E_g (eV)	Ref.	E_g HgATe (eV)	Ref.	(x_{max})	Ref.
HgTe	-0.3	2	-	-	-	-
CdTe	1.6	2	-0.3+1.82x	32	x=1	32
BeTe	1.49	26	-0.3+1.79x	26	-	-
MgTe	2.69	27	-0.11+2.8x	27	x=0.2	28
MnTe	3.34	20	-0.3+3.63x	20	x=0.35	20
BaTe	3.4	2	-0.3+3.7x	3	-	-
CaTe	4.1	2	-0.3+4.4x	3	-	-
SrTe	3.7	2	-0.3+4.0x	3	-	-

1.3 Information Desired

This investigation will focus on several basic material and electrical properties that are of practical interest in the design and fabrication of devices from a HgCdTe-like material. Potentially, some of the alternative materials may prove superior in some manner to HgCdTe.

Comparisons will be made on the basis of many considerations, several of these will include: ease of growth, mechanical strength, toxicity, stability during heating and during laser annealing, compatibility with ion implantation techniques, and the $E_g(x)$ and $a_o(x)$ relationships. The importance of each of these points will become apparent. Other material properties that become apparent only after device fabrication, such as detector noise will not be discussed since no detectors were fabricated.

1.4 Plan of Attack

Two common handicaps facing many scientific investigations are a lack of information and a lack of time. For several of the alternative materials to be investigated the literature furnishes nary a hint as to various basic physical properties such as thermal conductivity and density. Thus for some comparisons it is necessary to assume the alternative materials will behave approximately as their better known sister materials. The approximately linear bandgap versus composition relationship of $Hg_{1-x}Cd_xTe$ is an example of this. Because of it, and a similar behavior in HgMnTe,[19] it is assumed that other materials will also have an approximately linear relationship.

This reasoning will be applied to deduce other (unknown) physical and electrical properties and relationships.

While HgMnTe has been the focus of much interest[4,33,34] there remain many basic questions to be answered. For this reason and for the sake of being able to investigate one material about which something is known there will be a disproportionate amount of work done on HgMnTe.

Lastly, for reasons of economics and availability all of the material investigated has been produced in-house. This gives us the ability to track the progress of any sample from the point at which the ampoule was charged to the final characterization. This ability is an important one, especially in the initial investigations of new materials.

CHAPTER 2

Materials Growth

2.1 The State of the Art

As mentioned in the previous chapter, bulk growth of mercury ternaries is extremely difficult when compared with other semiconducting materials.[35] Standard and modified bulk growth techniques are often limited to boules on the order of a single centimeter in diameter, and thus may never be able to produce large enough samples for some device applications. Still, the equilibrium bulk growth processes, unlike much of the growth based on epitaxy, offers some unique advantages for producing material that may be used to divine more basic information about material properties. The electrical properties of bulk material tend to be superior to those of materials produced by epitaxy. Further, the equipment and associated techniques needed to produce novel HgATe materials do not differ substantially from those needed to produce more standard HgTe-based materials. Consequently, initial investigations are logically conducted with bulk material before an informed decision to develop epitaxial techniques can be made.

2.2 Ampoule Design, Preparation and Charging

Ampoules were fabricated using standard quartz tubing with a wall thickness of two millimeters. Figure 2-1 shows the prototypical shape of the ampoule. The first-to-freeze end incorporates the standard narrowing with the hope of generating a seed during initial cooling of the tip. A ground

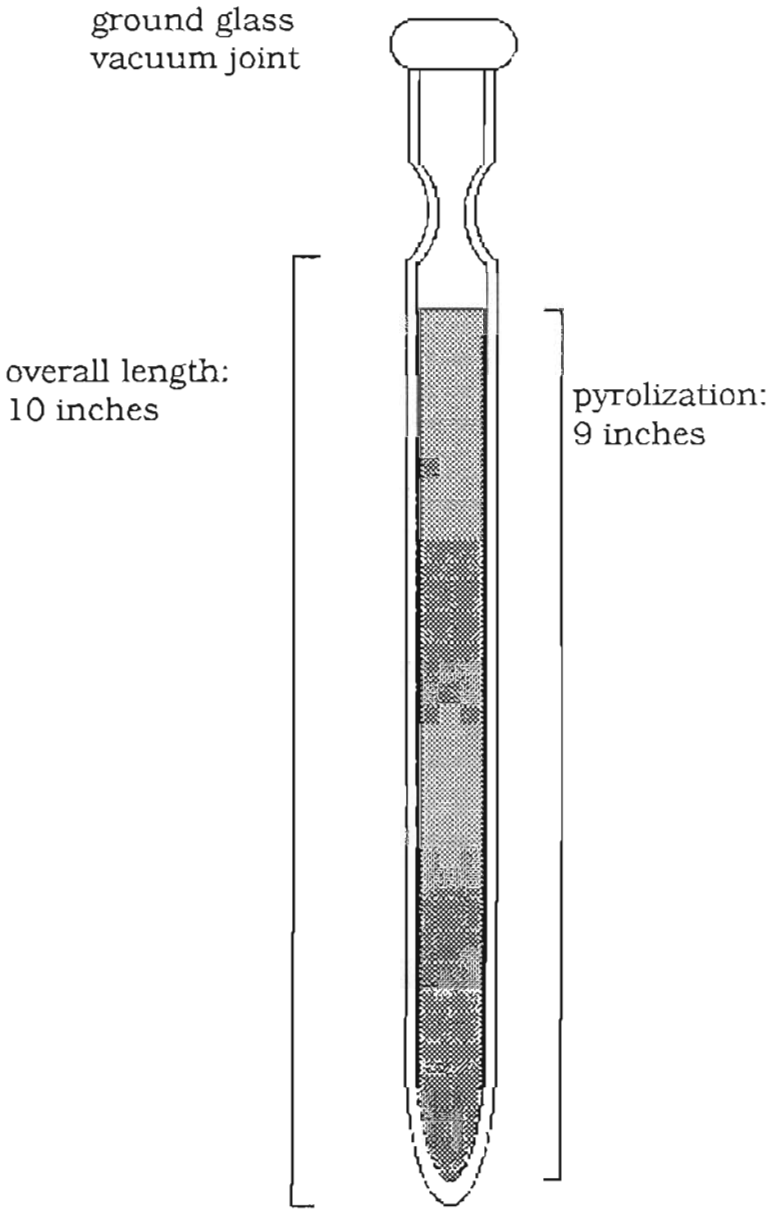

Figure 2-1 Prototypical shape and construction of quartz growth ampoules. Thick walled tubing is used, typical dimensions: inside diameter 10mm, outside diameter 14mm.

glass joint is affixed to the upper end of the tube and a pinched region is added to facilitate sealing the ampoule after it is charged and evacuated. An ampoule length, measured from the tip to below the pinched region, of nine to ten inches is normally satisfactory for a charge mass of 50-80 grams.

Prior to charging the ampoules were cleaned by:

- three washings in deionized water,
- three washings in aqua regia,
- three washings in methanol,
- drying at $\approx$ 80C for twenty minutes.

Because manganese is known to attack quartz at high temperatures[36] a layer of carbon was deposited on the inner surface of the ampoule. Figure 2-2 gives a diagram of the technique used to pyrolyze benzene within ampoules. A furnace capable of 1000C is needed, along with a roughing pump that can manage a 40-50 millitorr vacuum. The exterior of the ampoule is first cleaned with acetone to remove oils that can attack the quartz at high temperature, and then placed into the furnace. The ampoule is evacuated and the furnace ramped quickly to 1000C. The roughing valve is then closed and the benzene container is momentarily vented to the ampoule. After pausing a few seconds the roughing value is reopened and the ampoule evacuated. Repeating this process 30 to 40 times produces a satisfactory thickness of carbon. The ampoule must be cooled to room temperature slowly (8-10 hours) and while under continuous vacuum. When

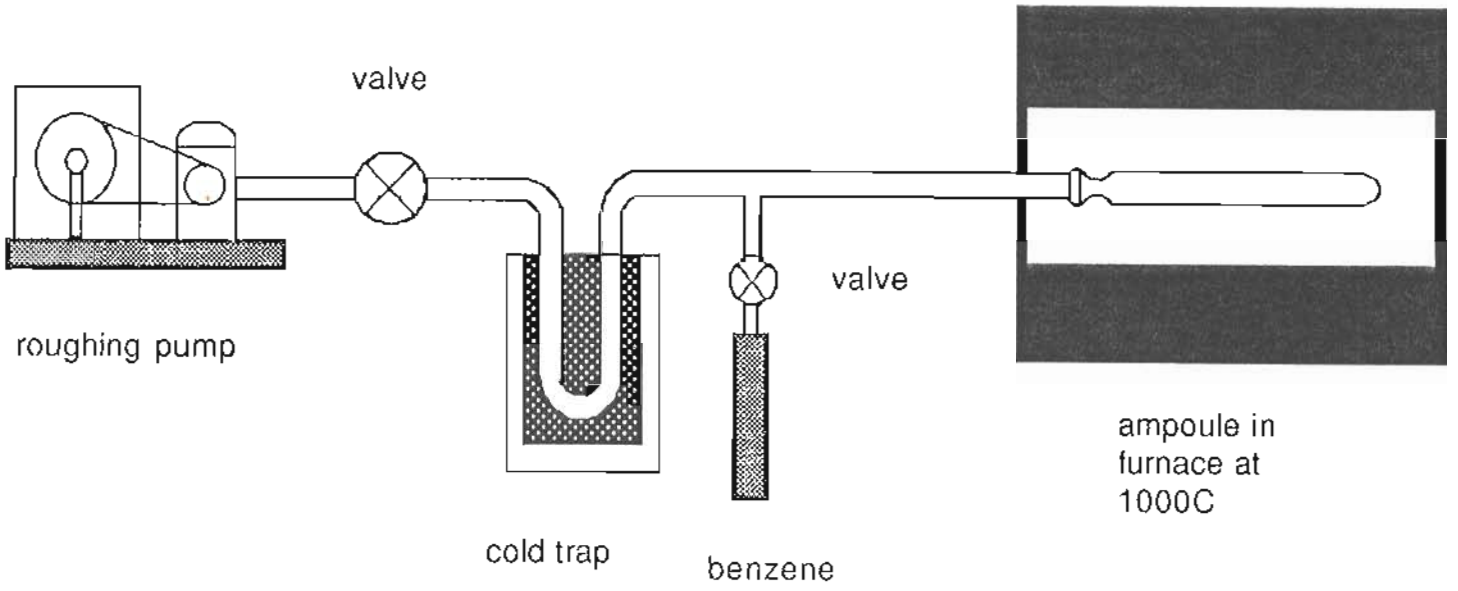

Figure 2-2 Pyrolization system used to deposit a layer of carbon on the interior surface of growth ampoules. A series of 30-40 ventings of benzene into the evacuated ampoule produces a satisfactory thickness of carbon.

rapid cooling was attempted carbon layer was observed to separate from the quartz. Further, the presence of air at elevated temperatures will remove the carbon.

The pinched region of the ampoule must be free of carbon to assure a good seal. Excess carbon can be removed by blowing air into the ampoule while heating the regions of excess carbon with a hydrogen-oxygen torch. At this point the ampoule is ready for charging.

Typical purities of starting materials are given in table 2-1. Starting masses of the constituent materials were calculated based on the desired x value of the growth. If the atomic masses of the materials are given by M_{Hg}, M_{Te} and M_A, where A is, for example manganese, and the desired total mass of the final ingot is M_T then the starting masses of each element are:

$$\text{Hg: } \frac{M_{Hg}}{M_T}\cdot(1-x), \quad \text{A: } \frac{M_A}{M_T}\cdot(x), \quad \text{Te: } \frac{M_{Te}}{M_T}\ . \tag{2.1}$$

These masses are obtained by weighing the materials on an electronic balance with a resolution of 100μg. The surface tension of mercury makes it difficult to obtain the desired amount. Thus it is advisable to get as close as possible to the calculated amount of mercury and then recalculate the masses of the other two elements based on the actual amount of mercury added to the ampoule. Portions of the other two materials can be added alternately to produce a layered arrangement that should result in better initial homogeneity during growth.

The toxicity of mercury, cadmium, strontium and especially beryllium

TABLE 2-1

Purity, Sources and Forms of Starting Material

Material	Purity	Source	Form
Tellurium	99.9999	Cerac	1/8 in. pieces
Mercury	99.99999	Aesar	liquid
Calcium	99.5	Aesar	1-10 mm shot
Beryllium	99.5	Aesar	powder
Barium	99.99	Cerac	granules ($\simeq$ 8 mm)
Magnesium	99.99	Cerac	1/8 in. pieces
Manganese	99.995	Metron	1/8 in. pieces
SrTe	99.5	Cerac	powder
Cadmium	99.9999	Metron	shot

Larger forms of starting material (shot or pieces) are less desirable than smaller ones. These large sections are awkward to load into the ampoule and with them it is difficult to obtain the desired starting mass to the necessary accuracy.

should not be underestimated. Standard references are available[37,38] and should be consulted and the appropriate precautions taken. Beryllium metal is perhaps the most dangerous of the constituent materials, and since it is normally obtained as a powder the inhalation hazard is particularly acute.

Figure 2-3 is a sketch of the arrangement used to seal charged ampoules. The ampoule is cooled in a dewar of nitrogen to reduce the vapor pressure of mercury. A diffusion pump is used to obtain a vacuum of $2-3 \times 10^{-6}$ torr. The ampoule is then quickly removed from its dewar and the pinched region of the ampoule heated with an oxygen-hydrogen flame and carefully sealed. Lastly the ampoule is again cleaned with with acetone, placed on a quartz holder and aligned within the growth furnace.

2.3 Furnace Considerations

Modified vertical Bridgman (moving furnace), Stockbarger (moving ampoule) and gradient freeze systems were used to provide the temperatures and temperature gradients necessary for growth. Figure 2-4 shows a side view cut-away of a Bridgman system typical of the ones used. The gradient freeze technique was abandoned early-on and the furnaces converted to a Stockbarger system. After several growths producing materials not used in this investigation a HgTe growth was attempted in the Stockbarger system, but with an ampoule having a internal diameter of 1.6 centimeters, and a wall thickness of two millimeters. The ampoule failed catastrophically and the resulting explosion severely damaged both furnace zones. Repairs were made but no more growths were completed using this system.

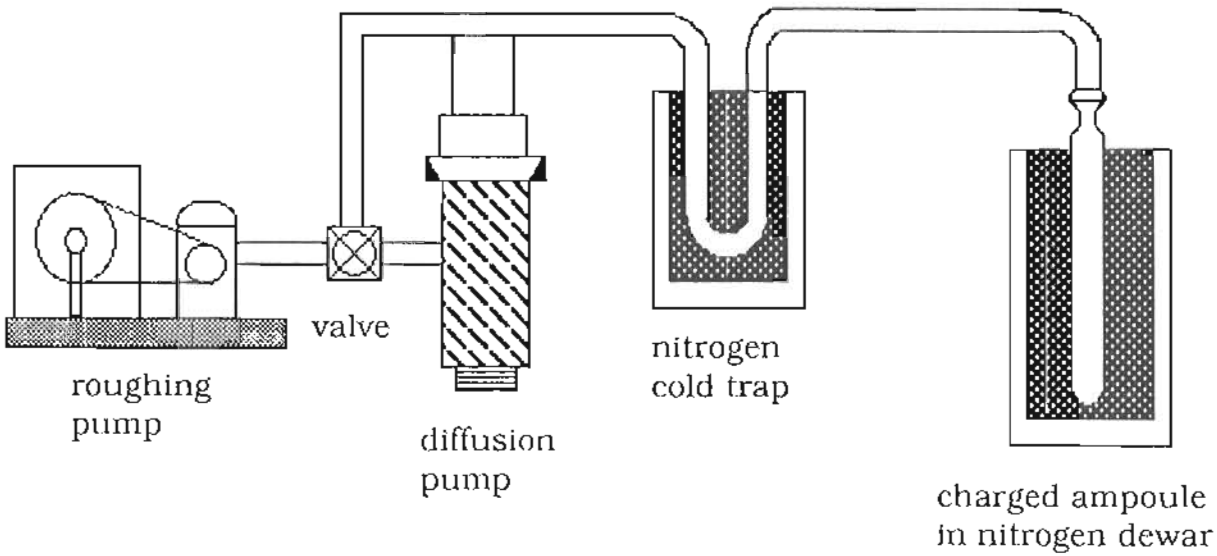

Figure 2-3 Ampoule-sealing system used to evacuate and close charged ampoules. Cooling the ampoule reduces the vapor pressure of mercury. Ampoules are typically evacuated to 2-4 micro-torr before sealing.

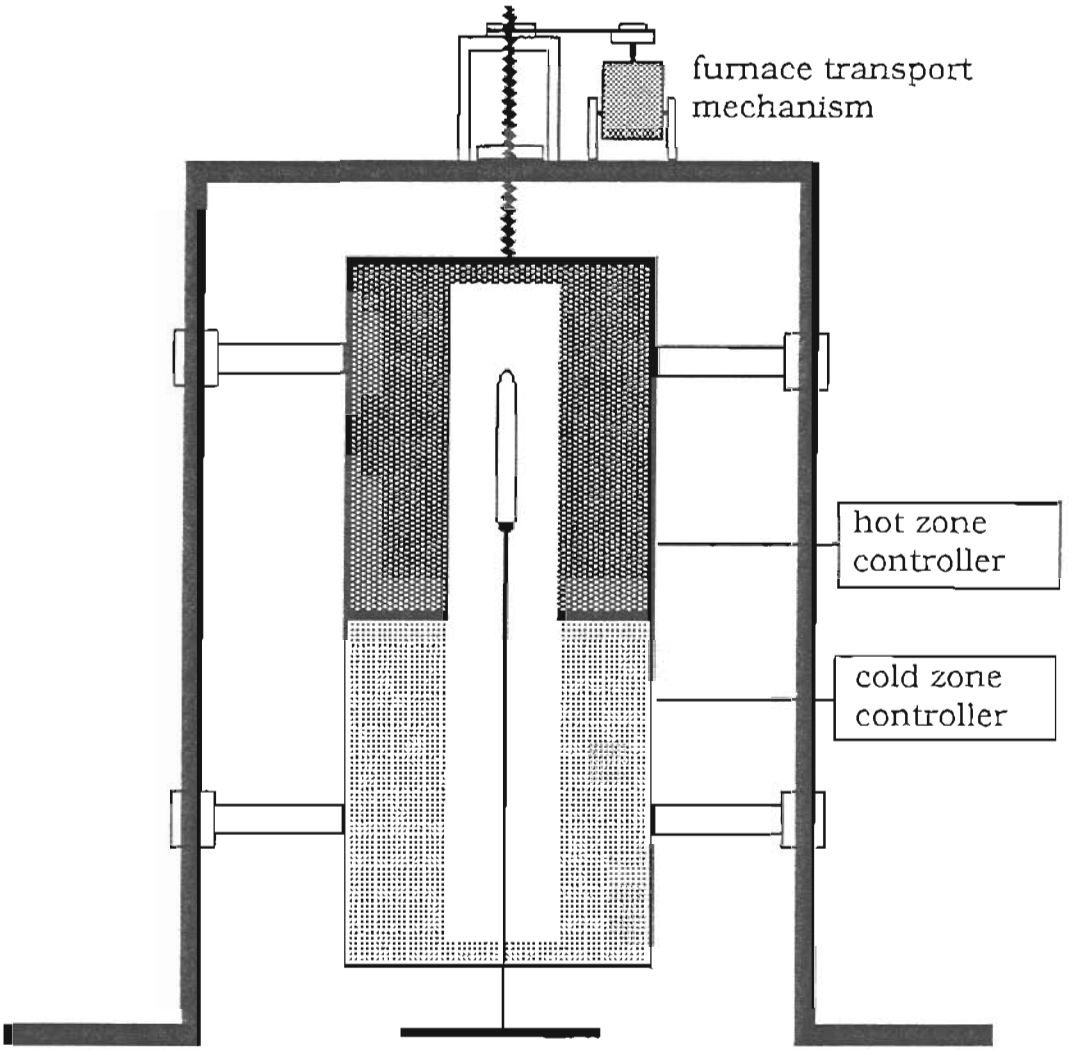

Figure 2-4 Sketch of Bridgman growth system used to produce bulk HgATe materials. This diagram is not to scale. the actual systems have range-of-motions of 60-70 centimeters.

The two (initially and nominally identical) systems that have produced most of the material are manufactured by the Marshall Furnace Company, and use Model 1138 two-zone furnaces. Modifications were made to the motion controls to provide slower transport speeds, and portions of the furnaces were rewound. Pull rates of less than one millimeter per hour can now easily be achieved. The temperature controllers are of the Omega CN-2010 series with multiple independent set points and elaborate ramp and soak programming. Each zone has its own controller and can be maintained to within one degree centigrade of the desired temperature level.[39]

Two type R (Pt:Pt + 13% Rh) thermocouples are used to measure of temperature during growth. Initially, a third thermocouple is placed on a dummy ampoule and the furnace profiled. Figure 2-5 gives typical profiles for the two Marshall furnaces with two different sets of zone temperatures.

An important feature of these profiles is the reasonably sharp temperature gradient that exists near the center of the furnace. The location of this gradient is approximately the same for both sets of temperatures. As the furnace moves the gradient region travels across the growth ampoule and the HgATe material solidifies.

2.4 Growth Considerations

These considerations are far too numerous to be mentioned at length in this document. At least for HgCdTe, there are several good references and in particular a good review[40] on the issues surrounding the growth of materials which contain a great deal of mercury. In this investigation, a careful

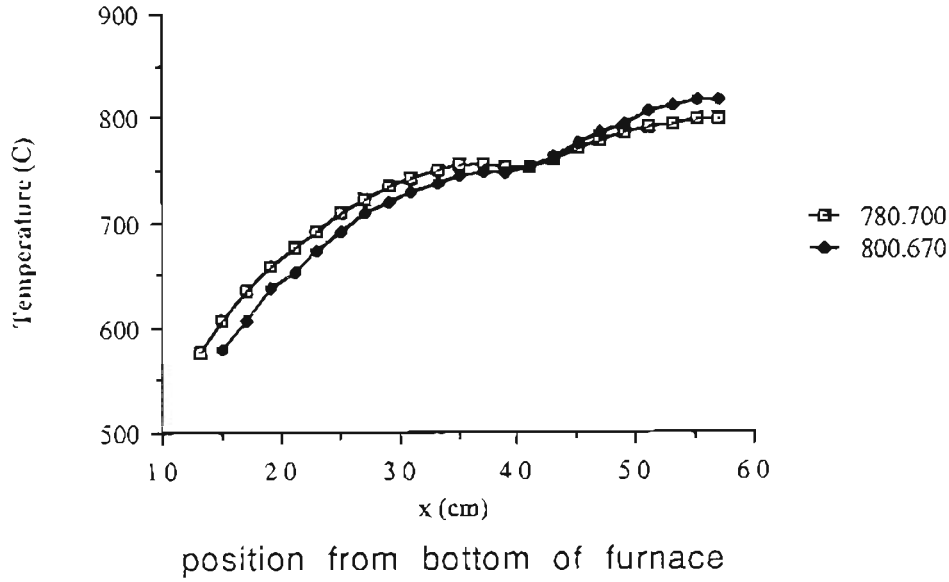

Figure 2-5 Profiles showing fairly sharp temperature gradient near the center of the furnace, (x≈40—45 cm) where solidification of the HgATe material occurs.

procedure was developed that would minimize intrusive, growth related problems and produce consistent material of the best possible quality. Still, several phenomena need to be considered on a sample by sample basis in order to understand results from subsequent characterizations.

Axial or longitudinal segregation has been documented in HgMnTe[11] and HgCdTe.[10] This investigation has measured longitudinal segregation in all of the novel alternative materials we have investigated. Radial segregation too adds complication and may be responsible for some variation in electrical conductivity from sample to sample and within samples. Segregation usually occurs and understanding its relation to growth conditions is necessary if it is to be controlled in a repeatable fashion.

Growth speed and segregation are closely related[12] and there appears to be a tradeoff between radial and longitudinal segregation in HgCdTe.[10] For the purposes of this investigation it was deemed important to have radially uniform material. This was accomplished by adjusting the pull rate to approximately one millimeter per hour during material growth. Data from the previously cited sources indicates that this growth rate will produce material with greater radial than longitudinal uniformity. Indeed the longitudinal segregation can be advantageous in that it produces samples of varying compositions within a single growth, that can be compared against each other.

CHAPTER 3
SAMPLE PREPARATION AND INITIAL CHARACTERIZATION

This chapter details preparation and characterization techniques that were designed to produce samples for subsequent parts of the investigation. A flowchart is provided in figure 3-1 that indicates the stages that materials passed through during these procedures. The individual steps are discussed in detail in the following sections.

3.1 Ingot Removal

Removing a boule from its quartz ampoule is straightforward, if somewhat messy. A high speed, water cooled cut-off saw with a v-block material holder is employed to score the quartz in a number of locations. All scores should be as deep as possible without actually cutting through the inner wall of the quartz ampoule. A series of three, equally spaced axial cuts from tip to tail are first made. Next, a cut is made above the top of the ingot and the top section of the ampoule is completely removed. A sharp edge (razor blade) can be placed on the top of one of the axial cuts and struck to induce the quartz to crack along the cut. With a bit of practice the quartz will easily crack along the three cuts and may then be lifted away from the ingot. More than likely the quartz will not come away cleanly and a series of ring-like cuts will need to be made around the ampoule. A flat edged tool can be placed into the groove of the cuts and gently twisted to fracture the quartz apart.

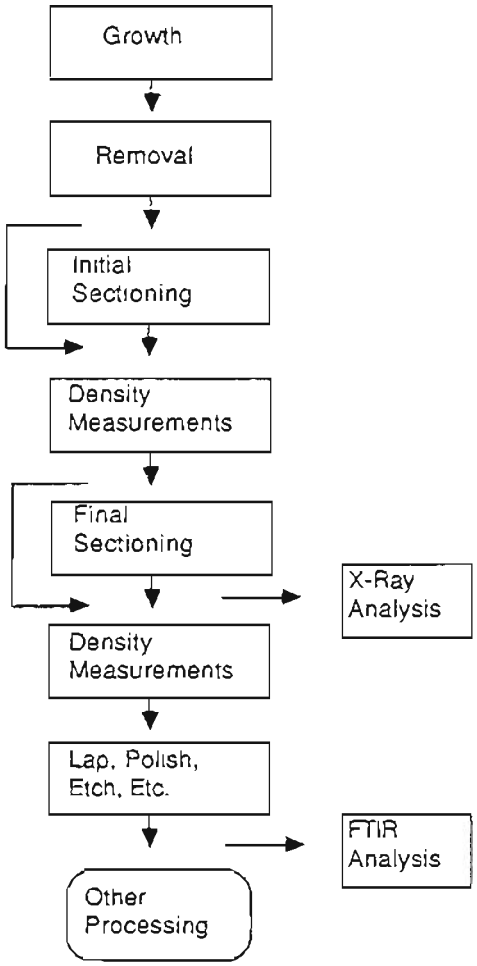

Figure 3-1 Procedures flow vertically downward. Some material may skip over the initial sectioning or final sectioning stages, or they may be extracted from flow to undergo x-ray or FTIR analysis.

More cuts in the quartz may be needed but eventually it should prove possible to remove all of it. In the process the ingot may be broken in several places. It is important to keep track of the order of the pieces, and their orientation. Sections of the ingot are carefully washed then stored until ready to proceed.

3.2 Initial Sectioning

The ingot, even if broken into several pieces, will doubtlessly need to be cut in several places. The intention of this initial sectioning is to generate sections about one centimeter long that can be subjected to density measurements. The actual size of the sections will vary somewhat since a broken piece of the ingot may, for example, logically yield two large sections or three small ones. Larger sections are typically more desirable than small ones.

A low speed diamond saw (South Bay #650) is employed for sectioning the ingot further. The ingot, or a portion of it, is attached to a graphite block using wax or modeling clay and placed on the arm of the saw. Once again it is important to keep track of the ingot's orientation so that the sections may be ordered. The cutting pressure is adjusted, an experienced hand is the best guide, and the saw is started. An initial speed of 100-120 RPM is desirable, but after the cut is established this can be increased to 200+ RPM. The time to finish a single cut varies with ingot diameter, the particular HgATe material, and the material's composition and the thickness of the saw blade. An average cutting time for a one centimeter ingot of $Hg_{0.89}Mn_{0.11}Te$ with a blade having a thickness of 0.01 inches is 30-35 minutes. The sections

are cleaned of wax and/or clay using acetone and methanol, placed in small boxes and labeled. Normally section A is the tip-most section and subsequent ones run in alphabetical order towards the tail of the ingot. This scheme is illustrated in figure 3-2.

3.3 Density Measurements

These measurements are made in order to determine the composition of the material. Since the densities of the binaries making up the (psuedo-binary) ternary are known and assuming Vegard's law it is possible to obtain an analytic expression for the density of the material $\rho(x)$. This relationship can then be inverted to yield $x(\rho)$, where the value of ρ is calculated after measuring the weight of each section in both air and liquid.

Assuming the zincblende structure, the relationship:

$$\rho(x) = \frac{80}{12.042}\left(\frac{(1-x)M_{Hg} + xM_A + M_{Te}}{(a_o(x))^3}\right) \qquad 3.1$$

gives the density of the psuedo-binary as a function of x. This relationship can be plotted, fit to a curve or expanded and approximated. Using the linear variation of a_o with x (Vegard's law) we have:

$$\rho(x) = \frac{80}{12.042}\left(\frac{(1-x)M_{Hg} + xM_A + M_{Te}}{(a_o^{HgTe}+(a_o^{ATe}-a_o^{HgTe})x)^3}\right) \qquad 3.2$$

With the information from table 1-1 to determine $a_o(x)$, a Taylor series expansion was done to obtain $\rho(x)$ to first order in x. This relationship was then inverted to give an approximation of $x(\rho)$. Density relationships for the

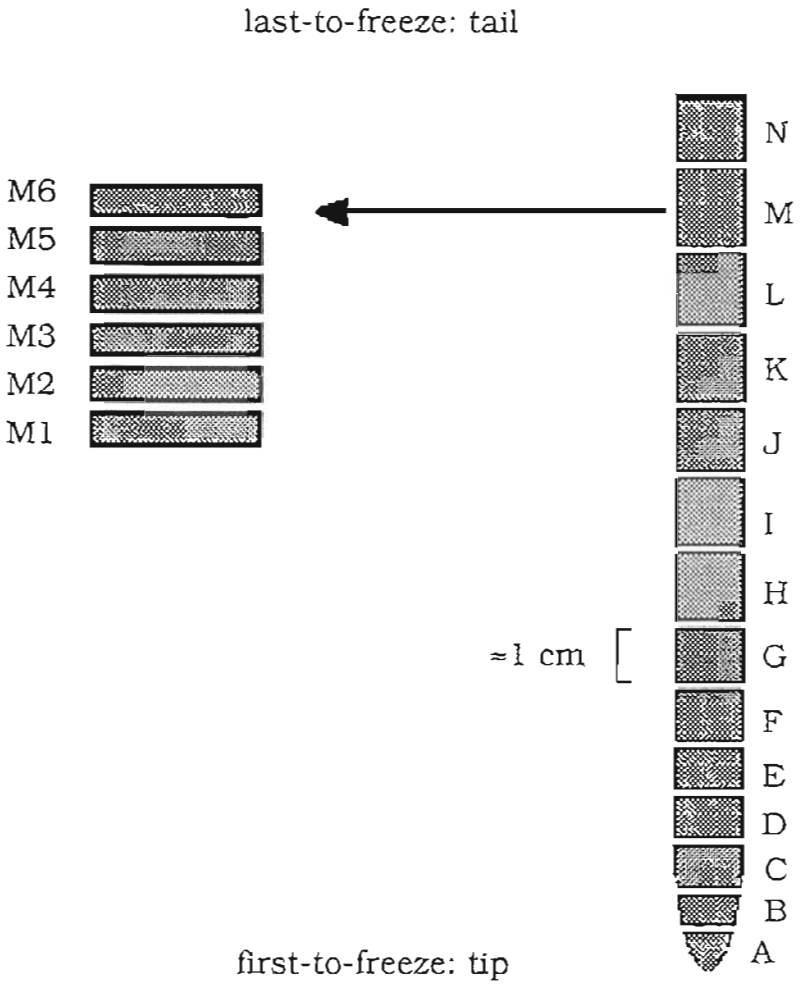

Figure 3-2 Ingots are divided into sections approximately one centimeter in length and labeled alphabetically beginning at the first-to-freeze end. Sections are further divided and a numerical suffix (beginning with the value one on the tip-most subsection) is added to the alphabetical designation.

four HgTe based materials known to form in the zincblende structure, are given in table 3-1.

Each sample section is weighed is air (W_a) and in liquid (W_l). The density of the section is then given by:

$$\rho = \frac{W_a}{W_a - W_l}\rho_l, \tag{3.3}$$

which ignores the buoyancy effect of air. The effect of this approximation is discussed in section 3.5. The density of the liquid can then determined by weighing a calibrated glass volume in air and then suspending it in liquid. The buoyant force provided by the liquid divided by the volume of the glass weight, yields the density of the liquid ρ_l. Note, that this calculation ignores the buoyant force provided by the atmosphere, which is considered to be negligible when compared to a liquid denser than water. Trichlorofluorethane is commonly used, and bas a density approximately 50% greater than water.

3.4 Final Sectioning and Density Measurements

Initial sectionings produce between eight and fifteen pieces of material. Density measurements are then used to calculate x values for each section. Since smaller pieces of the ingot will be cut and prepared it seems reasonable to make density measurements on each of them.

The sawing procedure is the same as before, though this time slices on the order of two millimeters in thickness are cut. Their ordering is main-

TABLE 3-1
Density as a Function of Composition
for Ternary Compounds

Material	Density (g/cm^3)	Ref.
$Hg_{1-x}Cd_xTe$	8.077 - 2.242x	22
$Hg_{1-x}Mn_xTe$	8.077 - 3.165x	23
$Hg_{1-x}Be_xTe$	8.077 - 1.244x	24
$Hg_{1-x}Mg_xTe$	8.077 - 5.490x	*

*This investigation, chapter three.

tained, numerically beginning in each subsection with the slice nearest the tip. The orientation of the individual slices is not maintained. On this scale of one or two millimeters in thickness, it is assumed that the material is axially uniform. The smaller thickness makes the cutting procedure more delicate and it is especially important to use a diamond wheel that is not warped. The same technique is used for the density measurements and x value calculation. Typical results for density measurements on HgATe material are given in figure 3-3.

3.5 Errors in Density Measurements

Calculations based on the aforementioned measurements suffer from the analytical error introduced by ignoring the density of air. This error would appear as the factor δ:

$$\rho = \frac{W_a + \delta}{W_a + \delta - W_l}\rho_l. \qquad 3.4$$

Assuming a sample volume of one cm^3 and a density of air of $1.2 \times 10^{-3} g/cm^3$, then $\delta = 1.2 \times 10^{-3} g$. A characteristic density of the materials measured is $8 \frac{g}{cm^3}$, which gives a relative error of less than one part in five thousand. A much more serious error is not analytical in nature but depends greatly on the size of the samples measured.

The roughness of the surface of the material is a source of error. A rough surface will trap air bubbles and cause erroneous measurements. Indeed, it is advisable to wait, after the sample has been immersed, for

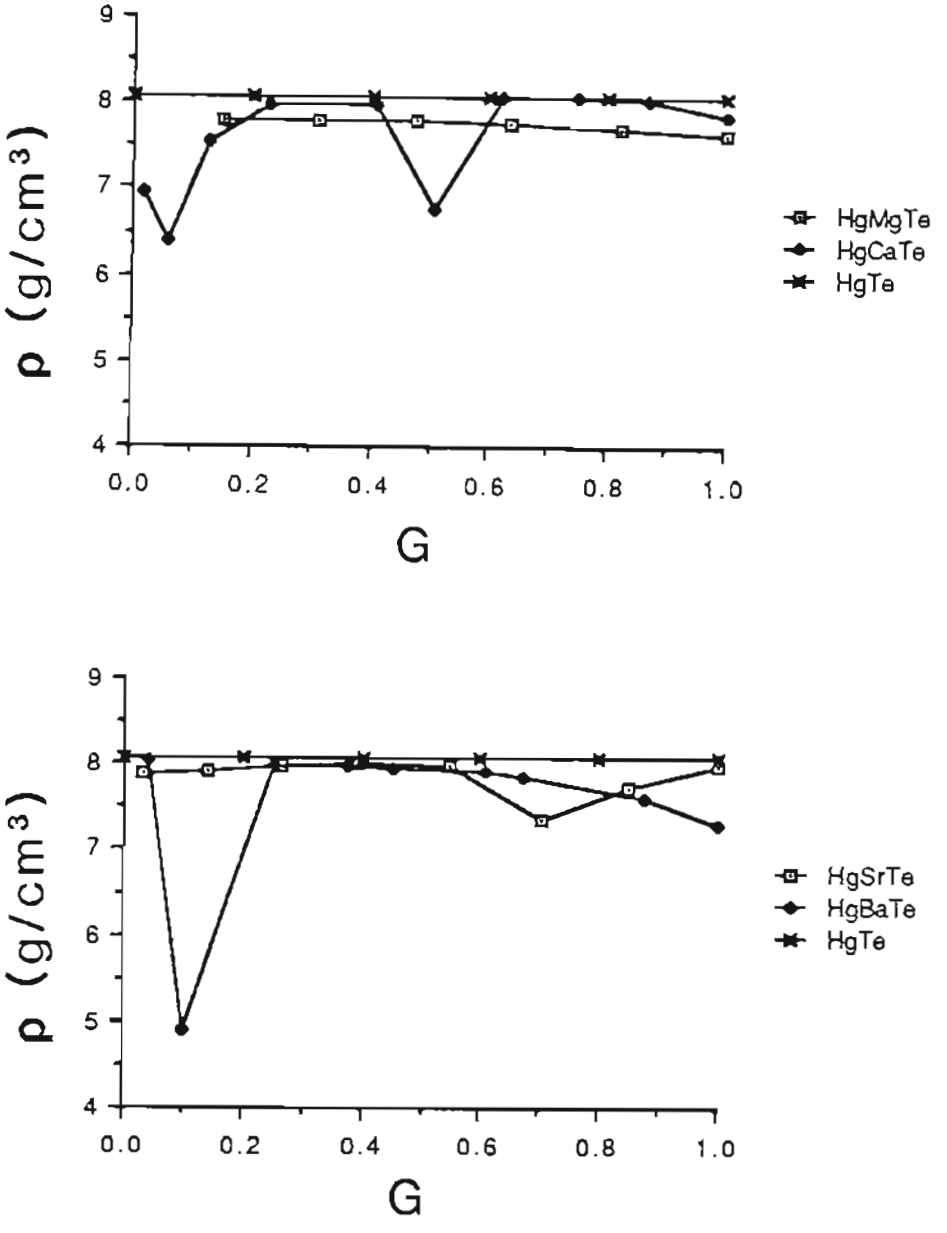

Figure 3-3 Densities are plotted with respect to G which is defined as the fraction of the total mass in the growth used to the point from which the section is obtained. Zero thus corresponds to the first-to-freeze end and one corresponds to the last-to-freeze end. The density of HgTe (x=0) is indicated on both plots. The HgMgTe growth was nominally x=0.11. Deviations from straight line behavior indicates segregation during growth.

upwards of one minute to allow any trapped air to escape. The surface area of sample does not decrease linearly towards zero with the weight of the sample, and will thus introduce greater error into small samples than in large ones. An empirical estimate of this error was made by comparing the measurement of a sample having unpolished faces with the same sample after polishing its faces. The radial surface was not prepared in any way.

The calculated density of a sample weighing approximately one gram changed by less than half a percent or one part in two hundred between these two measurements. A sample weighing approximately four grams changed by less than one quarter percent or one part in four hundred. Thus for material with an average surface quality, density measurements made in this matter suffer from a built-in error of $\pm 0.5\%$. The error that this introduces into the determination of x depends on the particular material being investigated. It is the difference in densities and lattice parameters of the two binaries that are the important factors. The closer the densities of the two materials, the greater the error introduced by an uncertainity in density. Other errors from voids or regions of differing crystal structure will also introduce errors. The presence of voids, of any great size, can normally be deduced from the large deviations they will produce.

As mentioned above, measurement errors are generally smaller for larger sample sizes. However, the density measured is an average value. So while larger samples will generally provide more accurate readings, they will not show the fine details of any compositional variations.

3.6 X-Ray and FTIR Analysis

If it had proved possible to obtain accurate measurements via Auger or SIMS of the materials' actual compositions one could then do lattice parameter measurements and correlate the two sets of data to obtain $a_o(x)$. Unfortunately, the only analytical technique available at OGC was an antiquated Energy Dispersive X-ray (EDX) system, which, without a standard to calibrate against is not accurate enough.

An alternate approach is to measure a material's bandgap using spectroscopic techniques and then to assume a linear variation between the bandgaps of the two binary materials to predict a composition, x. An experimental determination of density has already been made, and using this information along with the predicted value of x in the $\rho(x)$ formulation for zinc-blende material one can solve for a lattice parameter a_o. X-ray measurements of lattice parameter can then be compared to this predicted value.

A standard spectroscopic technique for chemists, Fourier transform infrared spectroscopy (FTIR) has begun to find numerous applications in the semiconductor industry.[41] Systems are available to be used in-line for process control, and can give a great deal of information about the optical properties of material.

The use of FTIR techniques with HgTe-based materials gives another, independent check on the composition. As discussed earlier the minimum energy gap is a function of the relative proportions of the binaries. By examining the transmission (or absorption) of a particular sample a characteris-

tic cut-on (or cut-off) wavelength, or energy can be determined.[42]

For a sample with energy gap E_g, light with $\frac{hc}{\lambda} < E_g$ is attenuated comparatively little as it passes through the material. When $\frac{hc}{\lambda} \geq E_g$ the transmission drops significantly as incident photons begin to induce electronic transitions between the valence and conduction bands. This information can be used to deduce the composition of the material under investigation, by inverting the $E_g(x)$ relationships given for the different materials to obtain $x(E_g)$. Further details of sample preparation and FTIR measurement techniques are available in appendix D.

After undergoing FTIR measurements samples were powdered and X-ray powder diffractometer measurements were made. The lattice parameters of a material can be measured very accurately with this technique,[43] and these values correlated to composition by means of Vegard's law. While the $a_o(x)$ relationship is fairly well known for both HgCdTe and HgMnTe, it is only predicted for other of the alternative materials used in this investigation. These measurements will be the first ones known to be done on several of these materials.

A Siemens D-500 system was used for the measurements. A standard software package was used to generate lattice constants from the intensity versus 2θ pairs measured. As is often the done, an internal powder standard scheme was used.[23] A small amount of commercially available semiconductor grade silicon was powdered and added to the sample powder. Software was

available to adjust the 2θ values based on where the silicon peaks should be versus where the particular machine claimed them to be. Additional details of sample preparation are available in appendix E. As a test of the accuracy of this machine and the efficacy of its software, a sample of CdTe was examined. The lattice parameter calculated by the Siemens system was within one percent of the value given by the standard reference works.[24] The X-ray powder spectrum of silicon that was admixed is given in figure 3-4.

If one assumes that Vegard's law is followed, the x-ray measurement of lattice parameter should provide an accurate measure of composition, x. However, as is the case with many III-V alloy systems, there is some non-linear bowing in the $a_o(x)$ relationship.[32]

3.6.1 HgMgTe Material

Recall that HgMgTe samples were subjected to FTIR analysis, which was then related to previous work detailing bandgap versus composition.[28] This work considered only four compositions of HgMgTe, two of these compositions being semimetallic. Two data points in the positive bandgap region of composition are not enough to generate an accurate "bowed" relationship for $E_g(x)$. The two positive data points were used to generate a linear $E_g(x)$ relationship for HgMgTe, which is used in all subsequent comparisons, and reproduced in table 1-2. Thus, for HgMgTe:

$$E_g(x) \approx -0.11 + 2.8x \text{ (eV)}. \qquad 3.5$$

Recall, that this is the room temperature relationship for HgMgTe. Samples

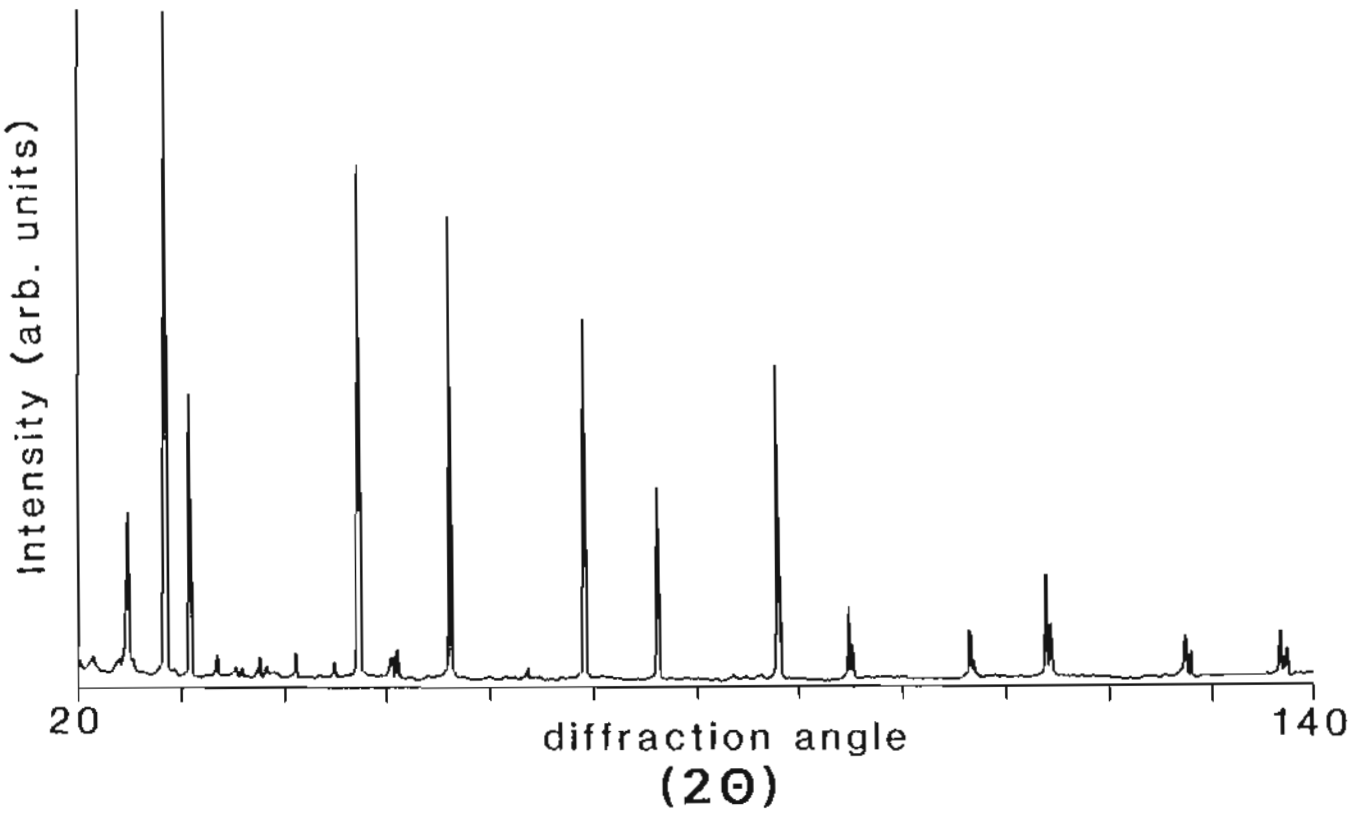

Figure 3-4 Silicon was added to all powdered samples of HgATe for use as an internal standard. Subsequent powder spectra thus show peaks not typical of the zincblende structure. When silicon peaks are not considered, HgCaTe, HgSrTe and HgBaTe spectra all show features similar to HgMnTe which is known to form zincblende material for $x<0.35$.

of HgMgTe were prepared as detailed in appendix D and subjected to FTIR measurements. The FTIR spectra from two of these samples are given in figures 3-5 and 3-6. A cut-on edge energy was determined for both samples.

To predict a composition from this value the $E_g(x)$ relationship is inverted to obtain:

$$x(E_g) = \frac{E_g+0.11}{2.8}. \qquad 3.6$$

With this relationship the compositions of samples OGC52E1 and OGC52F1 are determined to be 0.0786 and 0.0714 respectively. Solving the zincblende $\rho(x)$ relationship 3.2 for a_o one obtains:

$$a_o = \left[1170.7\ \frac{(1.9-x)}{\rho}\right]^{\frac{1}{3}}. \qquad 3.7$$

The densities of the two HgMgTe samples are known and these along with the calculated lattice parameter are summarized in table 3-2.

After FTIR measurements these two samples were powdered and data taken on the Siemens system. Their powder spectra are shown in figure 3-7 and 3-8. Using these two predicted values of 6.49 å and 6.48 å as input to the X-ray lattice parameter refinement routines values of 6.4900 å and 6.4797 å are obtained. Knowing the composition associated with these two values of lattice parameter and the lattice parameter of HgMgTe with x=0 (HgTe) a least squares fit is done on these three data points.

The resulting relationship is:

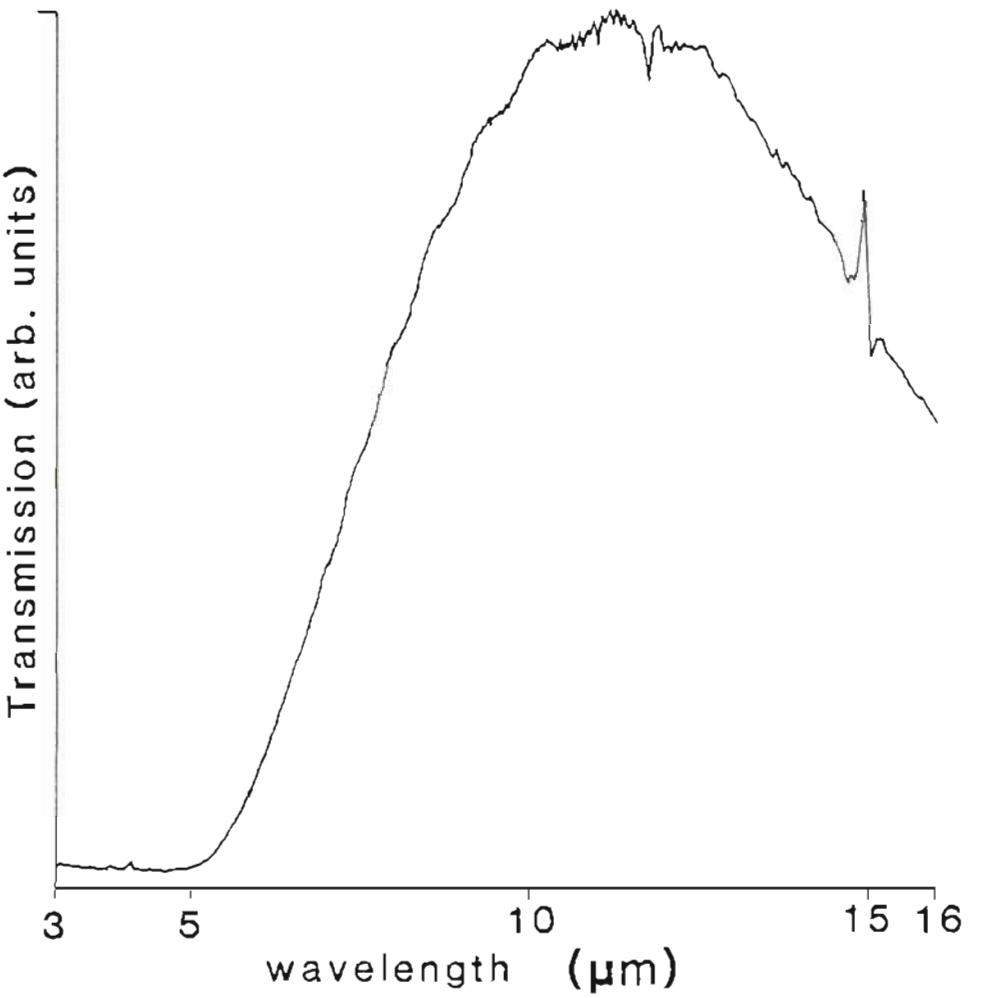

Figure 3-5 This (room temperature) transmission spectrum shows the cut-on edge obtained for OGC52E1. From this the minimum bandgap energy (at room temperature) of this particular sample is determined to be 0.11 eV (hc / 11.16μm).

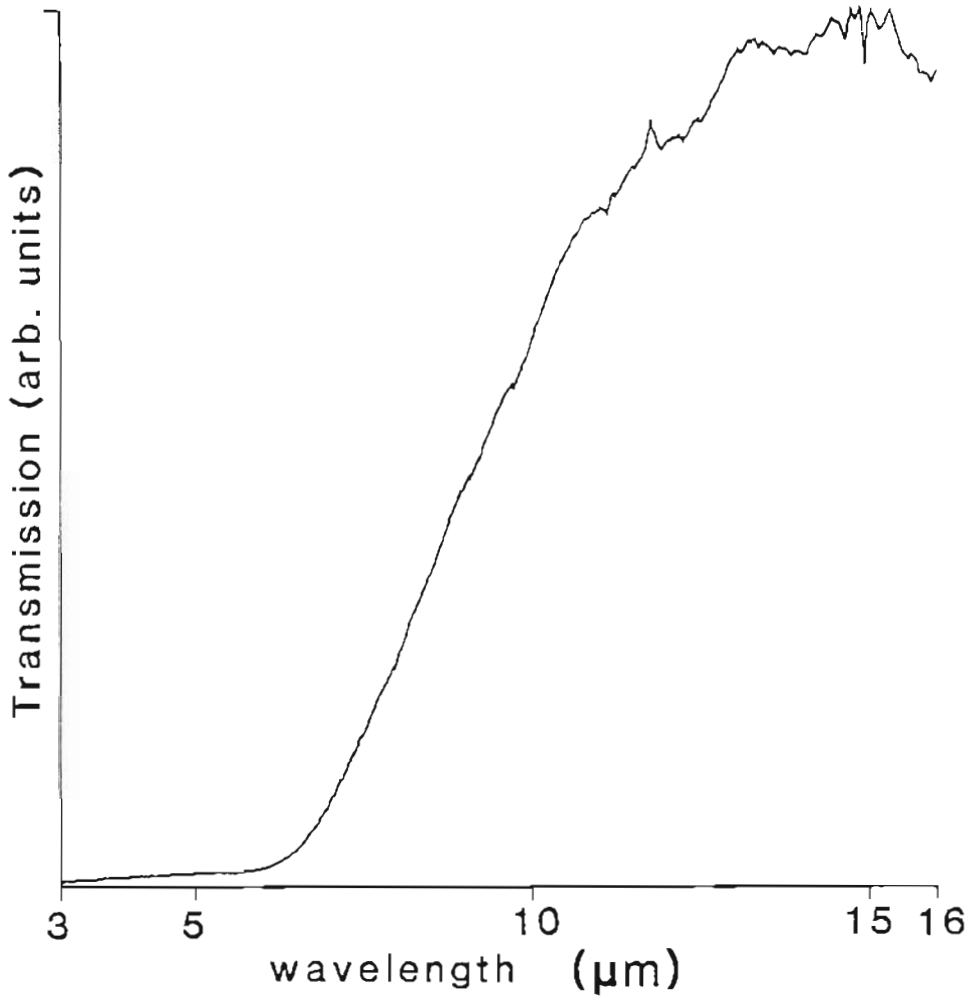

Figure 3-6 This (room temperature) transmission spectrum shows the cut-on edge obtained for OGC52F1. From this the minimum bandgap energy (at room temperature) of this particular sample is determined to be 0.09 eV (hc / 13.83μm).

TABLE 3-2
HgMgTe: Lattice Parameter Versus
Composition

Material	density (g/cm^3)	E_g (eV)	a_o calc.	a_o x-ray
OGC52E1	7.7019	0.09	6.480	6.4797
OGC52F1	7.6344	0.11	6.490	6.4900

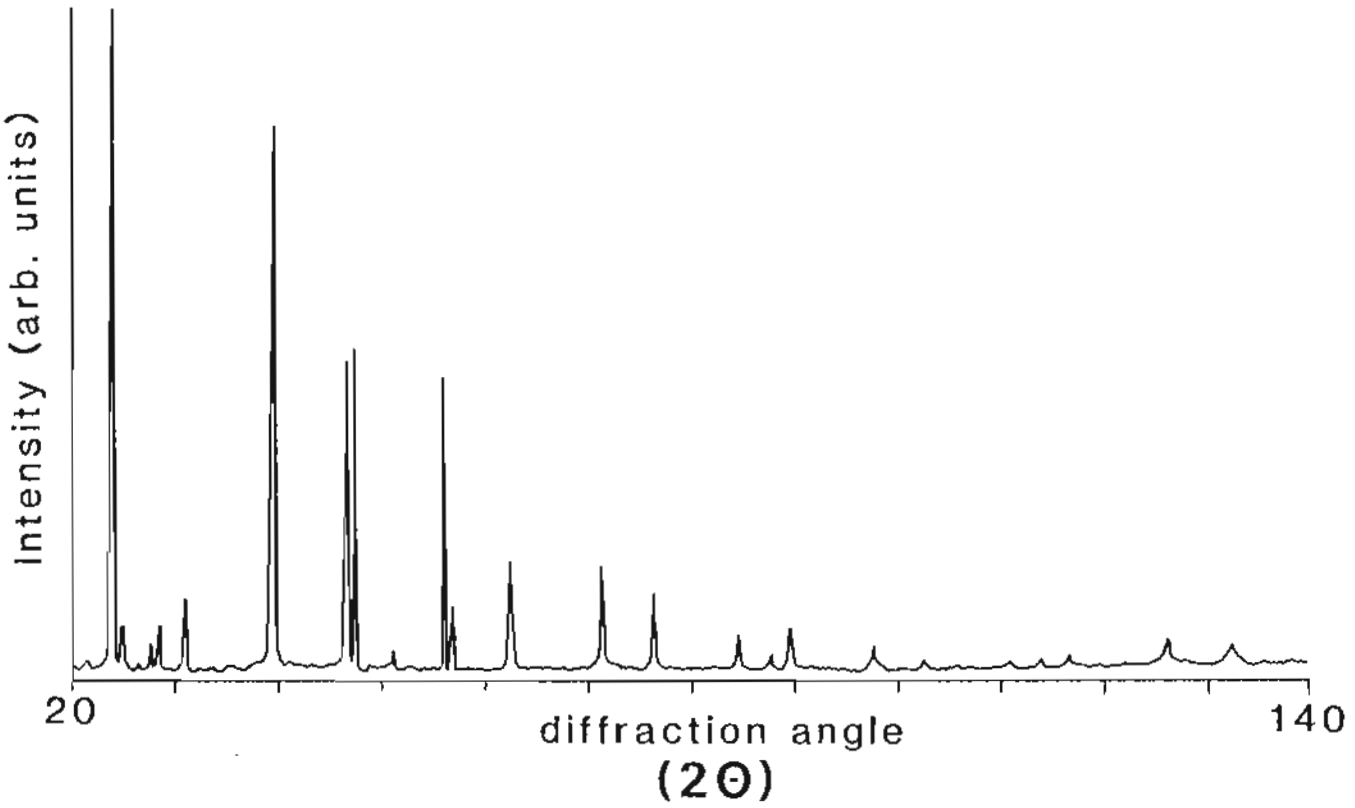

Figure 3-7 OGC52E1 (HgMgTe) was measured as having a lattice parameter of 6.4797 å. Based on FTIR bandgap measurements, and assuming a linear variation of bandgap with composition a prediction of 6.4806 å was made.

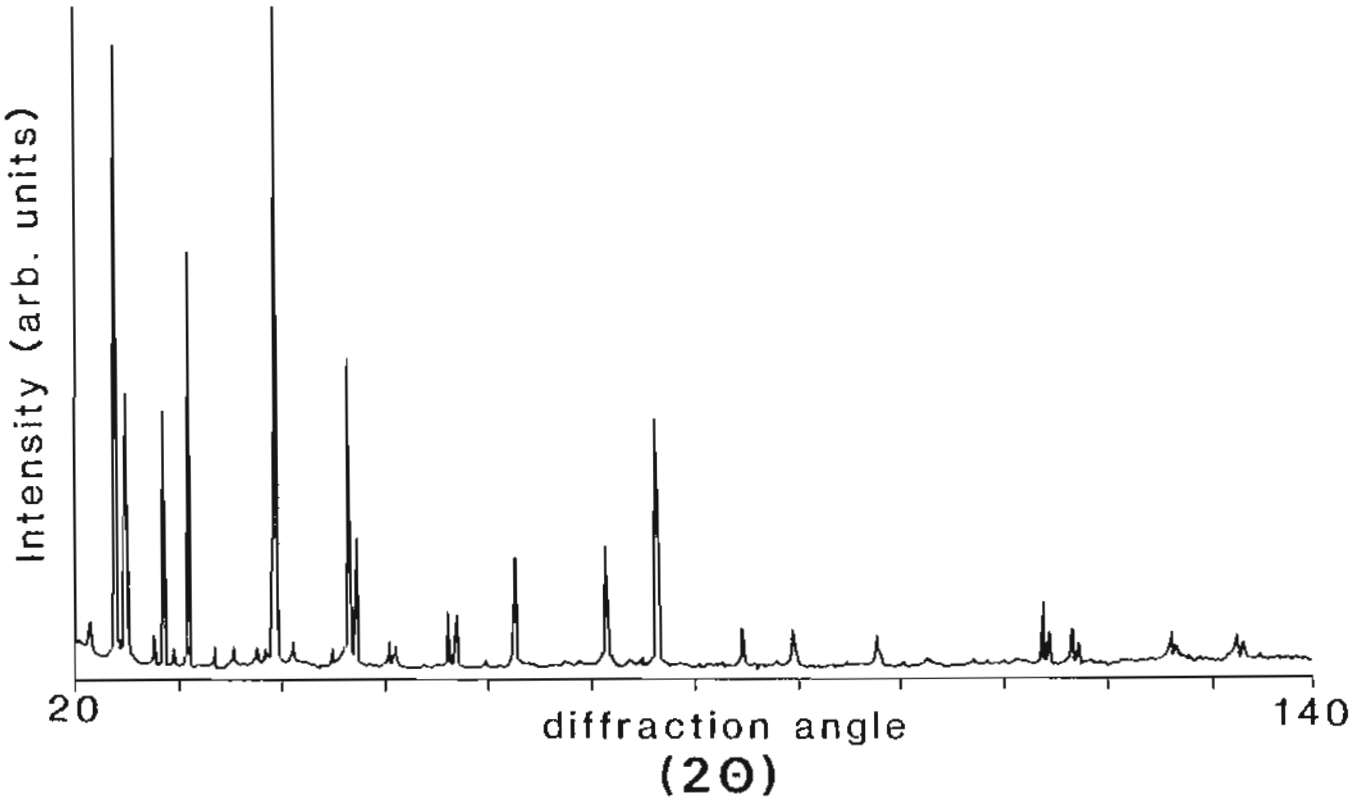

Figure 3-8 OGC52F1 (HgMgTe) was measured as having a lattice parameter of 6.4904 å. Based on FTIR bandgap measurements, and assuming a linear variation of bandgap with composition a prediction of 6.490 å was made.

$$a_o(x) = 6.462+0.307x. \qquad 3.8$$

3.6.2 Materials Containing Ca, Sr, Ba

Mercury-telluride ternaries formed with these three elements present some particular problems. As was mentioned in chapter one, with the exception of BeTe, the crystal structure of the remaining binary tellurides is that of NaCl. When forming a pseudobinary, i.e. $Hg_{1-x}Mn_xTe$, it can be assumed that the material retains the "host" zincblende structure for at least low values of x. As the "A" content increases, at some point mixed crystal phases may be present. Eventually, at very high x-values, the material will be forced to assume the NaCl structure. Note that in the region of mixed phases, x-ray measurements would show sets of peaks corresponding to both lattice types. Since our data shows only a single set (disregarding the admixed silicon reference peaks) we can safely assume that we are still forcing the nominally NaCl lattice to have the zincblende structure. However, we do not know the lattice parameter of this fictitious zincblende binary compound, so there is no reliable means for using the relationship 3.2 to determine a density versus composition relationship $\rho(x)$. Samples of these materials are best referred to, initially, in terms of their measured density rather than a value of x.

Unfortunately, no success was realized from efforts to produce HgCaTe, HgSrTe, and HgBaTe samples suitable for FTIR studies. Samples of these compounds were prepared for spectroscopy studies by the standard tech-

niques discussed in appendix E. These samples were then examined with FTIR over a wavelength range from 50 μm to 0.5 μm, and no distinct cut-on edge could be detected. The samples were thinned even further to approximately 40μm in thickness and measured again. The transmission of these samples was very close to zero. Only the thinnest of them showed any detectable transmission, and even then there was not a cut-on edge.

The Hall measurements made on these mercury annealed samples before they were thinned for FTIR work, indicated the material to be n-type. One explanation is that for the amount of Ca and Sr introduced into the Hg-Te lattice the bandgap of the material remains below that corresponding to $\lambda = 50\mu m$, or about 0.02 eV. Another explanation could be that a great deal of free carrier absorption is occurring. Further characterization work was done on samples of HgCaTe and HgSrTe, but in these cases the comparison of materials with similar bandgaps cannot be made. Powder spectra of HgCaTe and HgBaTe are given in figures 3-9 and 3-10.

A different problem arose with HgBaTe. Density measurements (see figure 3-3) indicated that some barium was introduced into the ingot, and visual inspection showed portions of the growth to be fairly uniform, and without voids. However, the preparation procedure, which is documented thoroughly in appendix E could not be completed. Samples were cut successfully but as they were being mounted to the lapping jig with phenyl salicylate, drops of mercury formed on the sample's exposed surface.. The jig and sample were at a temperature of approximately 50C, which is just sufficient to melt the phenyl salicylate. This phenomena of material weeping

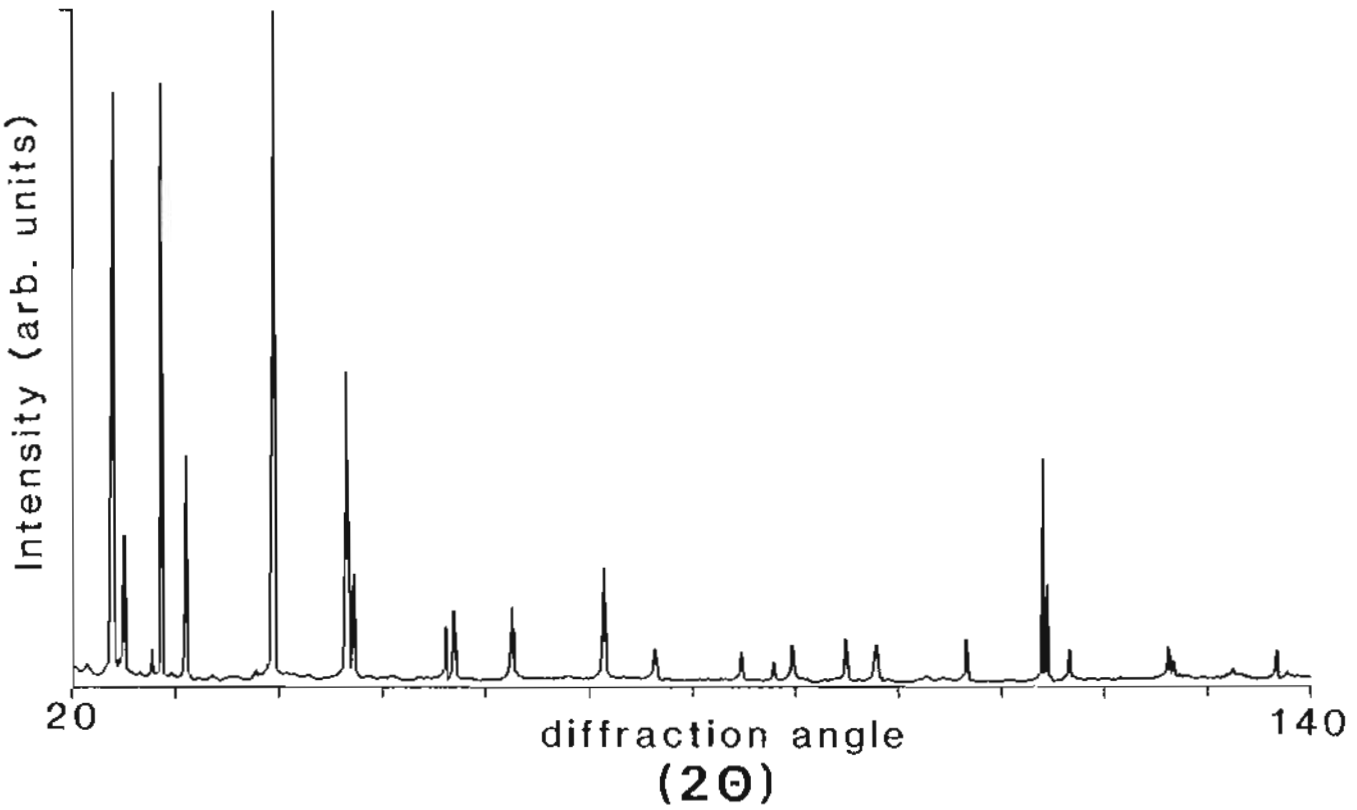

Figure 3-9 OGC53C6 (HgCaTe) had a measured density of 7.966 g/cm^3. The lattice parameter refinement routine used with the Siemens system did not converge strongly to a final value. The best estimate this algorithm could give was a value of 6.4582 Å. This value is less than that for HgTe.

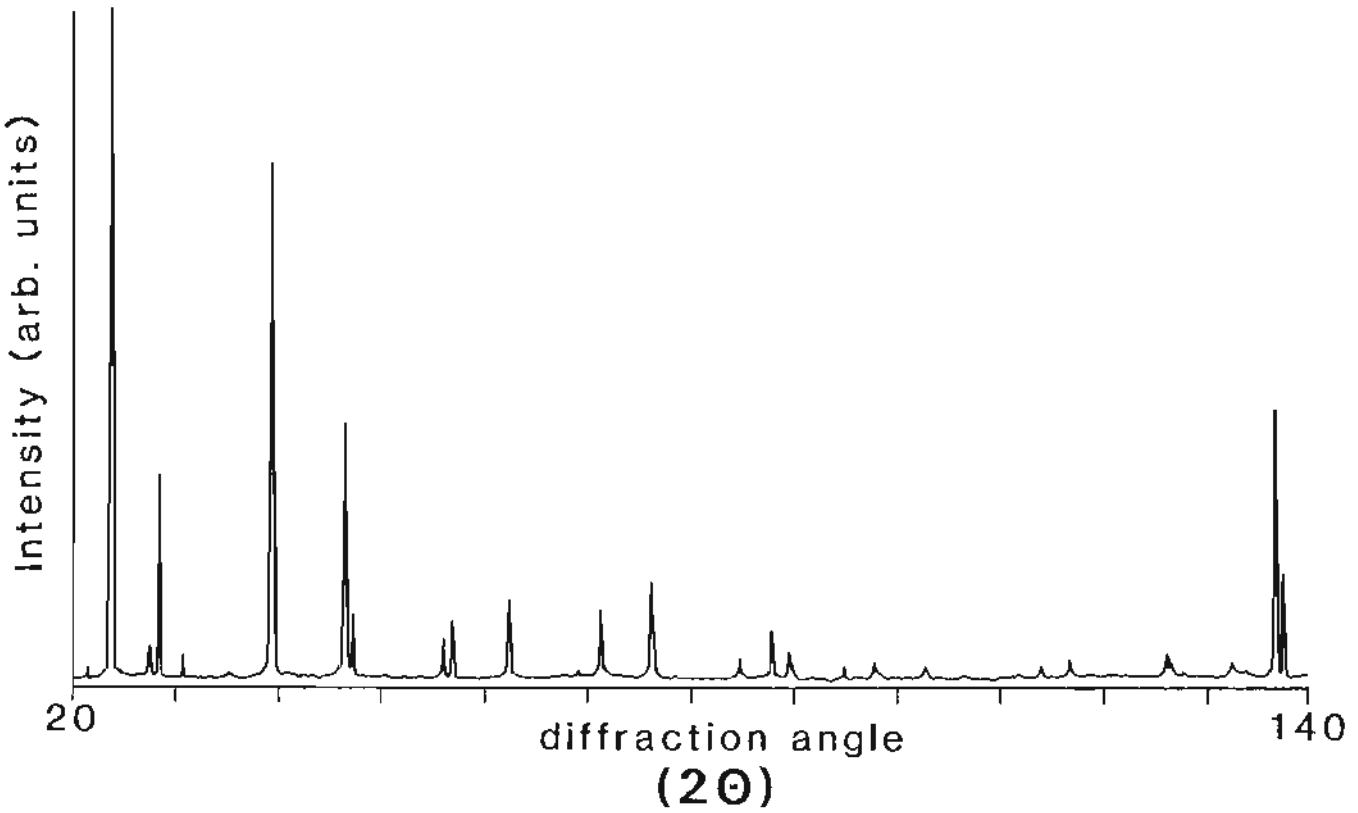

Figure 3-10 OGC54C6 (HgSrTe) had a measured density was 7.921 g/cm^3. its lattice parameter, again with weak convergence of the refinement routine, was 6.4723 Å.

mercury has been observed before but only in material riddled with small voids. Once mounted to the jig one side of the samples were lapped and a good quality optical surface obtained. When the samples were warmed to be dismounted so that the opposite side could be lapped and polished, more mercury was seen to escape the surface.

That this occurs at temperatures of only 50C does not bode well for the potential applications of HgBaTe. One supposition is that the material does indeed begin to decompose at very low temperatures. This seems likely since no free mercury was observed during cutting and no voids were detected.

An X-ray powder spectrum for a typical sample of HgBaTe is given in figure 3-11. Hall data for HgBeTe samples was obtained on unfinished, rough surfaced samples and is presented in chapter four.

3.7 Material Containing Beryllium

The growth of HgBeTe was approached with some trepidation since beryllium[44] is exceedingly toxic. Theoretical work on the properties of BeTe[26] and the fact that the binary, like HgTe, is zincblende,[24] seemed promising and a growth was started. The growth finished without incident but before opening the ampoule literature on the toxicity of beryllium was reviewed in greater detail.

After this perusal, it was decided that safe facilities for the handling, cutting and polishing of beryllium compounds were not available. In particular the cutting, lapping and polishing equipment is not vented well enough.

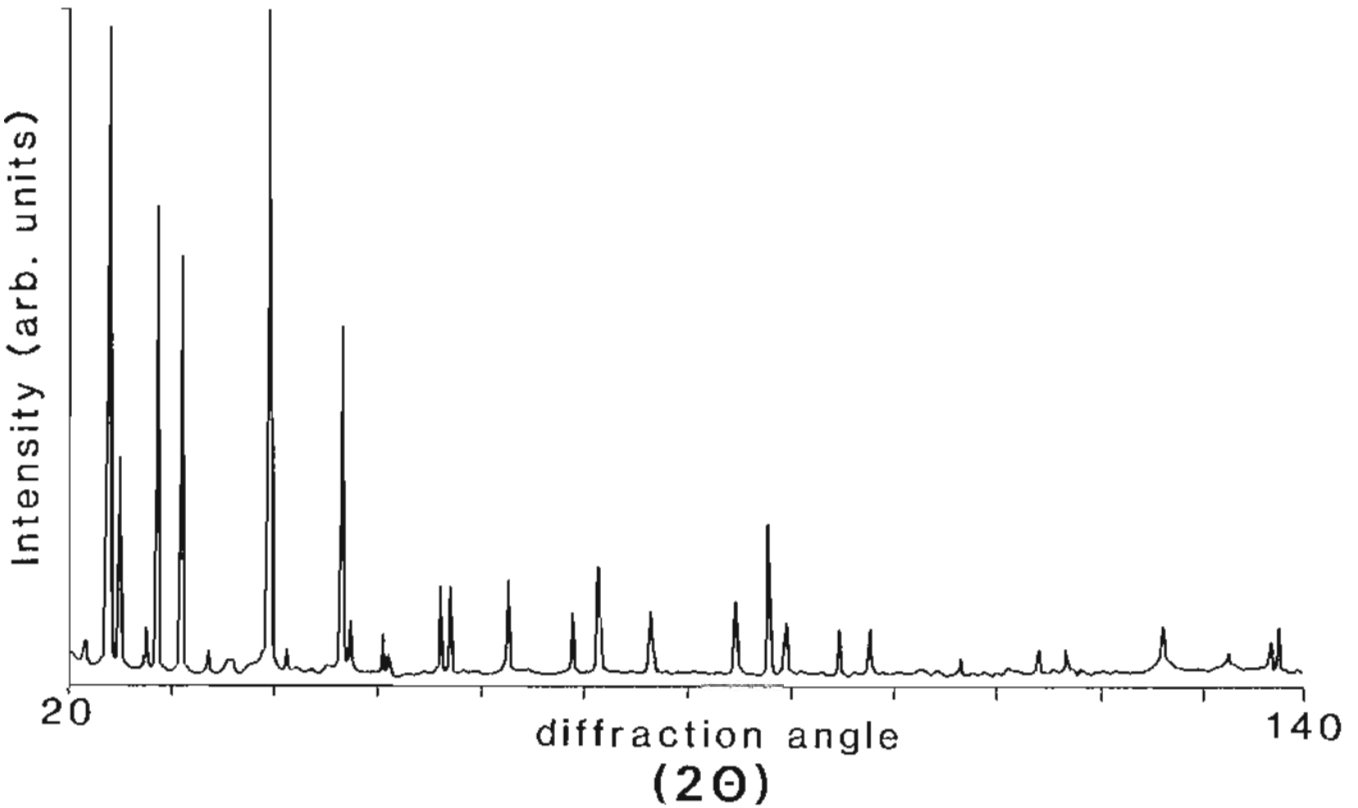

Figure 3-11 OGC55E2 (HgBaTe) had a measured density was 7.947 g/cm^3. Its lattice parameter, once again with weak convergence of the refinement routine, was 6.4912 a.

The single ingot of (nominally) $Hg_{0.90}Be_{0.10}Te$, thus remains in its growth ampoule and has been subjected to no characterization.

Initial visual examination of the material through the quartz ampoule seem to suggest that the growth was successful. The ingot has regions of uniformity near the tip of the growth which is an important region if good first-to-freeze end material is to be obtained. It is hoped that facilities can be found to safely prepare and examine this growth. However, no further experimental data for HgBeTe will be available for discussion in this work. After approximately two months in a sealed air environment this growth (only partially removed from its growth ampoule) has partially decomposed into powdered material. This decomposition is not uniform along the length of the ingot however. Only the tail-most section of the growth has decomposed. This would seem to suggest that the compositional characteristics vary greatly along the length of the ingot, possibly from segregation during the growth.

HgBeTe then, was the least explored of the novel HgTe-based materials, followed by HgBaTe. None of the material from these growths successfully underwent the procedures shown in figure 3-1. Single growths of both HgSrTe and HgCaTe received substantial scrutiny, but as yet no $\rho(x)$ relationship is available for either of these materials. Multiple growths of HgMnTe and HgMgTe were studied extensively and a psuedo-zincblende lattice parameter for HgMgTe was obtained. Multiple growths of HgCdTe were available and samples were studied in parallel with the aforementioned materials and comparisons are made in subsequent chapters.

CHAPTER 4
RESULTS OF PROCESSING AND CHARACTERIZATION

4.1 Introduction

Certain characterization techniques are inherently destructive in nature. Further, any particular characterization techniques may be incompatible with techniques which proceed or follow it. Good examples of these concerns are FTIR and Hall analyses, and x-ray powder diffraction. The latter of these is, clearly, rather destructive. The former two are incompatible since very thin specimens are needed for FTIR work but this very thinness makes handling and preparation for Hall analysis difficult.

A realistic course of action then, is to begin with multiple samples that have been grown and prepared in an identical fashion. At the end of the preparation outlined in chapter three (figure 3-1), it is possible to select samples that should yield identical results. Individual samples can then be removed and characterized at some point during the processing. The results obtained can then be expected to be comparable to those that would be obtained from the other samples, if it were possible to characterize them without interrupting their processing. From the flowchart in figure 4-1, procedure A was undertaken with the intention of providing information about the relative amount of mercury lost from a sample of a HgTe based material during exposure to CO_2 laser radiation.

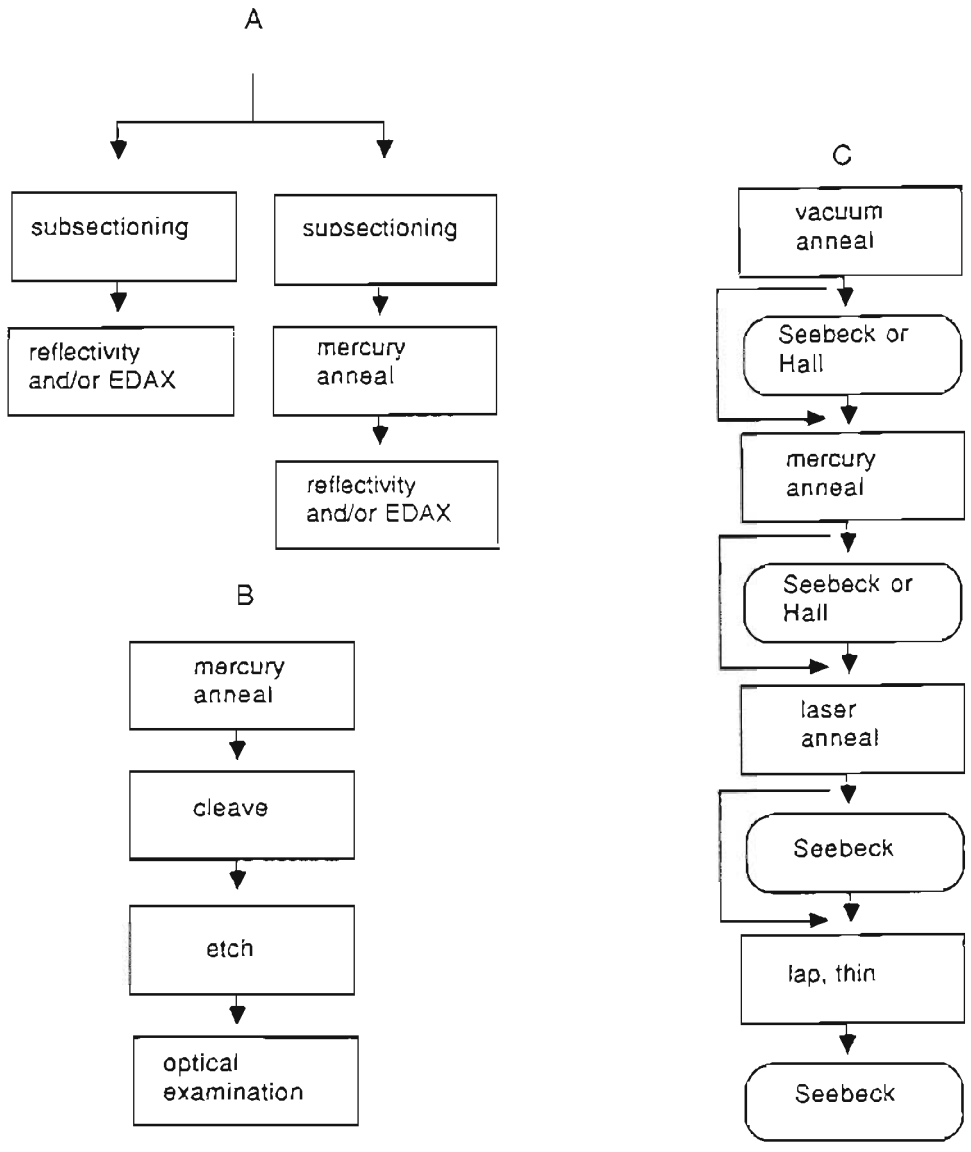

Figure 4-1 Samples prepared as detailed in chapter three may follow one of two paths in procedure A. These two paths generate data on stability of the Hg-Te bond in HgATe materials of different compositions. Procedure B was designed to measure diffusion rates of mercury into HgATe by revealing a line of defects along the cleaved edge of the sample. Procedure C tracks changes in the electrical properties of samples.

4.2 Mercury Loss by XES and Reflectivity Techniques

X-ray Energy Spectroscopy (XES) techniques have been established to yield valuable information about the relative amounts of component materials within an alloy.[45,46]

HgTe materials provide a special challenge to this technique, once again due to the high vapor pressure of mercury. XES instrumentation is often found as ancillary equipment on a scanning electron microscope (SEM), and such is the case at OGC. An EG&G Ortec instrument is available on a JEOL JSM-35 scanning electron microscope. The particular version of XES analysis implemented by this system is known as Energy Dispersive X-ray analysis or more conveniently as EDX.

4.2.1 Initial XES and Reflectivity Work

Materials with:

$$E_g \approx \frac{hc}{\lambda_{CO_2}}, \tag{4.1}$$

where $\lambda_{CO_2} = 10.6\mu m$, were selected and sectioned into subsamples (See appendix E) the final dimensions being approximately two millimeters square and one millimeter thick. The two millimeter dimensions were chosen so as to provide a subsample that would fit entirely within the laser spot. The subsamples were next mounted to a flat rectangle of quartz to facilitate handling, and identification (see appendix E for details). Lastly it was assumed that material properties would not vary over the individual sample from

which a set of subsamples was obtained. This was needed in order to make comparisons between the subsamples meaningful. The validity of this particular assumption is discussed later in this chapter.

Prepared subsamples were next exposed to a Sylvania CO_2 laser model 948. Exposures of various times at an identical cw power (5 watts $\pm$ 0.1 watt) were made with the intention of correlating the irradiation time with the amount of mercury lost. Optical examination of the exposed subsamples prior to XES work revealed a tendency for there to be a significant degradation in surface quality after a particular exposure time. A good example of this is given by a one centimeter sample that was not divided into subsections before being irradiated.

Figure 4-2 gives a diagram of this sample of HgMnTe, which was not cooled while being exposed to a CO_2 laser at five watts of power for twenty seconds. EDX data was taken before and after the exposure and the percent change in the amount of mercury at various points across the sample is indicated. The inner circle represents a region where the surface of the sample was damaged by the laser exposure. Note that comparatively little mercury was lost outside this region, which corresponds well with the size of the beam spot and that there is a significant difference in mercury loss as measured just inside versus just outside this region.

Other investigations have reported surface damage to II-VI materials after irradiation by laser both cw and pulsed.[47-49] At this point it was postulated that the damage to the surface could be related to the onset of a

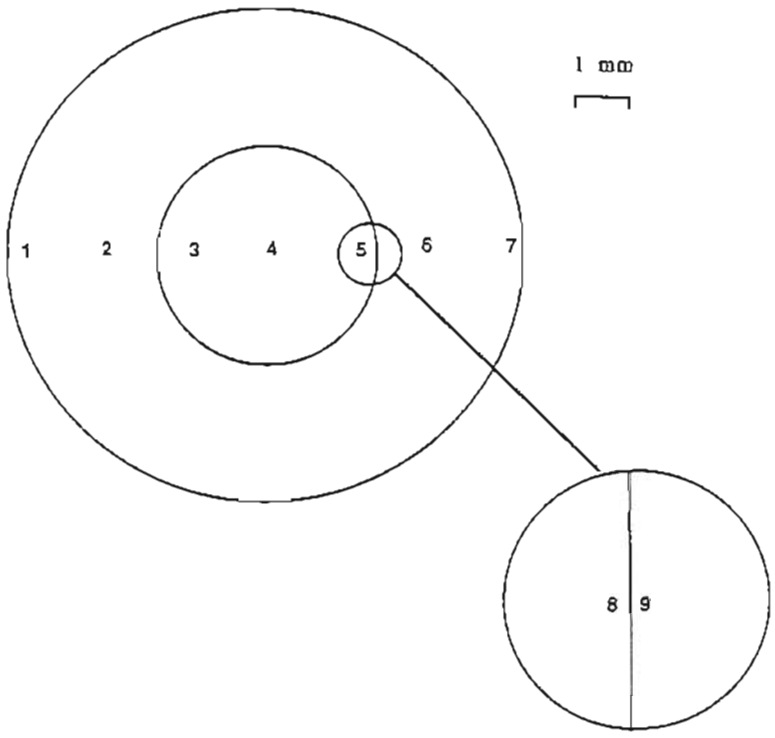

data	1	2	3	4	5	6	7	8	9
before	18.9	20.3	20.4	20.5	20.1	19.4	19.4	≈20.1	≈20.1
after	16.9	14.1	4.7	5.1	5.5	17.4	16.4	5.9	9.1
Hg loss %	11	31	77	75	73	10	15	71	55

Figure 4-2 A sample of HgMnTe with x≈0.1 is represented, with an inner circle showing the physical size of the laser spot. EDX measurements taken at the points indicated, before and after irradiation are used to generate a percent mercury loss value. These values are indicated above.

significant mercury loss from the surface and near-surface regions of the subsample. If this is the case one would expect to see EDX data indicating little mercury loss during exposure times up to and including the length of time for which the last "undamaged" sample was exposed. To say that a subsample has experienced damage is a somewhat subjective measurement. A better measure is obtained using a version of a reflectivity technique that has been used in laser recrystalization work[50] to detect the onset of material melting. A milliwatt HeNe laser was arranged so that it could be directed at subsamples with an incident angle of approximately 45 degrees. The reflected beam was measured with a digital photometer (Tektronix #J16).

Subsamples which had previously been examined with EDX were subsequently examined using the aforementioned reflectivity technique. The resulting values of mercury content were ratioed against the control subsample from each sample that was not exposed to the laser. These measures, Γ_{EDX}, are a function the mercury content X_{Hg} given by EDX measurement which in turn is a function of the exposure time τ. The exposure time has discrete values given by the subscript i and the relationship is:

$$\Gamma_{EDX}(\tau) = \frac{X_{Hg}(\tau = \tau_i)}{X_{Hg}(\tau = 0)} \qquad 4.2$$

The reflectivity data obtained was ratioed in the same manner as the above mentioned EDX measurements to obtain a reflectivity measure Γ_{ref} which again is a function of the individual subsamples' reflectivities R which are a function of the exposure time:

$$\Gamma_{ref}(\tau) = \frac{R(\tau = \tau_{ij})}{R(\tau = 0)} \qquad 4.3$$

The EDX and reflectivity data are plotted on the same graph in figure 4-3.

Obviously there is a very good correlation between the onset of surface damage and the onset of mercury loss. With this connection documented it seemed worthwhile to devise an experiment that would take advantage of the relative simplicity of the reflectivity technique. This choice was met with a degree of relief within the community that uses the SEM, as mercury contamination was of some concern to them. While mercury loss at room temperature under a vacuum has been shown to be negligible for HgCdTe,[51] electron beam induced mercury loss is a real concern.[52]

A block diagram of the reflectivity experiment in its final form is given in appendix G figure G-1. The advantage of this techniques is that the surface quality of the subsample under investigation is measured continuously as a function of exposure time. Further, a single subsample can provide the full amount of information that formerly required a number of subsamples (one for each data point). This effectively multiplies the amount of data available by the number of subsamples cut from a single sample, normally eight to twelve.

4.2.2 Comparison of Materials Before and After Thermal Anneal

Many investigations have shown that bulk growth of HgCdTe often results in p-type material due to the concentration of native defects, primarily[18] mercury vacancies which act as acceptors. The resulting material

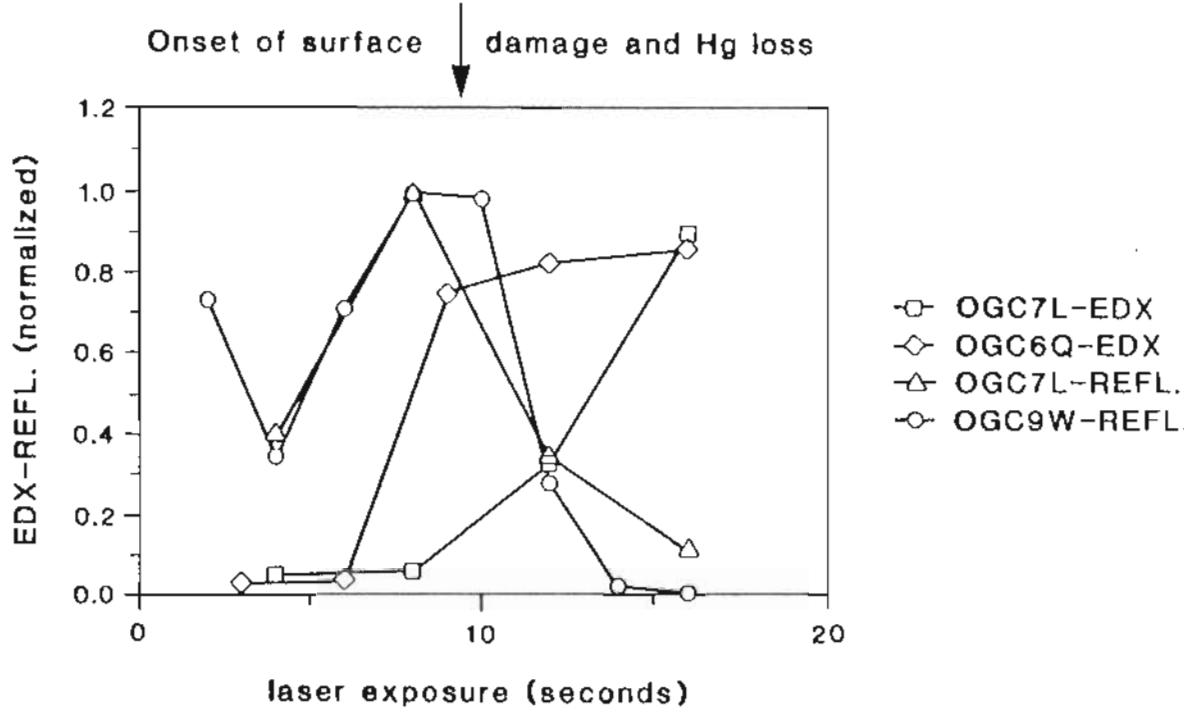

Figure 4-3 Samples exposed to laser irradiation for various lengths of time were characterized by reflectivity and EDX techniques. Plotted in the same figure the two types of data show a similar onset (near 10 seconds) of significant change.

must then be annealed in mercury vapor to reduce the vacancy concentration to an acceptable level or to invert the carrier type by introducing mercury interstitials.[53] An alternative procedure, proposed recently[54] involves a mercury anneal by immersion in a bath of mercury. The former annealing procedure is discussed in appendix H, and is the process used in this investigation. As is often the case with p-type material intra-valence band transitions can conspire to greatly increase the absorption of photons whose wavelength is below the material's intrinsic absorption edge.[55]

Part of the motivation for laser annealing studies of HgATe is the hope that photons with $h\nu = E_g$ will be absorbed after penetrating a finite distance into the material, thereby annealing ion implant damage, located some distance below the material's surface. Intra-valence band transitions pin the extinction length of photons, even those with near bandgap energy, to near zero. Thus, the possible advantage of laser annealing is lost for as-grown material since the rapid heating that occurs when the radiation is absorbed at the surface causes material damage before any improvements in electrical properties are realized. Conversion of material to n-type should result in more of the incident radiation passing through the surface region and giving a more uniform heating.

The information obtained from reflectivity data is the maximum exposure time possible for given beam parameters, before surface damage and mercury loss begin to occur. Typical reflectivity output for several materials is given in figure 4-4.

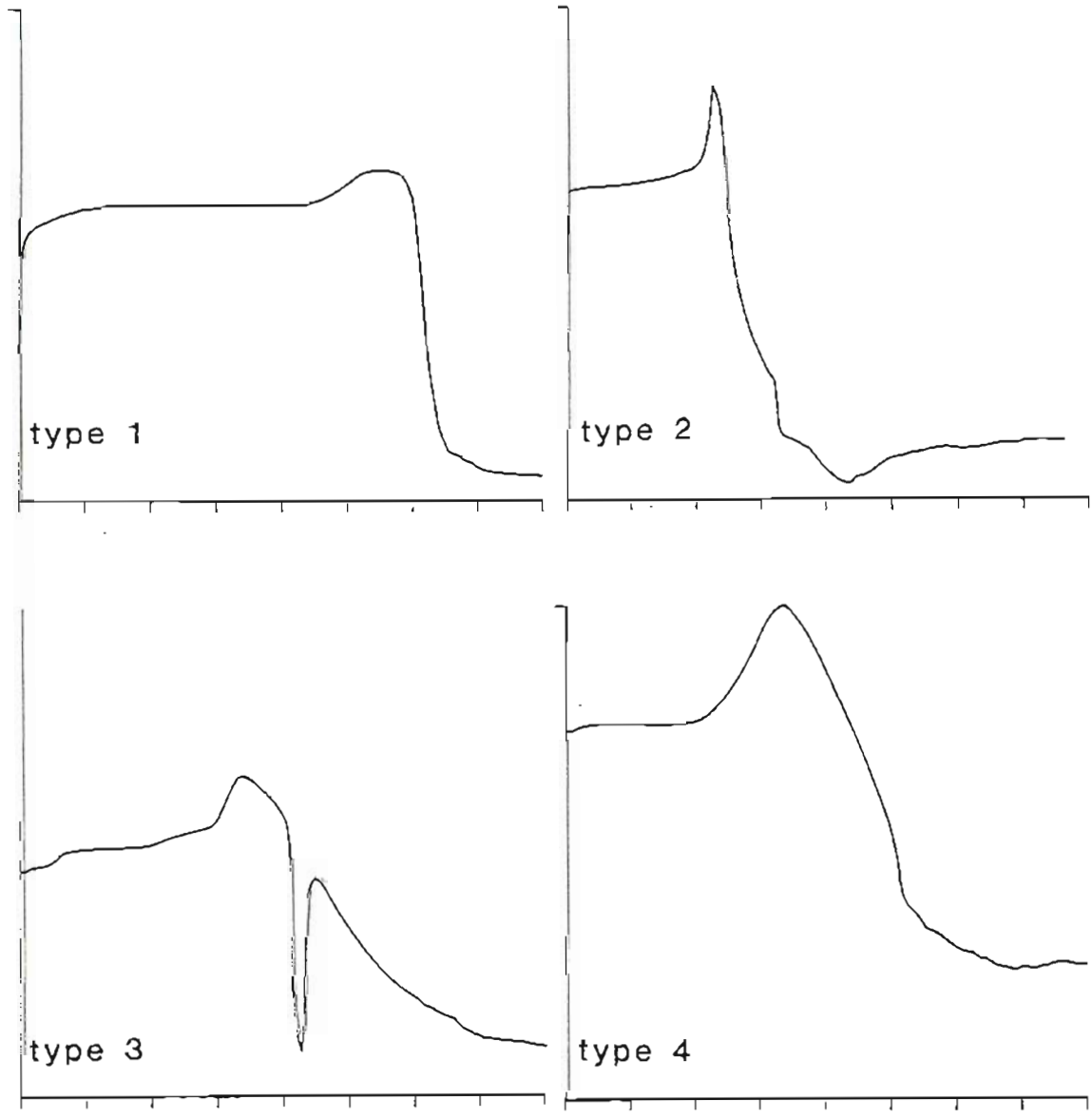

Figure 4-4 Each sort of trace (type 1-4), is found to occur in each of the HgATe materials. All traces show a distinct rise in reflectivity followed by a sudden precipitous fall. All verticle axes are of reflected intensity (arbitrary units). The time at which the maximum reflectivity is measure is designated t_d.

The similarities in the four typical traces are obvious. All of these traces are from runs at a nominal five watts of power. Type one shows the classical behavior of a rather lengthy exposure time followed by a relatively quick rise in reflectivity and then immediately followed by a precipitous decrease. After the catastrophic drop the reflectivity maintains approximately ten percent of its initial value over a period of tens of seconds.

Type two shows the same basic behavior but with a much larger and quicker rise in reflectivity. The precipitous drop occurs quickly and after achieving a minimum the reflectivity rises slowly to approximately twenty percent of its original value which it maintains for the duration of the exposure.

Type three shows a more gradual increase in reflectivity and a more gradual decrease to approximately thirty percent of its initial value. Note that there appears to be some symmetry in the traces about the region where the reflectivity increases just before declining.

Type four displays the oddest behavior and is typical of approximately twenty-five percent of the total number of samples measured with this technique. This type of behavior occurs in samples of all materials and in various compositions. There appears to be no correlation to a particular material or preparation. After the initial drop the reflectivity immediately rebounds to approximately eighty percent of its initial value then begins a slow decline to a final level at twenty percent of its original value.

The sudden increase in reflected intensity I_R occurs in all types of

materials investigated. Other investigators have used a similar reflectivity technique to observe the laser recrystalization process in silicon.[56] They too observe a sudden increase in reflectivity and attribute it to the surface of the silicon melting. Interestingly enough when the silicon surface is allowed to resolidify the reflectivity returns to its initial value. In HgTe based materials the surface melting is always immediately followed by a precipitous and permanent drop in I_R. Further, a significant amount of mercury is released as the sample is irradiated for times longer than the characteristic time t_d at which I_R initially begins to increase. This was confirmed by previously discussed EDX results.

For silicon, even if some material is lost from the surface the semiconductor remains stoichiometric. In HgTe-based materials a large amount of only one component (mercury) is removed. Thus the sudden and permanent drop in the reflectivity is not surprising.

The laser irradiation of HgTe materials carries with it an additional health hazard. During initial work the sample stage was partially enclosed in a lucite box and a commercial gold-film mercury vapor detector (Jerome Instruments #411) with a sensitivity of 1 $\frac{\mu g}{m^3}$ was employed. Mercury vapor in concentrations in excess of 100 $\frac{\mu g}{m^3}$ was detected. The currently accepted TLV for a daily, eight-hour exposure to mercury vapor is 50 $\frac{\mu g}{m^3}$ (consequently subsequent work was done with a vented sample stage).

As discussed earlier, as-grown material is usually strongly p-type. Thus free carrier absorption and/or intra-valence band transitions make the material strongly absorbent for most radiation. Annealing in mercury vapor converts the material to n-type and typically reduces the carrier concentration several orders of magnitude. Annealed material, then, absorbs CO_2 laser radiation (if it is sub-bandgap) much less strongly than unannealed material. Since the amount of incident laser power absorbed in the surface region is less in annealed material than for as-grown material the characteristic time t_d for annealed material should be longer than that for as-grown material. Because of this there is a logical distinction between data for as-grown and annealed materials and they will be presented and discussed separately.

Table 4-1 gives a summary of the characteristic exposure times t_d for the samples examined using this technique. The same information is shown graphically in figure 4-5. The information gained from these experiments gives a convoluted measure of many material properties. One of these (other factors, such as strength of absorbtion being equivalent) is the relative strength of of the mercury bonding within the various materials. Not surprisingly the strength of these bonds has been shown to depend both on the material (HgCdTe versus HgZnTe for example), its composition ($Hg_{0.8}Cd_{0.2}Te$ versus $Hg_{0.7}Cd_{0.3}Te$), and its electrical properties (as-grown versus annealed). Theory indicates that the addition of cadmium tends to weaken the mercury bonds, while the addition of certain other elements may actually strengthen the bond.[17] Stronger bonds should result in larger values of t_d for materials with similar bandgaps. Theoretical calculations of bond

TABLE 4-1
Reflectivity Data for As-Grown HgATe Material

Material	x (%)	E_g (meV)	Samples	(t_d)	Std. Deviation σ
HgCdTe	7.5	7.8	4	1.90	0.61
HgCdTe	11.0	65.5	7	0.90	0.70
HgMnTe	10.0	214	2	3.00	0.00
HgMnTe	12.0	280	4	1.60	0.70
HgMgTe	5.1	26.8	4	1.26	0.68
HgMgTe	8.5	122	7	1.59	0.21
HgMgTe	10.3	172.4	12	1.99	0.23
HgMgTe	11.9	217.2	16	2.24	0.38

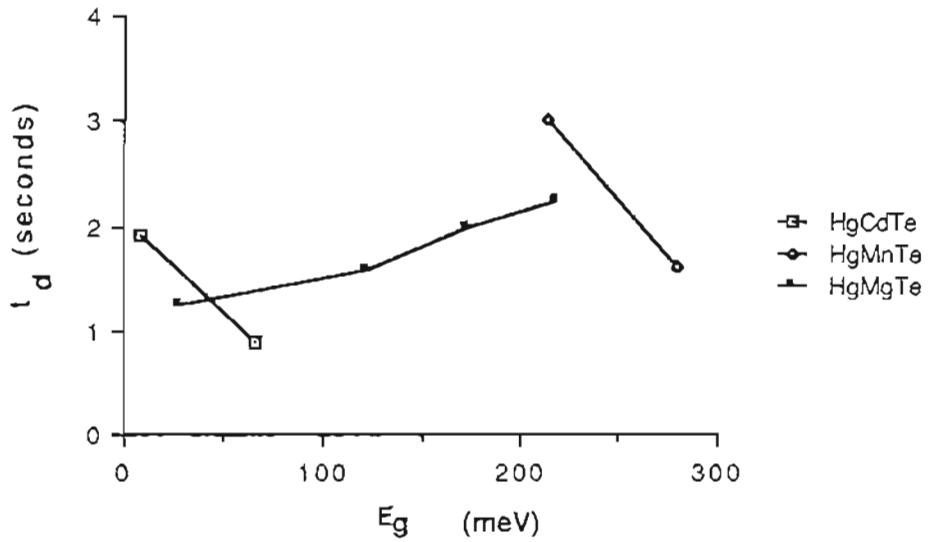

Figure 4-5 For as-grown samples of HgCdTe, HgMgTe and HgMnTe t_d is plotted.

strength for many alternative materials have not been done. In particular such predictions for the popular dilute magnetic semiconductor (DMS) material HgMnTe are difficult to make because of the partially filled D-shell of electrons in manganese. Likewise, no theoretical predictions have been made for HgMgTe. Recent theoretical work adds some understanding to these issues[2] but still experimental verification of these predictions is necessary.

Our results for as-grown samples give HgCdTe as the "strongest" material, with HgMnTe and HgMgTe being somewhat less robust. From figure 4-5 we see that at the same material bandgap E_g, t_d is longer for HgCdTe than for HgMgTe. Similarly HgMnTe has an equivalent t_d even though its E_g is considerably larger. HgMnTe also appears "stronger" than HgMgTe for comparable E_g. Note that throughout this discussion, "stronger" refers to the Hg-Te bond, and not some hardness or tensile strength of the material. Table 4-2 contains the t_d results obtained for annealed samples of HgCdTe, HgMnTe and HgMgTe. This annealed information is presented graphically in figure 4-6, and figure 4-7.

The data for annealed samples may present a more accurate comparison of different materials than the data for as-grown samples. The growth of many of these materials is often a rather haphazard proposition, and two ingots grown under "identical" conditions may turn out vastly different. However, after undergoing mercury vapor anneals, the properties appear more similar. Thus the result that there is little if any difference in the

TABLE 4-2
Reflectivity Data for Mercury Annealed HgATe Material

Material	x (%)	E_g (meV)	Samples	(t_d)	Std. Deviation σ
HgCdTe	10.0	49	8	2.05	0.15
HgCdTe	11.0	65.5	3	2.85	0.15
HgCdTe	12.6	91.9	4	1.2	0.73
HgCdTe	19.5	205.8	8	1.2	0.34
HgCdTe	29.0	362.5	14	1.74	0.43
HgMnTe	7.7	138.1	2	1.78	0.22
HgMnTe	9.2	187.6	3	1.45	0.10
HgMnTe	10.0	214	6	2.70	1.3
HgMnTe	11.0	247	5	1.87	0.12
HgMgTe	6.3	60.4	7	1.39	0.70
HgMgTe	9.0	136	3	1.73	0.03
HgMgTe	12.0	220	6	1.89	0.12

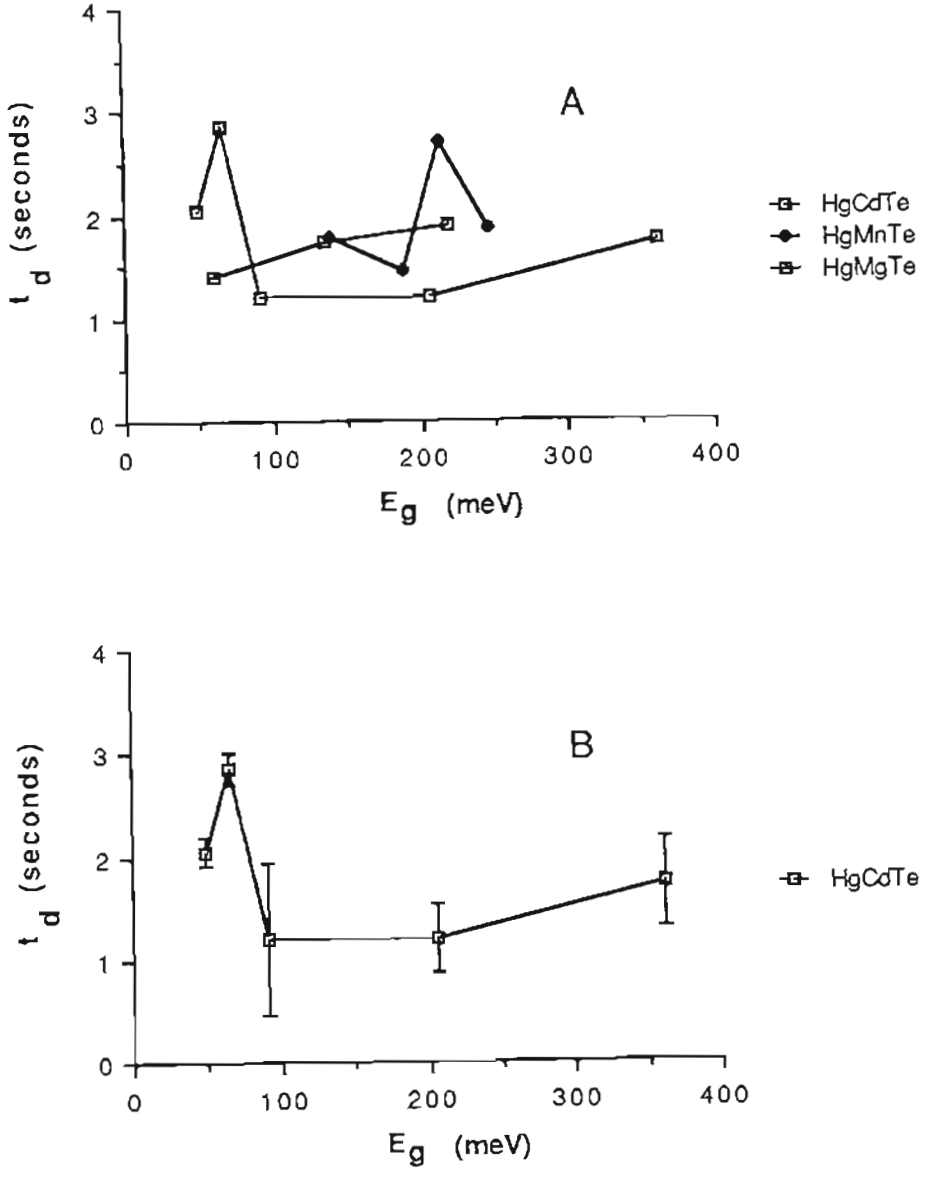

Figure 4-6 For the data sets in table 4-2 an average value was obtained and this value is plotted as a function of the materials bandgap in plot A. The standard deviation for each data set was also calculated. In B these deviations appear as error bars on the average values for HgCdTe. The variance shown is primarily due to non-uniformity of the material rather than experimental variation.

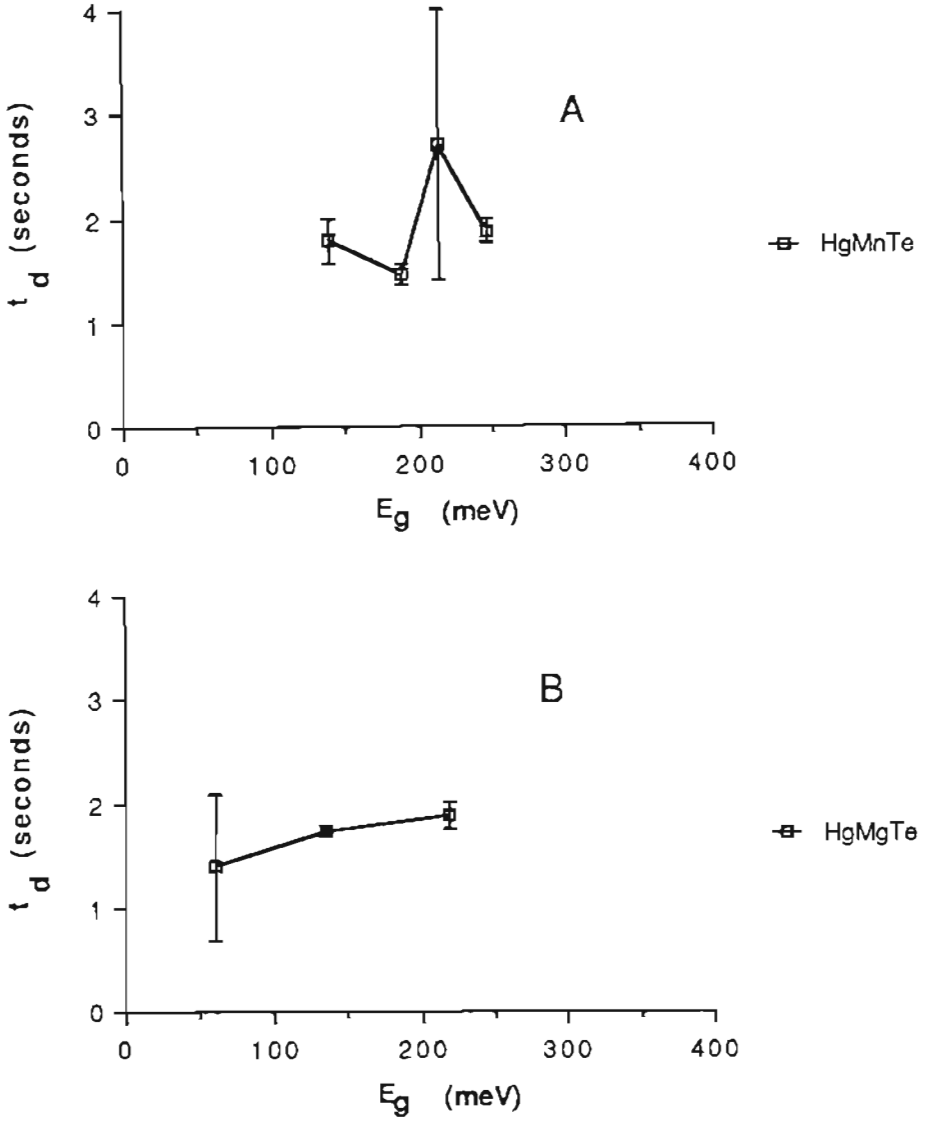

Figure 4-7 For the data sets in table 4-2 an average value of t_d was obtained and this value is shown for HgMnTe as a function of the materials' bandgap in plot A. A similar plot for HgMgTe is given in B.

apparent "strength" of the annealed materials is probably a safer assumption than the ranking made in the as-grown materials.

Recall that annealing HgTe-based materials in mercury vapor usually results in samples that are n-type with a fairly low carrier concentration. These annealed samples should absorb energy from the CO_2 laser less strongly than the as-grown ones. The comparison of t_d versus E_g for several as-grown materials is relatively inconclusive in terms of a comparison between the different materials. Differences between these materials, and even between samples of the same material with different bandgaps are similar to the spread involved in the measurements, as is shown by the error bars in figure 4-6.

HgMgTe materials seem to have a reasonably flat behavior in t_d, both for annealed and unannealed samples in the range of approximately 50-250 meV. The unannealed HgMgTe material can withstand less than one-half second of exposure in the $\lambda_{CO_2} \approx 120$meV region before degrading. Unfortunately unannealed HgCdTe and HgMnTe material with bandgap energies near this range were not available for comparison.

At a slightly lower bandgap energy range HgCdTe seems to become less able to withstand heating with an increasing amount of cadmium concentration. (Remember that an increasing bandgap energy in a material HgATe corresponds to an increase in the fraction of the material "A" in the compound.) This corresponds to theoretical predictions that adding cadmium weakens the Hg-Te bond. For HgMnTe, a similar decrease in t_d with increas-

ing material bandgap occurs in the energy range 225-275 meV. Two factors are playing roles here. As x increases E_g increases, which should result in less absorption and thus greater values of t_d. However, if the addition of "A" material to HgTe weakens the Hg-Te bond increasing x should decrease t_d. Still, for unannealed materials the minimum value of t_d observed for HgMnTe is only slightly below the maximum value of t_d observed for HgCdTe.

In figures 4-6 and 4-7 for the annealed materials, notice that there is a peak in the characteristic times for HgCdTe and HgMnTe at (approximately) 70 and 210 meV respectively. These energies are (respectively) substantially smaller and greater than then energy of photons incident from the CO_2 laser. However, the HgCdTe seems to experience a local minimum in t_d in a material with a bandgap of (approximately) 90 meV. The two HgCdTe compositions with successively higher cadmium concentrations (i.e. greater bandgaps) show no change and a thirty percent increase in t_d respectively. The t_d minimum in material with bandgap close to that of the incident photon energy may be due to a bandgap dependent photon absorption process. However, the increase in t_d with increasing cadmium concentration seems to indicate that there is another composition dependent absorption process in effect, or that the generally accepted weakening of the Hg-Te bond by addition of cadmium is not a monotonically increasing phenomenon, i.e. more cadmium may not always mean weaker bonds.

The maximum in t_d for HgMnTe at 210 meV is proceeded by a

minimum at approximately 190 meV which in turn is proceeded by an increase in t_d at 140 meV. For all of the bandgap energy compositions available in HgMnTe, t_d is larger than the corresponding times for HgCdTe. While this may indicate that HgMnTe is "stronger" than HgCdTe, the experimental error discussed elsewhere makes such a conclusion suspect. At lower energies two compositions of HgCdTe have substantially greater t_d values than in subsequent samples. One of these values, discussed above, is the maximum of the times obtained for any annealed material.

The data for annealed HgMgTe in form generally resembles the data for unannealed HgMgTe. That is, neither set has distinct minima or maxima in t_d. The actual values of t_d for annealed HgMgTe are greater than corresponding values in HgCdTe for the region between 90 and 240 meV.

Of some interest is the spread in the values of t_d obtained for a particular composition of HgATe. This spread is measured by calculating the standard deviation of the data sets and is presented graphically as error bars on data from annealed samples in figure 4.6. Note that HgCdTe seems to have the largest number of compositions whose measured t_d values have a significant spread. Also note that for HgCdTe and HgMgTe the largest deviation occurs at a local minimum in t_d and is then followed by a monotonic increase in t_d. For samples of annealed HgMnTe the largest spread in data occurs at the series maximum, and it is the largest spread of any data set.

Data for HgCaTe and HgSrTe is shown in tables 4-3 and 4-4 and summarized in figure 4-8.

TABLE 4-3
Reflectivity Data for As-Grown HgSrTe and HgCaTe

Material	ρ (g/cm^3)	Samples	(t_d)	Std. Deviation σ
HgCaTe	8.01	8	2.80	0.20
HgCaTe	7.98	8	2.95	0.48
HgSrTe	7.99	7	4.38	1.27
HgSrTe	7.90	7	2.00	0.57

TABLE 4-4
Reflectivity Data for Mercury Annealed HgSrTe and HgCaTe

Material	ρ (g/cm^3)	Samples	(t_d)	Std. Deviation σ
HgCaTe	8.04	9	3.78	0.25
HgCaTe	7.87	9	3.63	0.15
HgSrTe	7.99	9	3.51	0.20
HgSrTe	7.93	5	3.41	0.25

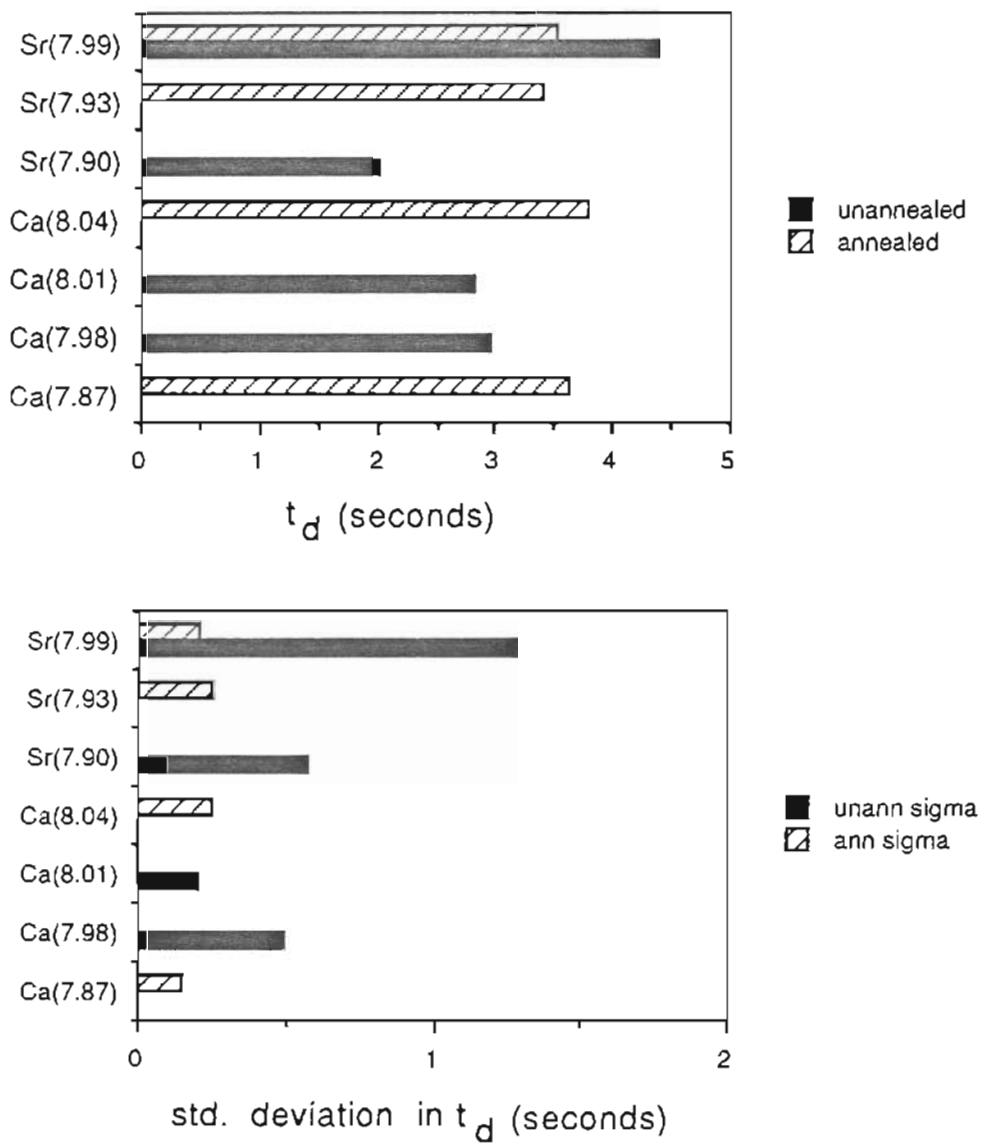

Figure 4-8 In the topmost plot exposure times are compared for several different compositions of HgCaTe and HgSrTe, note that for the annealed materials the values tend to be greater and more uniform than for the unannealed samples. In the bottom plot the standard deviations in the data sets are shown. Note here that the deviations in the annealed materials tend to be shorter and more uniform.

Recall that we have no information from either the literature or our own FTIR measurements concerning the variation of E_g or ρ with x. Thus the characteristic time t_d is shown plotted as a function of the measured mass density. As was the case for the better-known materials discussed previously annealing in mercury vapor tends to produce more uniform results, both within a particular material and between materials. The values of t_d for these two materials are significantly larger than those for any other material. However, lack of information about E_g makes direct comparison meaningless.

Other factors (i.e. laser power, sample preparation, etc.) being carefully controlled it seems that these spreads in t_d need to be explained in terms of variation in material properties within the samples making up the data set. A most likely explanation, in light of considerations to be discussed in chapter five, are differences in the absorption of the incident photons by the samples. The heating induced by the laser will be shown to be strongly dependent on the attenuation of light at the laser's wavelength. Strong absorption causes greater local heating at the surface of the material and could conceivably alter the onset of local melting and mercury loss. One mechanism controlling the attenuation of light is the carrier type of the material. Samples which are p-type experience greater intra-band absorption which can increase the attenuation of incident light. These concerns will be discussed further after results from another characterization technique are presented.

We have shown and discussed data from annealed samples separately

from that for as-grown samples. As discussed above, we would expect the annealed samples to be more uniform, and to generally have larger values of t_d. Figures 4-9 and 4-10 compress the annealed and as-grown data for materials where such a comparison of values is possible. The actual mechanisms causing the fluctuation in t_d for the various materials are of basic interest. However, it is the absolute values of these times that are of practical concern in designing a process utilizing laser irradiation of HgATe. The assumption of greater uniformity is certainly shown, however annealing does not always result in longer values of t_d. Such comparisons, of course, are not rigorous, since different samples are used for annealed and as-grown measurements. Variations within an ingot can easily produces differences as great as those seen in figure 4-6.

4.3 Uniformity of Materials -- Seebeck Mapping

The problem of producing bulk $Hg_{1-x}A_xTe$ material that meet homogeneity requirements have already been discussed. Not only is it important for the material composition (x value) to be uniform, but the resulting electrical properties of the material should share this uniformity. Unfortunately since the electrical properties are controlled by mercury vacancies, interstitials and other defects, knowing a material's composition, x to several significant figures is not enough.

Hall measurements yield the sort of information that is needed, however the multiple-probe requirements of this technique make it somewhat cumber-

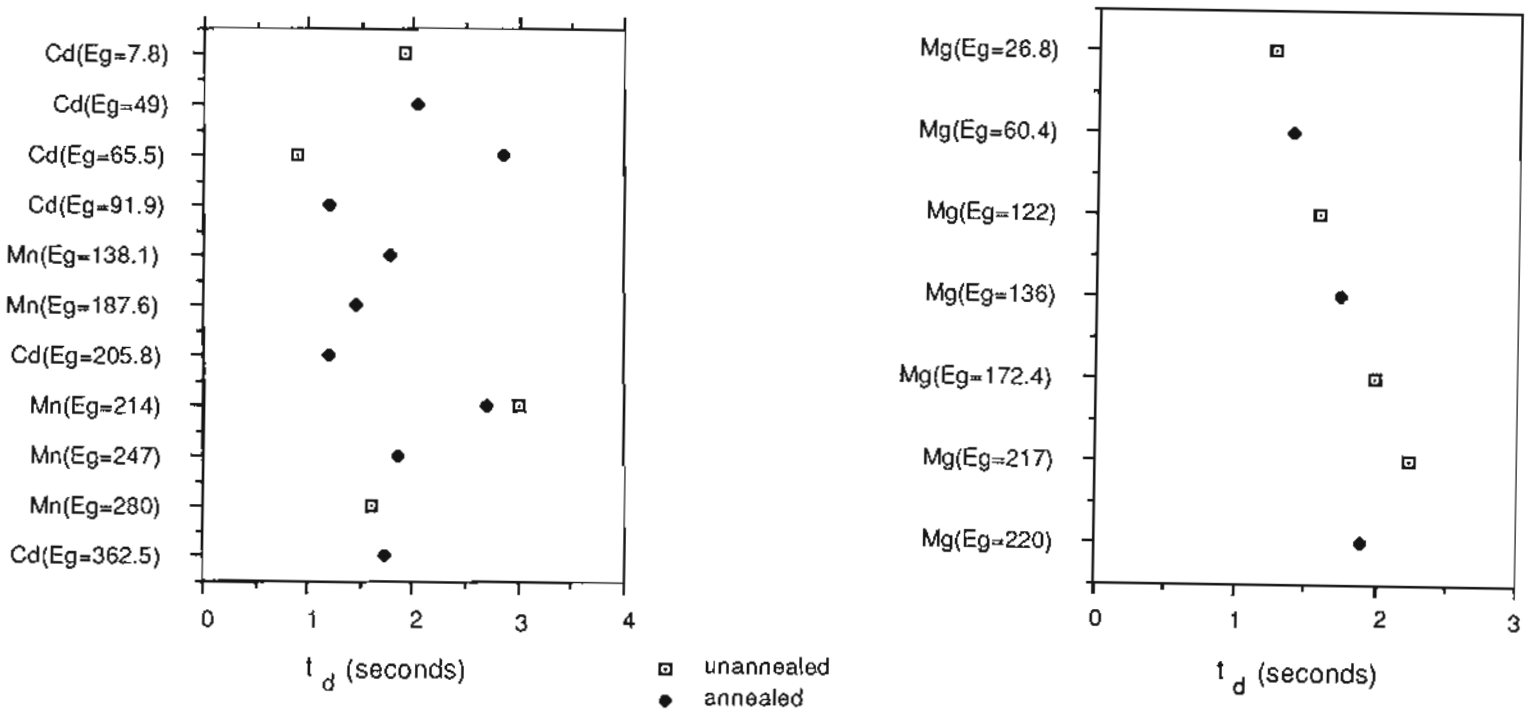

Figure 4-9 The scatter plots are arranged in order of increasing material bandgap. The left plot combines HgCdTe and HgMnTe, while the right plot is only HgMgTe. There is little structure apparent in the mixed plot but for HgMgTe there appears to be a trend toward increasing values in t_d with increasing E_g.

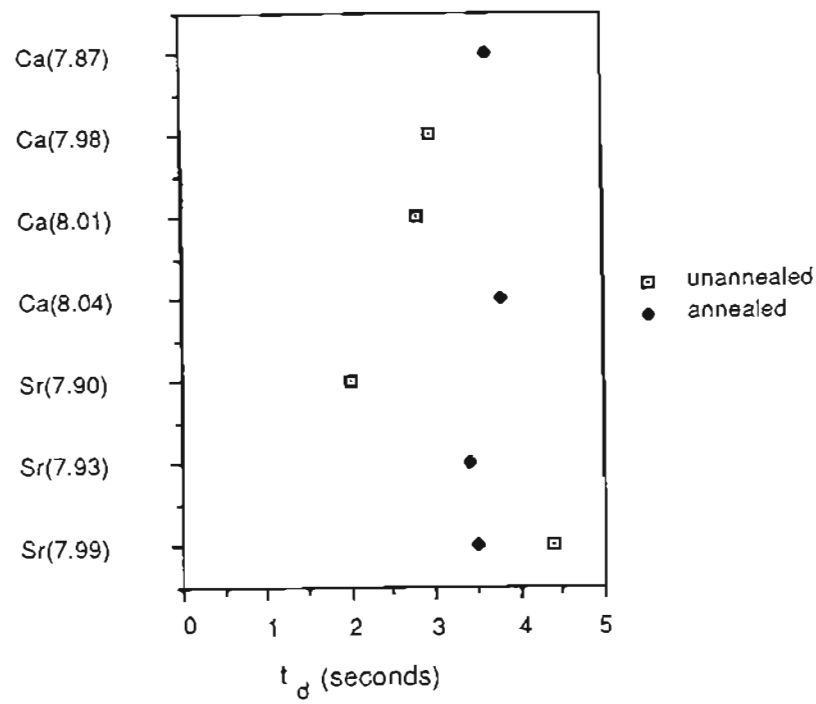

Figure 4-10 This plot shows a strong uniformity in times for annealed samples of HgSrTe and HgCaTe. The unannealed samples, too, show less scatter than HgCdTe materials for example. These materials are arranged by mass density since determination of x-values for them proved impossible.

some. It is difficult to make multiple Hall measurements at different locations on the surface of a sample, thus the information the measurement yields suffers from a lack of spatial resolution. Other techniques are available to give a higher degree of resolution, though typically these measurements are significantly more complicated in terms of both interpretation and instrumentation.

A common technique used to give a qualitative measure of a semiconductor's conductivity type is based on the Seebeck effect. A number of authors mention this technique in passing,[57,58] and it has been identified as being an important complement to Hall measurements[59] since it can be used to give an indication of material uniformity. From figure 4.1 sequence C was undertaken using this method. Appendix I includes a discussion of this non-equilibrium phenomena, and in this appendix figure I-1 gives a simplified block diagram of the procedure. Figure I-3 demonstrates how several minor refinements can be made. The effect of contacting a semiconductor sample with two probes which are maintained at different temperatures is to generate a voltage. The polarity of this voltage depends on the majority carrier type of the semiconductor in the non-trivial manner described in the appendix I.

The block diagram in appendix I figure I-2, shows the final set of instrumentation needed to perform the experiment. Using either of the probe arrangements noted in figures I-3A or I-3B the surface of a sample may be contacted at a number of locations and the generated voltage recorded at each. The information thus gathered can be displayed in a manner that will

allow one to interpret the variation in measured voltages in terms of uniformity of electronic properties over the sample's surface. Note that it is now possible to sample along a single (multiple) imaginary line(s) across the surface of a sample. The former procedure yields information in one dimension, the latter in two dimensions.

4.3.1 Diffusion Studies With 1-d Seebeck Measurements

These measurements were the first attempted and were made without the aid of much of the instrumentation detailed in appendix I. The experiment was designed to generate information about the rate at which mercury diffuses into $Hg_{1-x}Mn_xTe$ during a thermal anneal in mercury overpressure.

A number of prepared samples were characterized to be p-type by Hall measurements. The samples were placed in an ampoule connected to a roughing pump and the ampoule was evacuated to approximately 40 millitorr. The ampoule was placed in a furnace and the temperature ramped to 300C in 30 minutes. The temperature was maintained at 300C with the pump running (dynamic vacuum) for three hours. The ampoule was then removed from the furnace and allowed to cool in air to room temperature. The cooling process took approximately 30 minutes after which the vacuum was broken and the samples removed from the ampoule. The combination of elevated temperature and vacuum has been documented to deplete the samples of mercury creating mercury vacancies and thus rendering the samples even more p-type.[60] Representative samples were then characterized by Hall measurements again, which confirmed the depletion of mercury.

At this point the remaining samples were divided among three ampoules each containing mercury. The ampoules were sealed at atmospheric pressure and each ampoule was placed in a furnace whose temperature was maintained at 300C. Over the course of the next three weeks, samples were removed from each of the furnaces on a regular basis. The remaining samples were immediately returned to the furnaces and allowed to continue the mercury overpressure anneal.

After the last of the samples was removed they were quickly Seebeck probed. Without exception the surfaces were n-type. Next attempts were made to cleave the sample in half, with the intention of doing etching studies[61] on one of the halves, and Seebeck probing on the other half. Luckily all of the samples yielded at least a single half, though the remaining portion was more often than not in several pieces.

The halves of the samples were next fastened to a jig having a 3° bevel, then lapped until only approximately one millimeter of the original surface remained. The samples were then polished and etched in the standard fashion. A block diagram of the beveled sample arrangement and the points at which the sample was probed is given in figure 4-11. The effect of probing down the bevel is to measure the depth to which mercury has diffused. Thus, knowing the length and temperature of each sample's anneal it is possible to make a comparison of the diffusion rate in HgATe to data available for HgCdTe.[60]

This sort of measurement is normally used to determine junction depth.

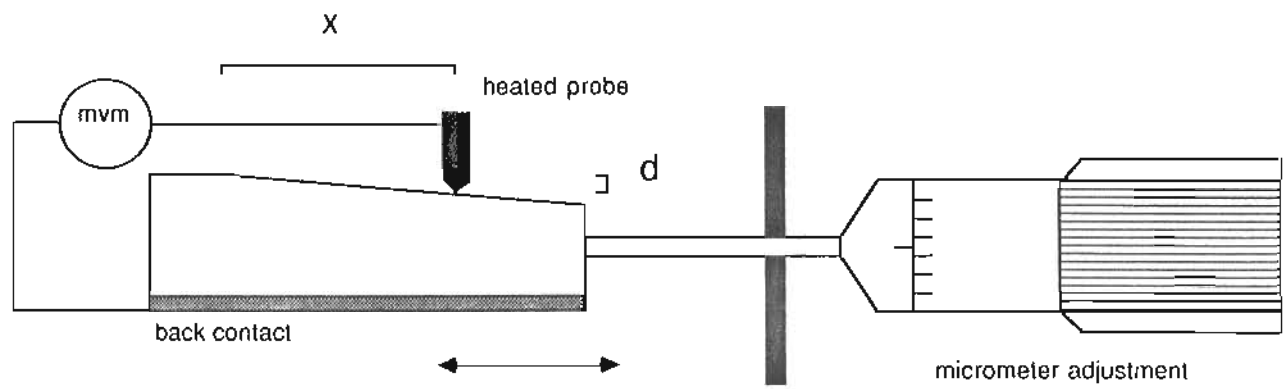

Figure 4-11 The system used to measure the thermal voltage generated in the semiconductor by the heated probe. The polarity of this voltage indicates the carrier type of the material. Beveling the sample and probing down the bevel allows determination of the depth to which mercury has diffused.

That is, the material begins p-type and the indiffusion of mercury produces a n-type region and consequently a n-p junction. By probing down a sample's bevel one should measure n-type voltages until the depth of the mercury diffusion front is passed, subsequent measurements will be p-type. The junction is said to occur at some depth between these two points.

The junction depths observed in these measurements are correlated to those observed by Jones et al[60] in figure 4-12. Since this work other studies modeling the diffusion of mercury into HgCdTe have been done.[53] The studies agree reasonably well with Jones' work. We probed annealed HgMnTe samples at only four locations along the bevel[62] that was produced. This analysis was carried out only for HgMnTe. As shown in figure 4-11, 300C anneals produce in-diffusion rates similar in HgMnTe and HgCdTe.

4.3.2 Diffusion Studies Using Etching

Another technique that was undertaken was an etching study to detect the defects generated when mercury vapor diffuses into HgMnTe. Studies have reported success in cleaving and preferentially etching annealed samples to reveal a diffusion front as it moves into a p-type sample of HgCdTe.[61] Cleaving these materials is not a straightforward undertaking. HgCdTe and to a lesser degree its sister materials are more ductile than brittle.[63] and obtaining a smooth surface from cleaving proved to be a hit or miss proposition, failing miserably on most samples.

The preferential etch is itself a problem. Of the several etches used in

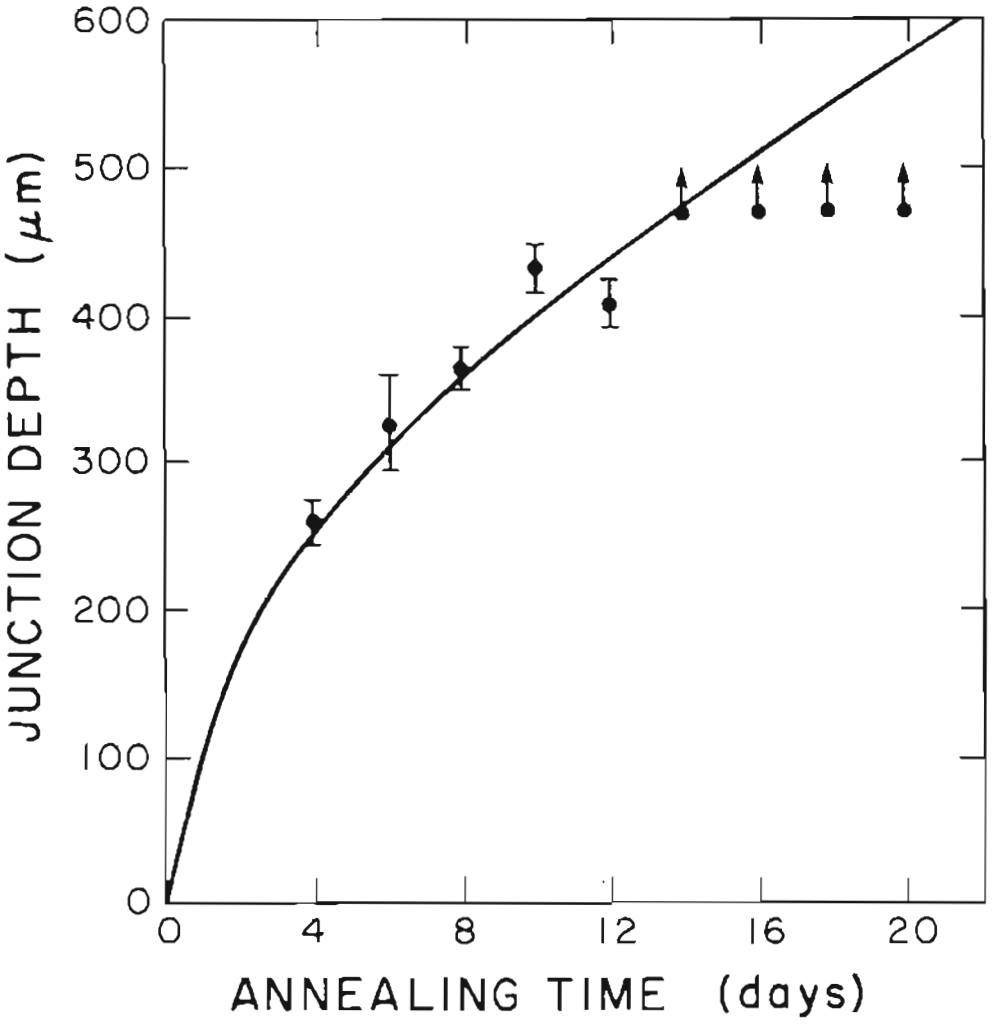

Figure 4-12 Junction depth is measured using the probing arrangement given in figure 4-11. The data points are for samples of HgMnTe annealed at 300C. The solid line is obtained from Jones et al and represents a similar determination for HgCdTe annealed at 300C. The data points with arrows indicate that the sample was completely converted to n-type, so the actual junction depth was greater than half of the sample thickness.

studies,[64-66] most were originally developed for CdTe. Though they work reasonably well for HgCdTe, none proved viable for HgMnTe. Etches tried on HgMnTe included: Polisar #2,[64] and an etch detailed by Bagai et al.[65] These etches were intended to decorate dislocations. Instead they tended to produce a smooth polished surface.

4.3.3 Uniformity Studies Using 2-d Seebeck Mapping

The one dimensional probing described in the previous section can be repeated at intervals across the surface of a sample yielding a two dimensional set of data. To facilitate the large amount of data collected, the system can be automated with the data being stored by a computer for later retrieval and analysis. Appendix I contains a description of the system developed. Samples to be mapped were prepared in the standard manner, describe in appendix E, then attached to an aluminum holder to facilitate handling. For the probe arrangement described in appendix I figure I-3A an electrical contact was made to the aluminum holder by means of a silver paste (DuPont #7941). The paste is soluble in butyl acetate and when applied must be cured at elevated temperatures (75C for 20 minutes). For the probe arrangement in appendix I figure I-3B no electrical contact to the aluminum was necessary and the samples were mounted using rubber cement.

After mounting, the sample/holder is fastened to a x-y translation stage and the Apple computer was told to run software that allows for manual control of the stage. When run, the sampling program generates an

imaginary grid within a one centimeter square region. The sample must first be manually positioned within this square region. When this is done the sampling routine is run. The routine first completely retracts the probe arrangement and then positions the stage so that the center of the sampling region is beneath the probe. An initial measurement is taken and stored. The probe is then lowered one step and a measurement taken. This measurement is compared with the first measurement and if there is sufficient difference between them it is assumed that the probe has contacted the sample. If there is insufficient difference between the two measurements the probe is lowered another step and the process repeats until the sample is contacted. When this occurs the number of steps which the probe has been moved is recorded, the probe is then retracted and the stage repositioned at the corner of the sampling region. The probe is then lowered number of steps determined above, a measurement is taken and stored, the probe is raised and the stage positioned for the next measurement. This process repeats until the entire sample region has been measured, the program inquires for the sample name, and stores the information on disk in a filename derived from the sample name. Variations on this software are available and appendix I contains printouts of the various sampling, plotting and analysis programs. The software was adapted from a system designed to optically map stress and EL2 concentration in semi-insulating GaAs.[67]

4.3.4 Interpreting a Two Dimensional Seebeck Map

The final step in the mapping of a surface is to use a pen plotter to generate a two color hardcopy map of the data. Figure 4-13 shows a typical map and an explanation of the grey scale used. As discussed in appendix I the polarity of the measured voltage indicates the carrier type of the material in a region surrounding the heated probe. Thus, for the purposes of this analysis the data has been taken in such a manner as to record positive voltages when the material is p-type and negative when the material is n-type. Notice that for black and white reproduction purposes the p/n-type regions of the sample have been delineated by a black line. The grey scale remains unchanged: the more black plotted in an n-type (p-type) region the larger the negative (positive) voltage.

Three plotting parameters can be adjusted on the basis of experience to allow easier interpretation of the data. Without exception only maps plotted with identical parameters will be compared. The plotting parameters are all measured in volts, and are given a graphical interpretation in figure 4-13. The junction sensitivity is adjusted to give a dead region about zero measured voltage. Points whose measured voltages are within this region are indicated by full white on the aforementioned scale. The false zero parameter is used to adjust the short circuit voltage to zero. Since there are resistances and temperature difference across various metals in the circuit small voltages are generated. These voltages are additive to the true Seebeck voltages and may be removed by this software tuning. Lastly, the step size sets the width, in volts, of each grey scale step.

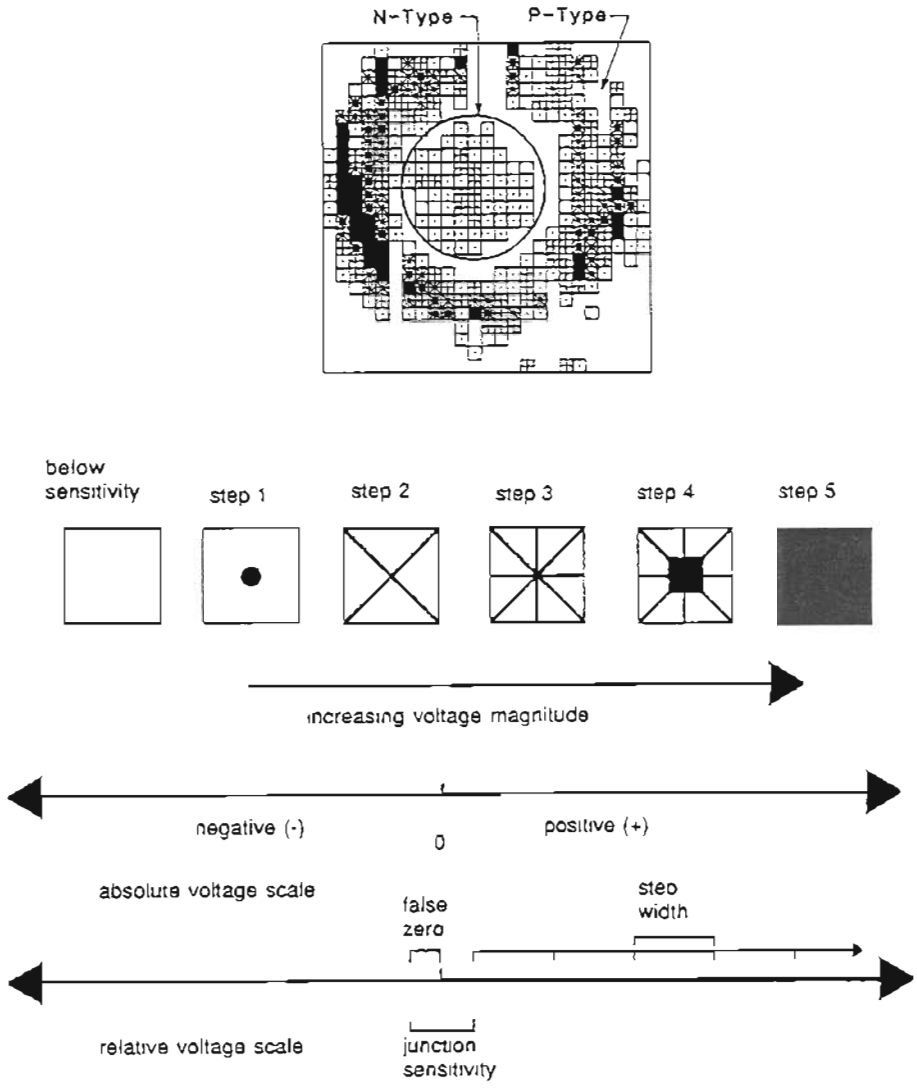

Figure 4-13 The map above is created by depositing ink in the indicated patterns. Each pattern represents a voltage falling somewhere within a step (measured in volts), as shown on the voltage scale.

The map in figure 4-13 is of an as-grown sample of HgMnTe with $x = 0.11$. The lack of uniformity on the surface of this sample is more or less typical of material in the as-grown condition. The first observation is that there are distinct regions of p and n type material with radial symmetry, that of a central n-type region surrounded by p-type material. Notice too, that in the outermost edge regions there is a tendency for a p-type voltage maximum. Over the course of mapping various samples several patterns emerged. Examples of each of these are given in figure 4-14 and will henceforth be referenced by an arbitrary number. For example the map in figure 4.13 is of type four. Notice also that many of the maps have a white region at twelve o'clock position. Several ingots were notched prior to sectioning which enabled us to orient the slices later. This notch manifests itself as a zero voltage region in the maps.

Maps of type one are, without fail, from as-grown material, and are uniformly p-type. The p-type voltage is typically very small. Maps of type two show samples that are n-type, but which have a fairly non-uniform appearance. Across the surface of these samples the Seebeck voltage will vary across several gray-scale steps. Maps of type three display a rather confused pattern of n-type regions and p-type regions. There tend to be areas with a high p-type Seebeck voltage, but no corresponding regions of high n-type voltage. Maps of type four display an amazing amount of radial symmetry, always having a central n-type region and a surrounding p-type region. This type of map is discussed in more detail later in chapter four. Maps of type five appear to be a degenerate form of type four maps. The central n-type

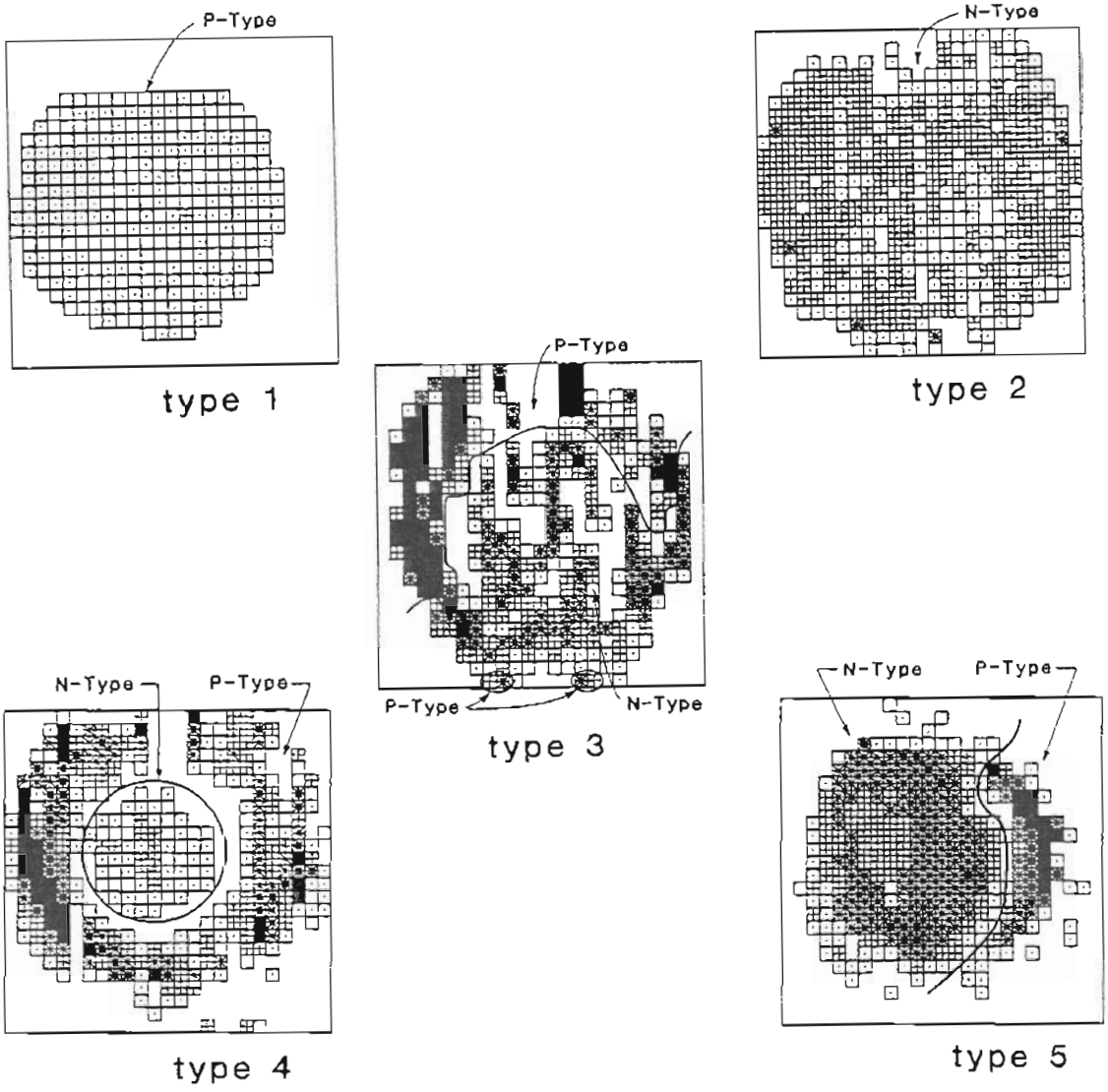

Figure 4-14
Type 1: The surface of an as-grown sample is sometimes found to be completely and fairly uniformly p-type.
Type 2: The surface of an as-grown sample is sometimes found to be completely but not uniformly n-type.
Type 3: The surface of an as-grown sample is sometimes a mosaic of p-type and n-type regions.
Type 4: This type of map, shown earlier, displays a great deal of radial symmetry. There is no corresponding map-type with a p-type region surrounded by an n-type region.
Type 5: This type of map appears to be a degenerate version of type four. The radial symmetry has been upset and within the n-type region there is a region which is just on the verge of displaying n-type behavior.

region appears to have expanded and moved off center. Again, this type of map is discussed later in the chapter.

At this point the effect of surface preparation techniques need to be discussed. The surface preparation of several samples was changed to try to induce changes in the subsequent Seebeck maps. The standard sectioning, lapping, polishing and etching processes discussed in appendix E were altered drastically. A typical sample of HgMnTe was chosen, and mapped after a standard preparation process. The sample was then lapped and polished repeatedly. After each lapping and polishing a different processing step was employed. These steps included:

- two minutes in Polisar etch #2
- two minutes in 5% Br-methanol etch
- lapped but not polished to an optical finish

Without fail the fingerprint pattern (map type 1-5) of the sample remained unchanged. Regions that began p-type remained p-type with approximately the same measured Seebeck voltage. Regions that were initially n-type remained n-type with approximately the same measured Seebeck voltage. The Seebeck mapping measures a voltage across a region of the sample where there is a non-zero temperature gradient. This region extends some distance below the surface, so it is not surprising that this bulk measurement is affected only sightly by different surface treatments.

Hall measurements also indicate that the preparation process is not being measured by these Seebeck maps. Hall work was done on samples that were subsequently mapped and determined to be of type three. These Hall

results indicate a sample of mixed conductivity type. Hall measurements for samples mapped to be type two indicate n-type conductivity, and for samples mapped to be type one indicate p-type conductivity. Secondly, to be discussed later, the mapping techniques correctly tracks the outdiffusion and indiffusion of mercury that occurs during thermal anneals.

Even assuming that the standard analysis (summarized in appendix I) holds, interpreting variations in the Seebeck voltage across the surface of a semiconductor sample is not straightforward. In regions where the magnitude of the measured voltages is at a maximum, it is safe to assume that the material is essentially unipolar. With this understanding then, for maps of type four it would seem that there is n-type conduction, such as that caused by mercury interstitials, near the center of the sample and p-type conduction, caused by mercury vacancies,[53] near the edges of the sample. In terms of material composition then there is excess mercury near the center and insufficient mercury near the edges. If this is the case and if we assume a uniform distribution of "A" atoms in HgATe, the bandgap of the sample, which is determined by the ratio of "A" to mercury atoms, should be a maximum near the edges and a minimum near the center. Work done by Bartlett[10] et al examined cut-on wavelength λ_{co} across the diameter of HgCdTe, slices and along the length of the ingot. Their results are reproduced in figure 4-15. In terms of material composition cut-on wavelength is related inversely to the concentration of "A" in HgATe. The greater the x value for the material the larger the bandgap and the smaller the wavelength. Thus slices with λ_{co} higher in the middle have less "A" atoms

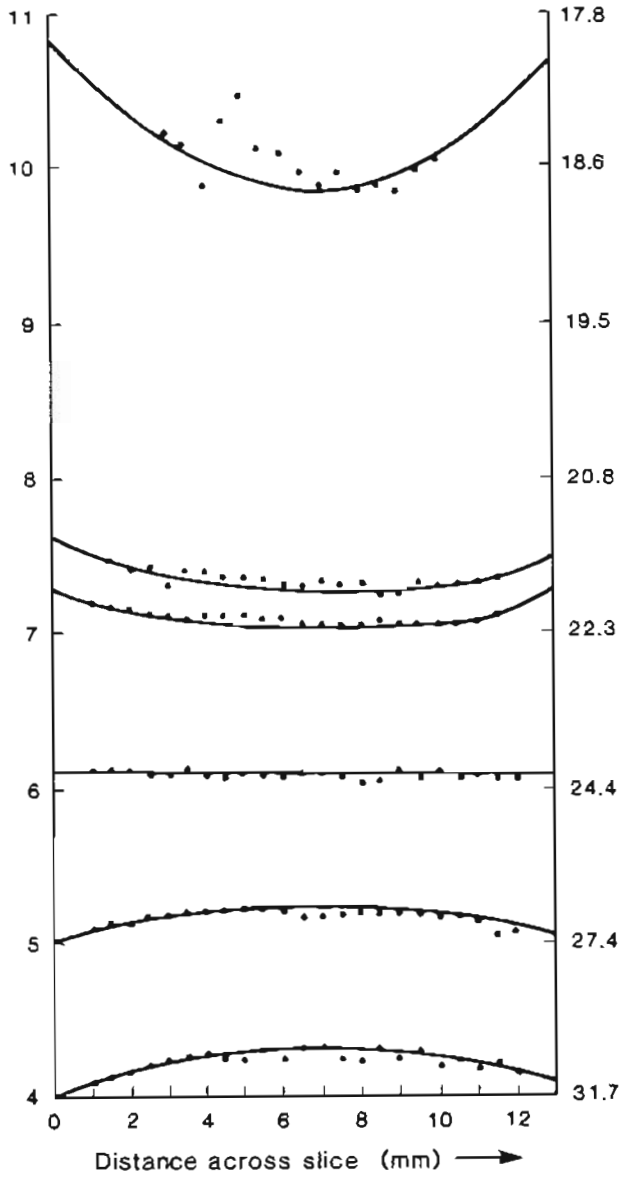

Figure 4-15 In HgCdTe, segregation, dependent on growth rate, occurs and generates material whose composition varies both radially and axially. This variation can be measured using infrared spectroscopy to determine cut-on wavelength versus position across a sample and within various samples coming from different regions of the ingot.

and fewer mercury atoms in the center. Likewise, regions with lower λ_{co} correspond to areas with relatively less mercury and more "A". With this understanding, the mechanism resulting in the variation in cut-on wavelength described by Bartlett[10] can be extended to explain this systematic variation in carrier type.

Figure 4-16 gives a series of four maps from as-grown samples of HgMnTe. The samples were taken from the first-to-freeze end through the last-to-freeze end. A density-driven, convective flow would result in the center of the first-to-freeze end of the boule being mercury rich (compared to the rest of the sample), while the center of the last-to-freeze section would be mercury deficient. Excess mercury tends to drive the material toward n-type behavior, as well as making x smaller, hence the variations noted in figure 4-16. Maps of types 2-4 can result from a non-symmetrical radial temperature distribution within the furnace, causing non-symmetrical convection within the ampoule. Since the ampoules are not rotated during growth this lack of uniformity would be frozen in and reflected in subsequent Seebeck mapping.

Interpretation of a map is more difficult in regions where the measured voltage, and hence the carrier type, changes significantly between adjacent measurements. Following the reasoning in appendix I, the next and final level of interpretation will be the understanding that somewhere between regions that are clearly p-type and regions that are clearly n-type there exists a p-n junction. The location of the junction is said to be between measurement points showing different polarities. The Seebeck mapping technique is interesting in its own right. However, further discussion concerning it will be

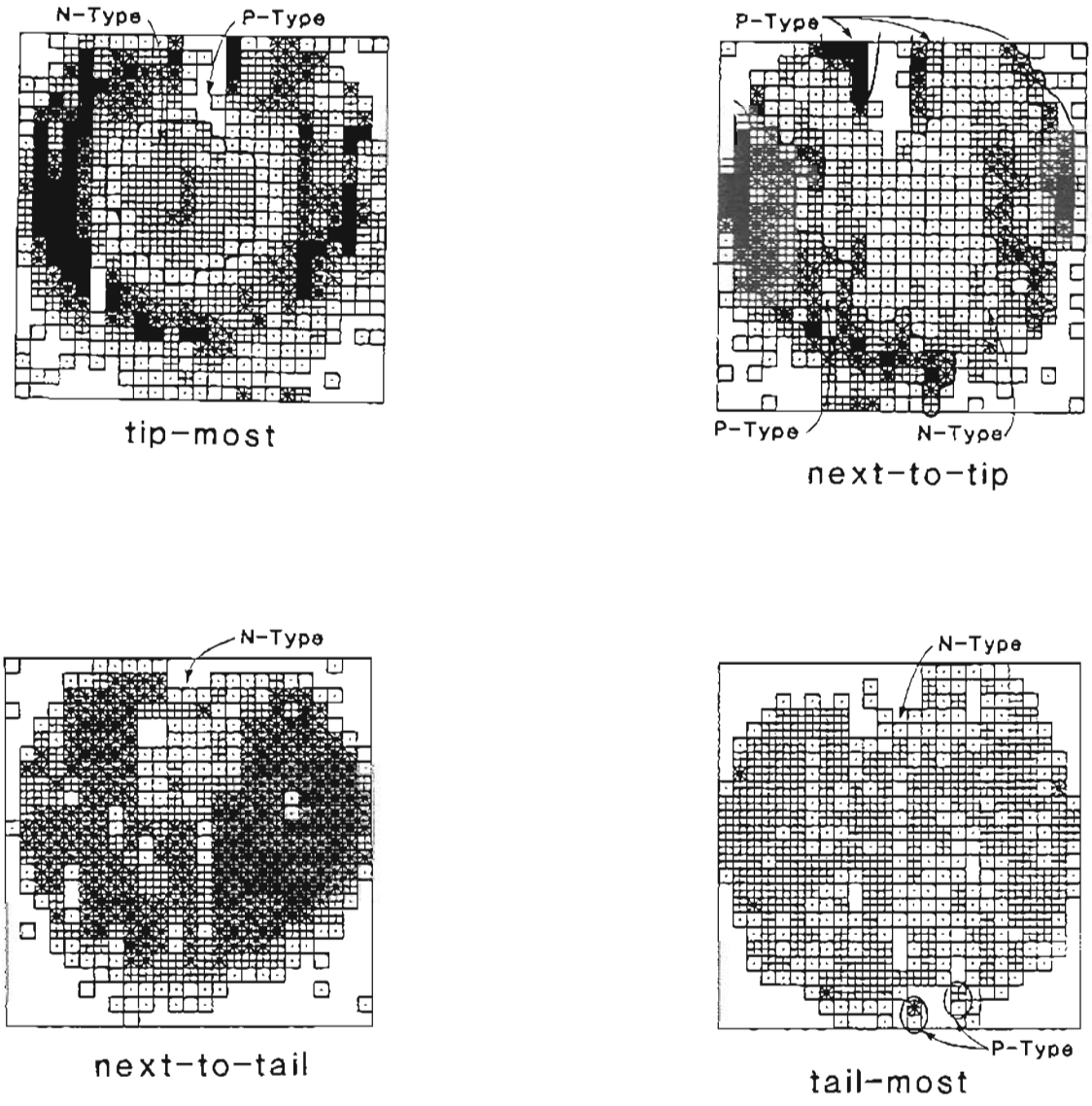

Figure 4-16
Tip-most: This sample of type four is typical of those which come from the first-to-freeze end of HgMnTe growths. The radial symmetry is also visible on samples immediately adjacent to this one.
Next-to-tip: This type three map can be seen to have some radial symmetry. This sample was two centimeters closer to the last-to-freeze end than the previous sample.
Next-to-tail: Continuing approximately one centimeter towards the tail of the ingot a map of type two is obtained.
Tail-most: One centimeter further towards the tail of the ingot another map (basically) of type two is obtained.

limited to the results obtained in its application to examining samples at various stages of preparation.

Initial experiments involved mapping samples after every step in their processing. Figure 4-17 shows a typical series of maps for a particular sample. Note that the as-grown sample may have adjoining regions of p-type or n-type behavior. A subsequent anneal in dynamic vacuum results in mercury outdiffusion and consequently uniform p-type material. Next, a standard mercury overpressure anneal results in the indiffusion of mercury and a uniform inversion to n-type behavior.

If the above process is altered slightly, and the mercury anneal halted before conversion to n-type behavior has been achieved an interesting phenomenon is observed after subsequent exposure to a CO_2 laser. Figure 4-17B shows the map of a sample after vacuum annealing and figure 4-17C after a subsequent mercury anneal. The sample was then mounted on a LN_2 cold finger, and exposed to the CO_2 laser for 45 seconds at 5 watts of power. This corresponds to (a maximum of) 225 joules of energy being pumped into the sample. The sample was remapped and the result is given in figure 4-17D.

The annular regions that have arisen can be explained in terms of a lateral diffusion of mercury away from the beam spot. Notice that in figure 4-17D the center of the annular regions shows a higher Seebeck voltage than the same region in figure 4-17C. Indeed this region more closely resembles the map in figure 4-17B, taken after the sample was annealed in dynamic

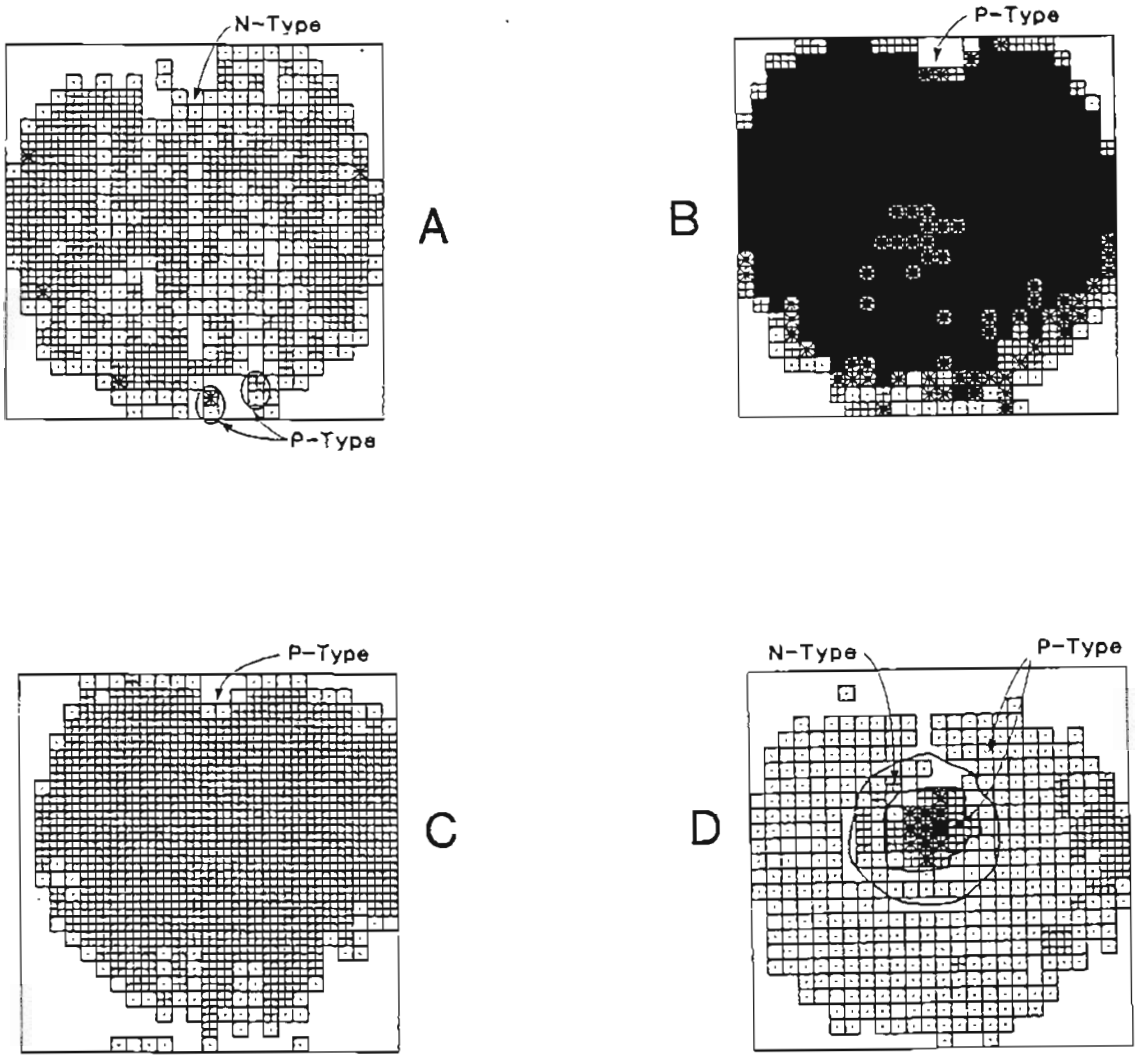

Figure 4-17
A: The as-grown sample displaying a type two fingerprint, with the exception of four points near the edge of the sample.
B: An anneal in dynamic vacuum at 300C produces a material that is greatly depleted of mercury. The mercury vacancies act as acceptors, consequently the Seebeck map shows a material that is very strongly p-type.
C: Strongly p-type sample annealed in an overpressure of mercury. In-diffusing mercury settles on mercury vacancies, reducing the acceptor concentration and altering the material towards n-type behavior.
D: HgMnTe sample having experienced electrically significant amounts of lateral mercury diffusion. The sample was cooled on an LN_2 coldfinger and exposed to a cw CO_2 laser for sixty seconds.

vacuum to deplete the surface regions of mercury.

Apparently the temperatures and temperature gradients generated by the incident laser beam have depleted this center region of mercury. Where did this mercury go? Evidently very little of the mercury left the sample as tests with the Jerome mercury vapor detector show no mercury vapor (at detectable levels) in the sample chamber during laser exposure. Recall that this was not the case with samples not attached to the cold finger during laser exposure. The surrounding n-type region in figure 4-17D provides the necessary clue.

Since p to n conversion is normally accomplished through the elimination of mercury vacancies and the creation of interstitials the logical conclusion is that mercury has diffused outward from the center of the sample and settled in the surrounding annular region. Notice too, that the outermost regions of the map in figure 4-17D show little change from figure 4-17C, indicating that there has been no change in material properties at this distance from the laser spot.

Material was removed from the surface of this and other samples subjected to the same procedure, and the newly exposed surface remapped at higher resolution. The result from a typical remapping at a depth of 70-80 microns is given in figure 4-18B, the map before lapping is given in 4-18A. The redistribution of mercury is clearly not a surface effect since this map shows the same pattern as the map of the original surface.

An extensive literature search found only a single reference[68] concerned

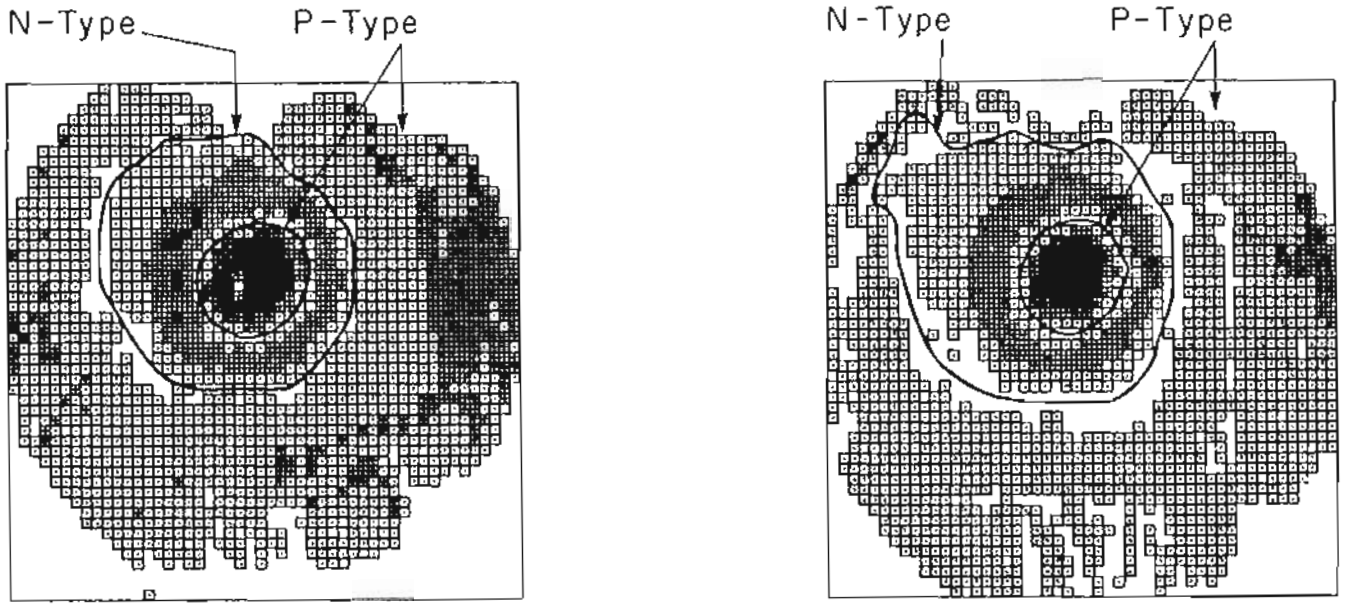

Figure 4-18 The sample from 4-17D was remapped at a 50x50 resolution. The same fingerprint is clearly visible on the left map. The sample was then lapped to a depth of approximately 70 microns and remapped. The fingerprint of the two maps remains the same, indicating that electrically significant mercury diffusion occurs in the bulk rather than only in a thin surface layer.

with laser induced diffusion in semiconductors. This work was of limited interest since it deals with pulsed laser exposures and does not consider the effects of cw irradiation. From the dimension in the maps in figures 4-17 and 4-18 (the outer square being one centimeter across) it is clear that diffusion has occurred over distances approaching a millimeter and has done so in under a minute. The diffusion front generates a p-n junction which moved from r=0 to r≈1000 μm during the 45 second exposure. This rate of travel is several orders of magnitude larger than values reported for HgCdTe[60] or HgMnTe.[62] Clearly, laser induced diffusion produces an effective p-n junction movement several orders of magnitude greater than furnace annealing.

The samples on which laser induced diffusion was initially seen were uniformly p-type as a result of an anneal in dynamic vacuum followed by an anneal in mercury overpressure. Other samples that, as grown, were uniformly p-type were put through the identical procedure as detailed above. In these samples, for exposure times up to and exceeding those used on the annealed samples, no lateral mercury diffusion was detectable. Further, maps of these samples after exposure to the laser were not discernibly different from maps made before the exposure. Eventually, with lengthy exposures, the surfaces of these samples began to show damage.

This is one instance where the processing history of a particular sample has a profound influence on subsequent behavior. We have no firm information as to why only thermally annealed samples display lateral mercury diffusion during laser annealing. If the thermal processing (mercury overpressure anneal) allows for easier redistribution of mercury atoms within the

material then the lack of mercury loss from the surface argues for a very large surface barrier.

It is worthwhile to point out that substantial work has been done to measure loss rates of mercury from HgCdTe.[6,69,70] However, only work from this study has documented the possibility of redistribution of mercury within HgTe based psuedo-binaries.[71]

4.4 Hall Measurements

The literature reports a number of thorough Hall studies on HgCdTe.[72,73] The Hall techniques that have been used in this investigation are not elaborate ones. The instrumentation is basic but the sample holder is somewhat unique. Because characterization was necessary between a variety of processing steps the contacting process was important. Standard metallization/soldering techniques were undesirable and instead a delicate pressure contact system was designed. The sample holder embodied this system and with it one can make four radially symmetrical contacts to a samples of various diameters and thicknesses in a repeatable fashion. This contacting process is as unintrusive as possible, and allows the characterized sample to undergo further processing with a minimum of damage. A simple one carrier model was employed for the analysis of most material, though for ion implanted samples a one carrier/layered structure model was used.[74]

Hall data for annealed HgCaTe, HgSrTe and HgMgTe was taken and is presented figure 4-19. The mobilities and carrier concentrations in these

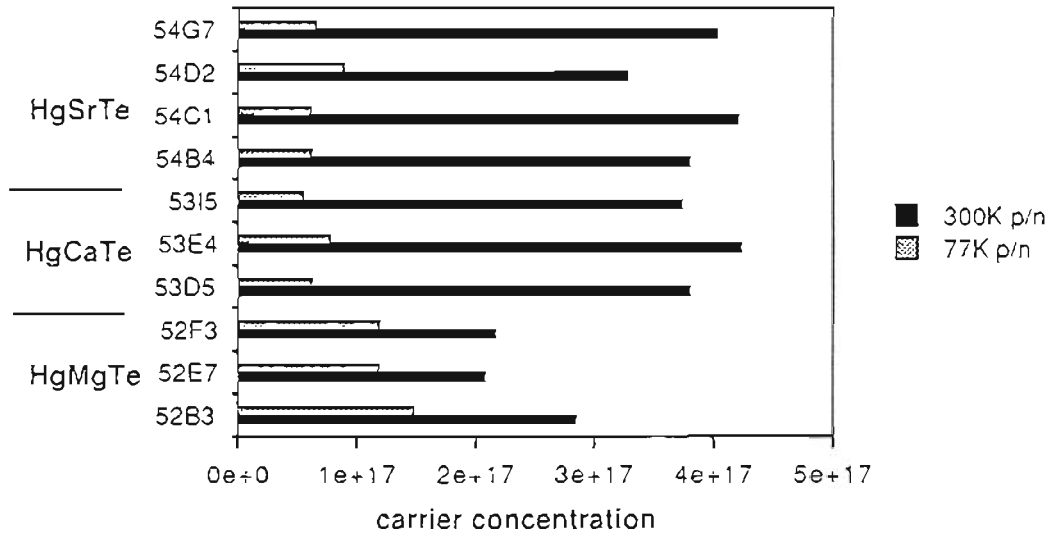

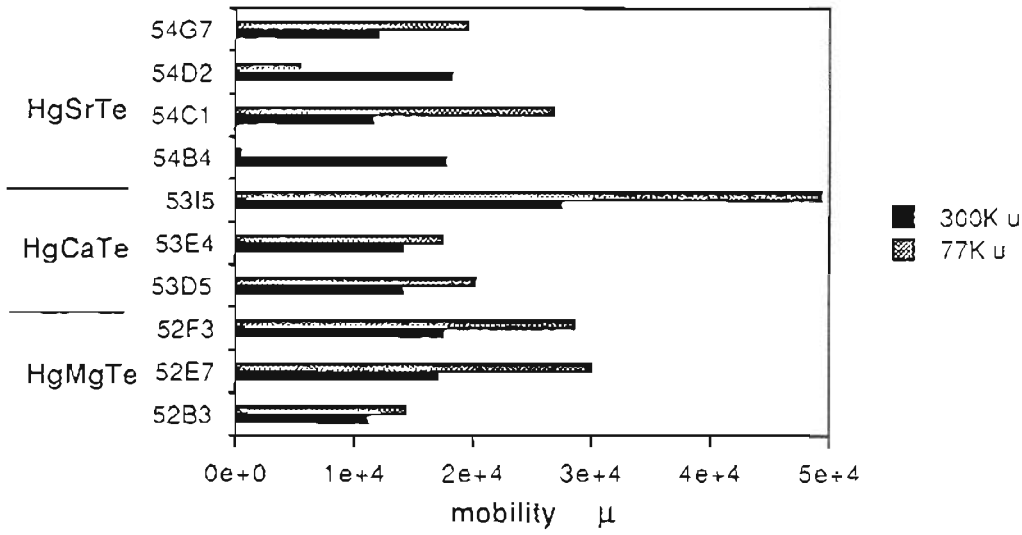

Figure 4-19 Hall data taken at room temperature (300k) and 77k for several alternative materials. Samples have all been annealed in a mercury overpressure for 14 days at 300C to reduce the concentration of mercury vacancies.

materials are similar to those in HgMnTe and HgCdTe grown at OGC. HgCdTe and HgMnTe material that has been annealed in mercury typically has electron concentrations of $4-6\ x10^{16} cm^{-3}$ and electron mobilities of $8-9\ x10^{4} \frac{cm^2}{Vs}$ when measured at 77K. The data in figure 4-19 shows lower mobilities and higher concentrations. Only one sample of HgCaTe shows a low temperature mobility approaching 50,000. Values such as these should not be considered disheartening. The bulk growth of these alternative materials is still being developed and with additional work the electrical properties should improve.

4.5 Ion Implants

The suitability of ion implantation techniques for use with HgCdTe has been investigated.[75-78] However, there has been little work done with alternative materials. Our investigation was specifically aimed at studying the electrical properties of HgMnTe, after implantation and a laser annealing process.

A series of HgMnTe samples was prepared by the standard means and then characterized with Hall techniques. The results of these characterizations are given in table 4-5. The samples were then sent to The Aerospace Corporation for implantation. The implanted species was $^{10}B^{+}$ and the dose schedule and beam currents are detailed in table 4-6. The samples were mounted to a three inch silicon wafer using Dow-Corning vacuum grease. The wafer was then attached to the liquid nitrogen stage and cooled

TABLE 4-5
Before Ion-Implant Hall Data for HgMnTe (77K)

Sample	X (%)	bulk p/n (cm^{-3})	bulk μ (cm^2/Vs)
38-1G	9.8	$n = 6 \times 10^{16}$	900
36-2G	6.5	$n = 3 \times 10^{16}$	2,000
43-3F	9.5	$n = 3 \times 10^{16}$	4,600
43-1F	9.5	$n = 3 \times 10^{16}$	3,500
43-5I	12.2	$p = 2 \times 10^{17}$	100
44-2H	7.6	$n = 6 \times 10^{16}$	1,500
44-5F	10.9	$p = 9 \times 10^{16}$	600
44-4E	12.2	$n = 7 \times 10^{16}$	300
44-1J	10.2	$n = 4 \times 10^{16}$	1,700
44-3E	12.2	$p = 6 \times 10^{16}$	500

TABLE 4-6
Ion-Implantation Schedule for HgMnTe

Ion Energy (KeV)	Ion Dose (10^{14} cm^{-2})	Beam Current ($\mu A/cm^2$)
100	5	0.037
200	5	0.044
300	5	0.044
400	5	0.036

throughout the implanting process. The samples were observed to have remained fixed in their original positions and were not heated above ambient after the implantation. Samples were warmed to ambient, removed from the silicon wafer and cleaned with TCE and methanol rinses.

Several of the samples were subjected to neutron depth profiling (NDP) at the National Bureau of Standards' facility in Gaithersburg, Maryland. Results from this profiling indicated that the implants were distributed in good agreement with well known Monte Carlo simulations[79] and that the dopant was confined to a surface layer of approximately one micron in thickness. Results from this NDP work are given in figure 4-20. The remaining samples were characterized using Hall techniques and a two layer analysis that assumes a surface layer of given thickness[74] and an underlying bulk region. As can be seen from table 4-7, implantation invariably creates a n-type surface layer regardless of the bulk properties prior to the implant. This layer is caused by physical damage from the implant.[80] The bulk electrical properties of the samples remain unchanged by the implant.

Note that the simple one-carrier Hall model used for as-grown material is reasonably accurate for strongly p-type or n-type material. However, in many samples the as-grown condition is one of mixed conductivity type. This is evidenced by the Seebeck results mentioned earlier. The implantation added an extra complication. As discussed above, the implant created a layer at the surface which was strongly n-type, but the bulk is still of mixed conductivity.

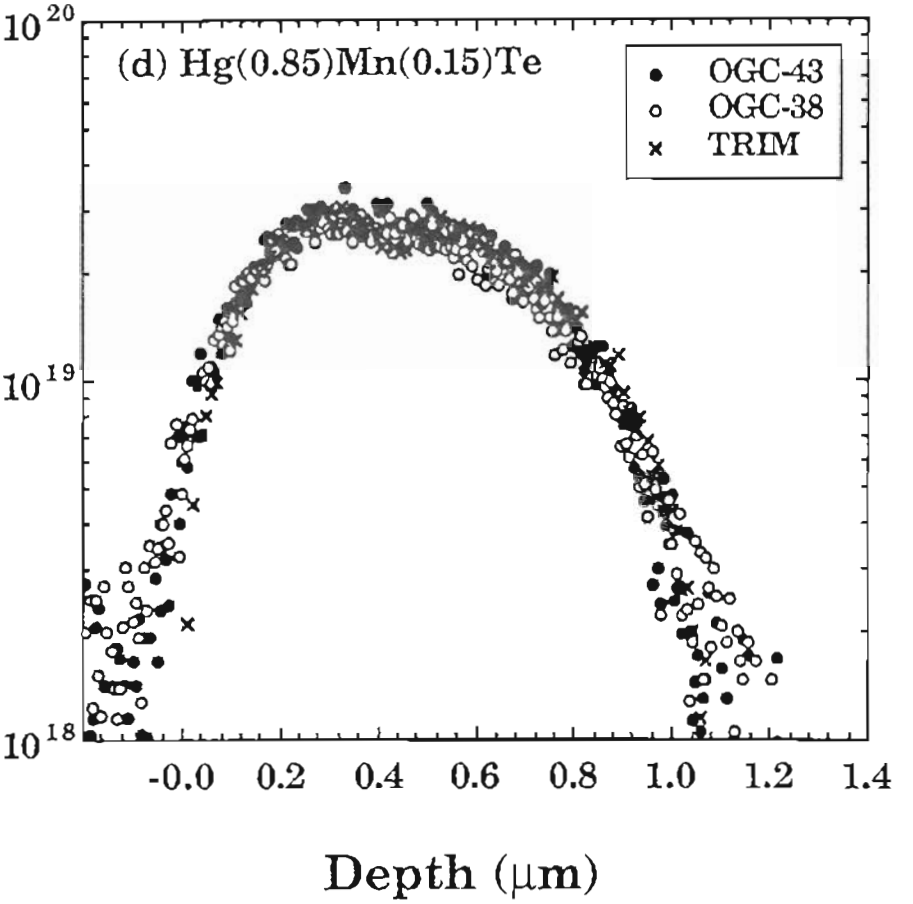

Figure 4-20 Neutron Depth Profiling (NDP) data showing $^{10}B^{+}$ concentration versus depth in implanted HgMnTe. Superimposed on the data are predictions from a Monte Carlo simulation (TRIM-86).

TABLE 4-7
After Ion-Implantation Hall Data For HgMnTe
Surface Layer Model (77K)

Sample	layer (μm)	p/n (cm^{-3})	μ (cm^2/Vs)	p/n (m^{-3})	μ (cm^2/Vs)
43-3F	1.0	n = 1.5e18	12,300	n = 3e16	4,600
43-1F	1.0	n = 4e18	9,000	n = 3e16	3,500
43-5I	1.0	n = 2e18	3,000	p = 2e17	100
44-2H	0.5	n = 9e18	4,000	n = 6e16	1,500
44-5F	1.0	n = 1e18	4,400	p = 9e16	600
44-4E	1.0	n = 1e18	3,500	n = 7e16	300
44-1J	1.0	n = 3e18	6,400	n = 4e16	1,700
44-3E	1.0	n = 6e17	5,000	p = 6e16	500

4.6 Laser Annealing

Several of the samples were then mounted to a liquid nitrogen cold finger and exposed to a CO_2 laser for various lengths of time. These samples were then characterized by the aforementioned Hall technique. The goal of the laser annealing was to "heal" some of the implant damage, thereby improving the electrical properties, especially the mobility and to activate the dopant.

The surface analysis is not particularly useful for material that has been laser annealed. This model assumes a thin surface layer over a much thicker bulk. This structure is connected in parallel (in the sense of electrical circuits) and thus assuming a layer thickness the characteristics of the surface layer can be predicted. The laser spot is less than half the width of the sample and thus the laser annealing process disturbs the uniformity of the surface. After annealing the surface layer would have to be modeled as as having multiple conduction paths each with different electrical characteristics. The physical dimensions of these paths are unknown, though a guess at their sizes could potentially be made based on Seebeck Mapping results presented earlier in this chapter. Given the uncertainty associated with such a model, it was decided to focus on an interpretation of results from the simple, single carrier Hall model. A summary of these results is presented in table 4-8.

After the laser annealing process, Hall measurements on only five of the original ten samples were possible. The remaining samples were either used as references for NDP work or broken while attempting to make Hall meas-

TABLE 4-8
Hall Data After Laser Annealing
Single Carrier Model (77k)

Sample Exposure Energy	43-3F 4 x 10s, 3w 120 Joules	43-1F 4 x 5s, 7w 140 Joules	44-2H 20s, 7w 140 Joules	44-5F 20s, 7w 140 Joules	44-1J 10s, 7w 70 Joules
as-grown p/n (cm^{-3})	n = 3e16	n = 3e16	n = 6e16	p = 9e16	n = 4e16
as-grown μ (cm^2/Vs)	4,600	3,500	1,500	600	1,700
post I-I p/n (cm^{-3})	n = 3e16	n = 3e16	n = 6e16	n = 2e18	n = 3e16
post I-I μ (cm^2/Vs)	5,600	5,000	2,000	40	2,700
post anneal p/n (cm^{-3})	n = 3e16	n = 3e16	n = 5e16	n = 1e18	n = 4e16
post anneal μ (cm^2/Vs)	3,000	8,000	3,100	50	1,600

urements. For the majority of the samples, laser annealing did not alter the electrical properties greatly. Usually, both electron concentrations and mobilities remained unchanged. In certain cases, however, while the concentration remained relatively constant the mobility showed a significant increase upon laser annealing. It is suspected that this increase in overall mobility was due solely to an improvement in the surface layer mobility. The properties of the bulk material should remain unchanged.

Any improvement in the sample's electrical properties depended strongly on the details of the annealing procedure. Time and power could be varied and it was possible to anneal the samples with a continuous burst or a series of shorter pulses separated by a period during which the sample could cool. Extremely lengthy anneals could produce the sort of lateral diffusion of mercury that has already been discussed.

With the CO_2 laser set to seven watts of power the optimum exposure seems to be about 20 seconds for the HgMnTe used in this investigation. Two samples in particular showed substantial improvement in their n-type mobility. Interestingly, one of these samples (43-1F) was annealed in four bursts of five seconds at seven watts, another (44-2H) was annealed with a continuous burst of twenty seconds also at seven watts. The total energy transferred would then be 140 Joules. Two other samples were annealed with substantially less energy, one with several bursts (43-3F) the other (44-1J) with a continuous exposure. Both of these samples showed a decrease in mobility. The remaining sample (44-5F) seems to yield unexpected results. However, considering its as-grown condition to be rather strongly p-type,

while the others were equally strongly n-type this may not be a fair comparison.

This information seems to indicate a threshold in absorbed energy is important rather than time or power threshold independently. The annealing process is most properly thought of as allowing the atoms in the lattice to rearrange themselves to positions more favorable for electronic transport. Energies of less than the threshold apparently do not permit this realignment.

Implantation techniques seem compatible with HgMnTe materials. The generation of an n-type layer, with reasonable electrical properties, in as-grown bulk material is a first for this material. The use of laser annealing techniques were successful, but the application of this process needs to be managed carefully in light of the possibility of mercury loss and lateral diffusion.

Still, the question of successfully implanting and activating p-type implants in HgTe materials remains. Some investigators have reported some success in activating p-type implants in HgCdTe with laser annealing techniques,[81,82] while other investigators use more standard thermal annealing processes[75] and some novel thermal pulse[83] annealing techniques. The ability to activate implants needs to be demonstrated in HgMnTe, if it is to prove a viable alternative to HgCdTe.

CHAPTER 5
MODELING OF TEMPERATURE DISTRIBUTIONS

As often is the case, the full complexity of physical processes underlying portions of an investigation prove to be unmanageable. Specifically, a comprehensive treatment of either the Seebeck effect, or laser-induced heating would have led to analysis outside the realms of an experimental dissertation. To provide some understanding of the mechanisms at work, a modicum of modeling work was attempted. An understanding of the laser-induced heating of irradiated samples seemed a logical starting point. Strictly speaking, this problem is three dimensional. However, for the purposes of this analysis the laser heating will be modeled in two dimensions, and it will assume a circular, Gaussian laser spot, and compositionally uniform material.

The starting point for the laser heating analysis is a 1977 paper by M. Lax.[84] His work allows one to estimate the temperature profiles of a material whose surface is being exposed to a laser. The solution to the general problem involves making several assumptions regarding the thermal properties of the material under investigation. Since these properties are best known for HgCdTe, the analysis will be limited to a discussion of the heating of HgCdTe materials, with an extrapolation for the behavior of other materials.

The interest in obtaining an understanding of temperature profiles during laser heating is of interest because of the drastic alteration in surface and

near-surface electrical properties, measured by Seebeck mapping, seemingly caused by exposure to a laser. It is postulated that the lateral temperature gradients present in the sample during exposure allows mercury diffusion to take place. This being the case, then an understanding of what the temperatures and gradients are should prove enlightening.

The analysis begins by assuming the beam to have Gaussian intensity distribution given by:

$$I = I_0 \, e^{-\frac{r^2}{w^2}}, \tag{5.1}$$

where r is the radial distance from the center of the beam spot, and w is a beam parameter known as the waist. At this point, the beam spot is considered to be a slowly varying function of z, the depth below the sample surface, so that w may be treated as constant.

The Sylvania #948 CO_2 laser has a $\frac{1}{e^2}$ beam waist of three millimeters near its aperture. This corresponds to a value of $w = \frac{3}{\sqrt{2}}$ mm. The beam has an optical pathlength l, of 0.75m before falling on the sample stage. The standard[85] relationship used to calculate beam width at a distance from a known waist is given by:

$$w(l) = w\left[1 + \left(\frac{\lambda l}{\pi w^2}\right)^2\right]^{\frac{1}{2}}. \tag{5.2}$$

With a wavelength of 10.6μm and using the aforementioned parameters this relationship yields, in millimeters:

$$w(l) = \frac{3.0}{\sqrt{2}} \left[1 + 2.25\text{x}10^{-6}l^2\right]^{\frac{1}{2}}. \qquad 5.3$$

To calculate the rate of change with respect to the beam depth within the sample the derivative of 5.3 is taken:

$$\frac{d}{dl}w(l) = \frac{3.0}{\sqrt{2}}\ 2.25\text{x}10^{-6}\ l\ \left[1 + 2.25\text{x}10^{-6}l^2\right]^{-\frac{1}{2}}. \qquad 5.4$$

This quantity, evaluated with $l = 750$mm is dimensionless, giving the change in beam width per distance within the sample in units of millimeter per millimeter.

$$\frac{d}{dl}w(l{=}750) = 5.39\text{x}10^{-3} \qquad 5.5$$

This value may safely be considered as slowly varying, since our interest will only extend to a depth, z, on the order of 100μm. The assumption then, is that: $w(l{=}750) \approx w(l{=}750.1)$.

With α being the attenuation constant of the beam in the solid:

$$G(r,z) = \alpha e^{-\alpha z} I_0 f(\frac{r}{w}), \qquad 5.6$$

gives the energy absorbed in a unit volume per second and the function $f(\frac{r}{w})$ is for the Gaussian case given by:

$$f(\frac{r}{w}) = \exp^{-\frac{r^2}{w^2}} \qquad 5.7$$

Finally, Lax writes the temperature rise as:

$$\Delta T = T_{max} N(R,Z,W), \qquad 5.8$$

where T_{max} is given by:

$$T_{max} = \frac{P}{2\pi K}\frac{\pi^{1/2}}{w}, \qquad 5.9$$

where P is the total beam power, K is the thermal conductivity of the material and N(R,Z,W) is a normalized temperature rise taking on values $0 \leq N \leq 1$.

The real variables r (distance from beam center), z (depth below surface), and α (attenuation in cm^{-1}), have been scaled with the spot size, w, to yield:

$$R = \frac{r}{w}, \quad Z = \frac{z}{w}, \quad W = \alpha w\ . \qquad 5.10$$

The solution obtained by Lax is given as:

$$N(R,Z,W) = \frac{W}{\int_0^\infty F(\gamma)d\gamma}\int_0^\infty J_0(\gamma R)F(\gamma)\frac{We^{-\gamma Z} - \gamma e^{-WZ}}{W^2 - \gamma^2}d\gamma, \qquad 5.11$$

where J_0 is the zeroth order Bessel function and γ is a dummy variable of integration. The function $F(\gamma)$ is the Bessel transform of $f(\frac{r}{w})$ and is known exactly for the Gaussian case. With $R = \frac{r}{w}$:

$$F(\gamma) = \int_0^\infty f(R)J_0(\gamma R)RdR = \tfrac{1}{2}e^{-\frac{\gamma^2}{4}}. \qquad 5.12$$

The limiting form of this solution when $W \sim \infty$, is:

$$N(R,Z,\infty) = \frac{1}{\pi^{1/2}}\int_0^\infty J_0(\gamma R)\exp(-\gamma Z)\exp(-\frac{\gamma^2}{4})d\gamma. \qquad 5.13$$

A further simplification can be made by restricting interest to the case of R = 0. If this is done then an explicit solution can be obtained[86] as:

$$N(0,Z,\infty) = \exp(Z^2)\left[1 - \mathrm{erf}(Z)\right], \tag{5.14}$$

where the error function is given[87] by:

$$\mathrm{erf}(Z) = \frac{2}{\pi^{1/2}}\int_0^Z \exp(-t^2)dt. \tag{5.15}$$

The solution with very large W is the situation of complete absorption occurring essentially at the surface of the solid. In this case, it will be shown that the maximum temperature rise also occurs at the surface. The optical quality of the material at the surface is measured by the reflectivity experiment and EDX work described in chapter four. The temperature distributions of the surface regions are thus of prime concern in this analysis.

Before proceeding it is necessary to calculate T_{max}. Except for the solid's thermal conductivity K, which is a function of temperature, this calculation is straightforward. Data is available for the thermal conductivity of HgCdTe at various temperatures and with different compositions.[32] In the temperature range 100-500 K the relationship:

$$K(T) = \frac{0.51}{T^{0.64}}\ \frac{\mathrm{watt-K}}{\mathrm{cm}}, \tag{5.16}$$

is used to determine the thermal conductivity of x=0.2 HgCdTe. This function can be averaged by calculating:

$$K_{ave} = \frac{\int_{T_{min}}^{T_{max}} K(T)dT}{(T_{max} - T_{min})}. \tag{5.17}$$

Performing this integration we have:

$$K_{ave} = \left[\frac{0.51}{400} \frac{T^{0.36}}{0.36} \right]_{100}^{500} = 0.042 \frac{watt-K}{cm}. \qquad 5.18$$

Calculating T_{max} we obtain:

$$T_{max} = \frac{5.0}{0.084\pi} \frac{\pi^{\frac{1}{2}}}{0.3} = 158K. \qquad 5.19$$

The numerical value of this prefactor is of less interest in this investigation than the behavior of the normalized temperature distribution N(R,Z,W) as a function of R and Z. Early, preliminary calculations using other values for thermal conductivity have estimated maximum temperature rises larger than this value by almost a factor of two.[71] Even these, substantially larger values, when added to the initial temperature of the sample (attached to a LN_2 cold finger) give final temperatures much lower than the temperatures normally assumed necessary[7,53] to produce mercury diffusion.

Further analysis of the N(R,Z,W) function will be limited to the case of very large W, which corresponds to very strong attenuation of the incident radiation. This assumption is valid for p-type HgTe materials[55] and can be considered to be the limiting case for other materials. The effect of decreasing α (i.e. decreasing W) is to distribute the incident power to greater depths and to decrease the temperature rise near the surface of the solid. Thus, materials in which the incident radiation is attenuated less strongly will be able to undergo longer exposures without experiencing mercury loss or diffusion.

Figure 5-1 gives the normalized temperature rise at the center of the beam spot as a function of depth within the solid. With a beam spot of approximately $\frac{3}{\sqrt{2}}$ millimeters, a depth of 100μm would correspond to $Z = \frac{0.1\sqrt{2}}{3} \approx 0.05$. Obviously there is little change between temperatures at the surface and temperatures at a depth of 100μm.

If M_x is the ratio of the normalized temperature at a depth of x microns to the temperature at the surface then:

$$M_{10} = \frac{N(0,10\ \mu m,\infty)}{N(0,0,\infty)} = 0.99\ , \quad \text{and} \quad M_{100} = \frac{N(0,100\ \mu m,\infty)}{N(0,0,\infty)} = 0.95\ .$$

Figure 5-2 shows the behavior of the normalized temperature at and near the surface, as a function of distance from the center of the laser spot. The three curves detail this temperature rise at different depths, Z. The surface corresponds to the topmost curve, the middle curve represents the temperature distribution at a normalized depth of $Z = 0.05$ ($\approx$ 100μm), and the bottom curve a depth of $Z = 0.1$ ($\approx$ 200μm). Notice that the maximum difference between these curves occurs at $R = 0$, or beam center.

Also included in figure 5-2 is an indication of the regions of the sample mapped in figure 4-18. The central p-type annular region extends to approximately $R = 0.6$. The surrounding n-type region then continues to approximately $R = 1.1$. Thus the normalized temperature in these regions corresponds to $1 \geq N \geq 0.79$ for the central region and $0.79 \geq N \geq 0.53$ for the surrounding region.

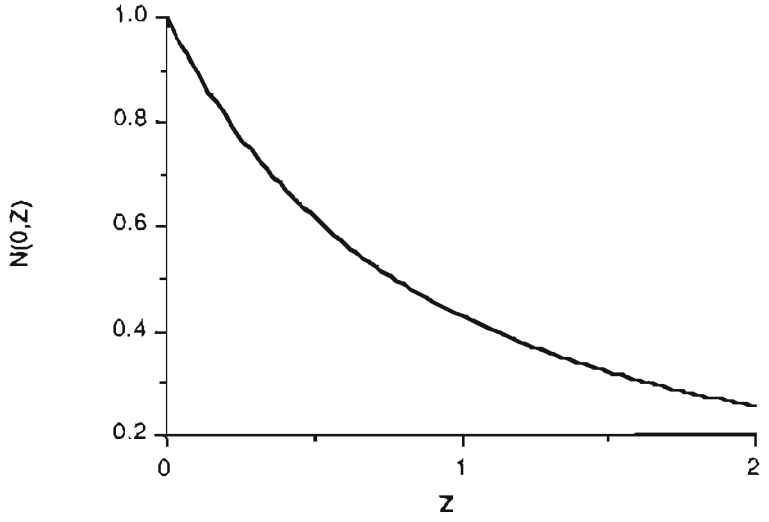

Figure 5-1 Using Lax's model the normalized temperature rise takes on values between zero and one as a function of distance below the surface of the solid. The depth Z is a normalized distance, $Z=z/w$, where w is the spot radius at the sample surface. For the experimental setup used, a depth of 100 microns corresponds to $Z\approx 0.05$.

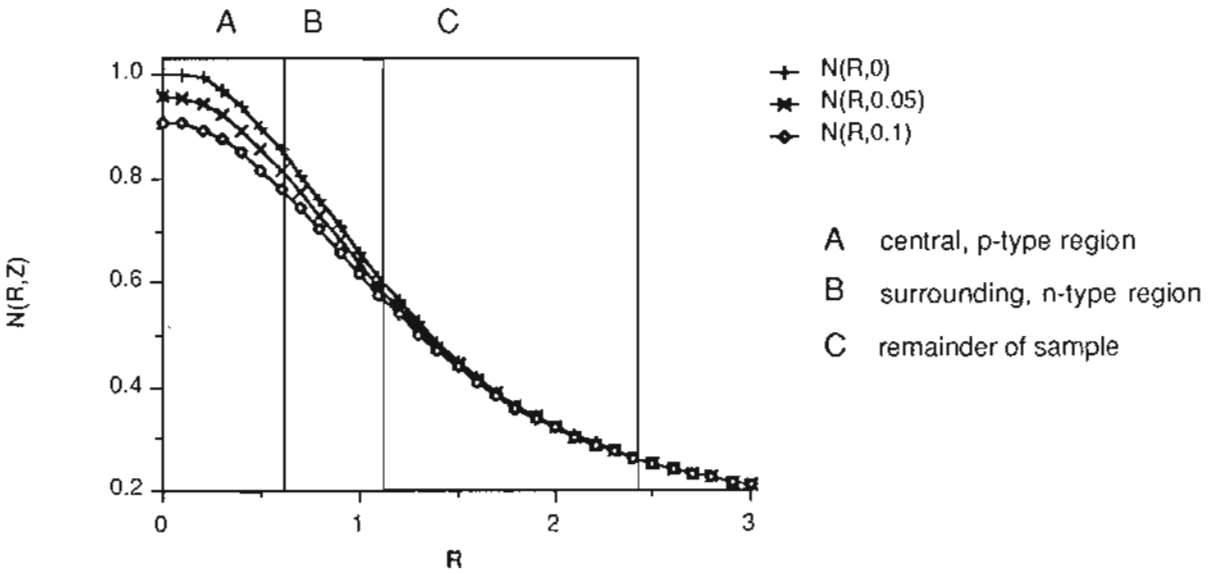

Figure 5-2 Analysis of Lax's model can also be used to generate temperature information versus distance from the spot center. The three curves represent such information at different depths below the surface. The topmost curve is at the surface, the middle curve at Z=0.05, and the bottom curve at Z=0.1. The latter two curves correspond to depths of 100 and 200 μm respectively. The dimensions A, B and C are taken from figure 4-18. A≈0.6 corresponds to the radius of the central p-type region. B≈0.5 corresponds to the width of the surrounding n-type annular region, and C≈1.3 to the remaining radius of the sample.

The above analysis is important since it corroborates the interpretation of Seebeck maps given in chapter four. In particular, several of the many maps taken after the sample was exposed to a laser were presented and the structure seen in these maps was seen to extend a finite distance beneath the original surface of the material. This assertion has been confirmed by repeated cycles of mapping/material-removal to a depth of approximately 100 microns beneath the original sample surface. To this depth in the samples, the corresponding maps have very similar features.

That the sequential maps are similar is not surprising in light of the above analysis that shows the temperature profiles in these regions during laser exposure to be similar. Thus, regions of the sample subjected to similar temperatures and temperature gradients experience similar degrees of mercury diffusion. This implies that the redistribution phenomenon is one inherent to the material and not an artifact of material defects or surface preparation. While the modeling does explain the depth behavior of the lateral mercury diffusion, it does not predict a high enough temperature for any diffusion at all during the time involved.

This approach to determining a laser induced temperature rise in a material offers the advantage of providing an analytical solution. A number of iterative, numerical schemes have been developed as well. These treatments are applicable to scanned or stationary laser beams[88] and e-beams.[89,90]

An iterative technique more easily incorporates the variation with tem-

perature of material parameters such as thermal conductivity. An extension of Lax's analysis to include these concerns is available,[91] but the additional complexity rivals that of iterative solutions.

Several analysises are available for layered structures. One is a reasonably analytical approach, which arrives at a Green's function solution.[92] The other is an iterative approach.[93] The most general versions of these treatments assume each layer to have different thermal conductivity and diffusivity. The geometry of such an analysis would seem to be ideal for application to laser induced heating of epitaxial HgATe materials, but has not been pursued here.

CHAPTER 6
CONCLUSIONS

The information presented in this dissertation is, in many ways, a feasibility study. Of the materials that have been investigated as possible alternatives to HgCdTe only HgMnTe and HgMgTe have received anything beyond cursory attention. For the remaining materials, and indeed for these two, this evaluation should serve only as a very preliminary comparison between their strengths and weaknesses.

6.1 Bandgap versus Composition

Figure 6-1 gives a bar graph of the $\frac{dE_g}{dx}$ relationship for various HgATe materials. For HgCdTe and HgMnTe this value is fairly well know, and for HgMgTe work in chapter three provides the information. For the rest of the materials the quantity is interpolated by assuming a linear relationship between the bandgaps of the two binaries. This relationship is important for very practical reasons.

Good bulk HgCdTe material can today be produced with a uniformity on the order of $\Delta x \approx \pm 0.01$.[9] This difference would result in a variation of the nominal bandgap of the material by:

$$d\frac{E_g}{dx}\Delta x = \Delta E_g \approx 0.02\text{eV}. \qquad 6.1$$

A similar deviation in the composition of HgMgTe would change the

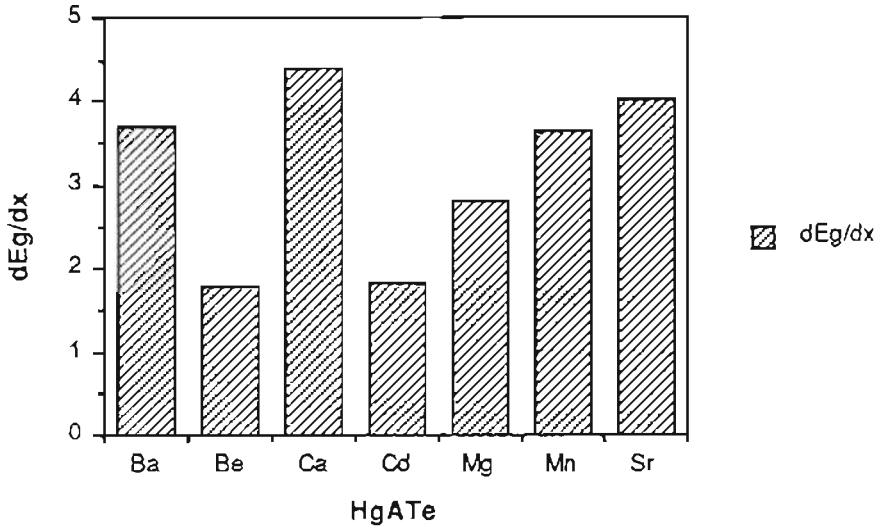

Figure 6-1 This rate-of-change relationship is calculated assuming a linear variation between the bandgaps of the constituent binaries. In reality there may be some bowing to the relationship.

bandgap by $\Delta E_g \approx 0.04eV$. Thus, the larger the value of $\frac{dE_g}{dx}$ the greater the effect that nonuniformities in material composition have on bandgap variations.

If it were possible to control material composition very accurately, and if the binaries were completely miscible, then the ability to produce material with $E_g = 0$ to $E_g \approx 4eV$ as in CaTe, could be useful. However, there are other materials suitable for mid to large bandgap applications including silicon, GaAs, ZnS and ZnSe. Further, after this preliminary investigation it would seem that developing wide gap HgTe based ternaries including HgCaTe and HgSrTe materials will be difficult.

Our growths of HgCaTe, HgSrTe, and HgBaTe did not produce uniform ingots. Plots of measured density for these wide-gap materials given in chapter three indicate that only a fraction of the intended amount of calcium, strontium or barium was introduced into the HgTe lattice. Since FTIR measurements on these materials failed it is possible that not enough of the substitutional element was introduced to produce a positive bandgap in the ternary. Perhaps these materials have extremely large or small segregation coefficients in HgTe, and are not suited to equilibrium bulk growth. Without further data on the bandgap versus composition relationship in HgCaTe, HgSrTe and HgBaTe it is impossible to predict the usefulness of these compounds as infrared device material.

Of the HgATe materials (A = Cd, Mn, Mg) that have been more extensively studied, HgMnTe has the largest value of $\frac{dE_g}{dT}$. Unfortunately, single

phase samples of this material can only been produced in compositions up to a value of $x = 0.35$.[19] The problem is that, as a binary MnTe is of a different crystal structure than HgTe. Beyond $x = 0.35$ growths tend to be of mixed structures.

A similar problem is encountered in HgMgTe where equilibrium growth can only produce material to a composition of $x = 0.2$.[27] Like manganese compounds, the bandgap of HgMgTe also changes with composition more rapidly than in HgCdTe. Using the data in table 1-2, the largest producible bandgaps in HgMgTe and HgMnTe are, respectively ≈ 0.32 eV and ≈ 0.97 eV. Thus, gaps which are of technological interest are easily obtainable in both of these materials.

If these ranges of bandgap are insufficient, it may prove possible to produce both materials, with larger compositions of manganese or magnesium by utilizing nonequilibrium epitaxial growth techniques such as MBE or MOCVD. Still, it would appear that the HgTe-ATe systems will find most of their applications in the narrow-gap regime.

6.2 Lattice Parameter

An important factor in determining the usefulness of a material relates to its lattice parameter, which is a function of composition in ternaries. Especially for epitaxial techniques, there are concerns surrounding lattice mismatch with whatever substrate material is to be used.

Figure 6-2 is a plot of lattice parameter versus composition for several of

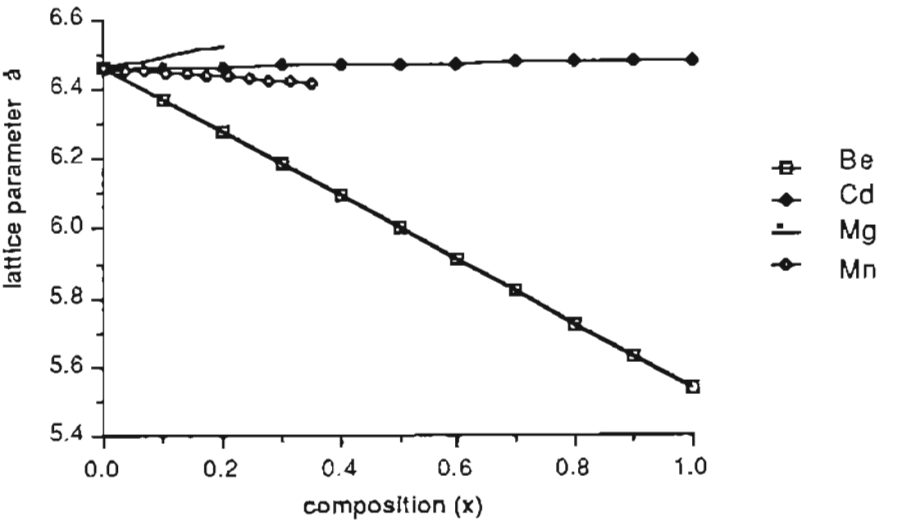

Figure 6-2 Variation in lattice parameter with x for three materials (HgCdTe, HgMnTe, HgMgTe) known to form in the zincblende structure for some or all compositions. Also included is the extrapolated relationship for HgBeTe.

the materials mentioned in this investigation. Since Vegard's law has been assumed, within certain ranges these relationships are linear. Further note that for two of the materials there is a known composition limit.

A topic of concern is the lattice match of HgTe materials to other materials normally used as substrates during epitaxial work. The most common substrate for growth of HgCdTe is CdTe, primarily because it is possible to obtain fairly large CdTe substrates. Recently, good quality substrates from the CdZnTe and CdMnTe families have become available. The $a_o(x)$ relationship of $Cd_{1-x}Zn_xTe$ for example, may then be used to tailor the lattice parameter of the substrate to that of the epilayer.

Figure 6-3 gives a scatter plot of E_g versus lattice parameter for a number of binary compounds. This data is taken from table 1-2. By connecting any two of these points in a linear fashion one can obtain an $E_g(a_o)$ relationship for the psuedo-binary made up of the two binaries that have been joined. The solid lines show possible substrates, while the dotted lines are the HgATe alloys.

By focusing on a horizontal line at a particular E_g of interest, the intersection of this line and the dotted lines connecting HgTe to other compounds corresponds to the desired bandgap being reachable (at some composition) in that psuedo-binary system. If vertical lines are placed at each of these compositions then the intersection between these imagined vertical lines and the solid lines joining the substrate materials indicate the compositions needed in various compounds to produce materials of common lattice parameter. This

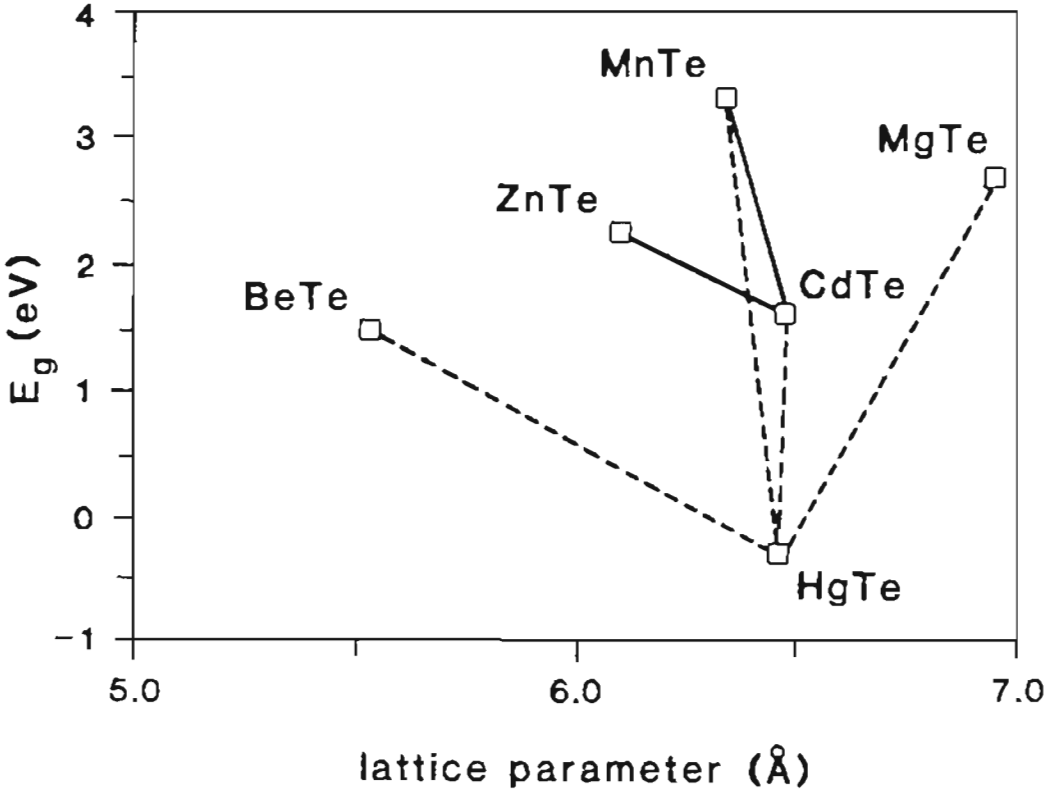

Figure 6-3 On this sort of plot each binary is represented by a single point. By connecting the points one obtains a linear relationship between bandgap and lattice parameter in the associated psuedobinary. With appropriate interpretation this diagram can be used to predict lattice matched psuedobinary pairs. One of the pair may then be used as a substrate for epitaxial growth of the other.

technique can be used to predict a suitable, lattice matched substrate for a particular composition of HgATe. For example, HgMnTe with a nominal bandgap of 0.2 eV could be lattice matched to CdZnTe with $x \approx 0.15$ or CdMnTe with $x \approx 0.30$.

Using this analysis it is possible to see that HgMnTe can always be lattice matched to a composition of CdZnTe. However, since the lattice parameter of HgMgTe increases with increasing magnesium content HgMgTe could only be matched for low concentrations of magnesium. Further, it would appear that HgBeTe could be lattice matched to CdZnTe over a substantial range of compositions.

6.3 Stability Under Heating

Another major concern, already mentioned, is that the elevated temperatures necessary during material processing and device fabrication will cause physical damage and/or mercury loss from the material. The reflectivity experiments described in chapter four and appendix G, can be interpreted to give a measure of this stability.

The CO_2 laser causes rapid and localized heating which eventually results in surface damage and mercury loss. Loss of mercury indicates that mercury-tellurium bonds are being broken in substantial numbers. The energy required to break these bonds can therefore be thought of as an indication of the strength of that bond, and a direct measure of the stability of the material under heating.

Separate experiments with samples mounted on a cold finger, show virtually zero mercury loss during exposure times approaching one minute. If significant mercury were lost as a result of direct photon interaction, this loss could be detected at shorter exposure times and would become greater with increasing exposure. The presence of a threshold exposure time below which little mercury is lost from uncooled samples indicates that the majority of the laser power contributes to bulk heating.

With p-type samples, the extinction length is small and the heating primarily takes place at the surface of the material. With n-type samples, which have a larger extinction length, a greater proportion of the incident photons should penetrate a finite distance into the material before being absorbed. In this latter case, as analysis in chapter five indicates, the temperature rise near the surface is lessened.

The information that comes out of these reflectivity measurements is the characteristic time t_d after which the material surface quality degrades. This measure t_d can be used as a comparison of material stability during exposure to a CO_2 laser. For samples that have not been annealed in mercury vapor, and hence are still p-type, t_d can be used as a more general measure of material stability during surface heating. Since, in p-type material the heating occurs in a small region adjacent to the surface on which the laser is incident, this situation should be similar to other forms of heating be they in a rapid thermal annealing system or during a wire bonding process.

Several authors have studied the interaction between a laser and

CdTe.[47-49] These studies indicate that material damage occurs and that material can be sublimated at temperatures far below the melting point of CdTe. Similar results can be deduced for laser exposures made on HgMnTe. The greatest temperature rises predicted in chapter five are far below the melting point of HgMnTe yet are lengthy enough to cause surface damage.

Meaningful comparisons of t_d can best be made between different HgATe materials if the material composition is converted to a minimum bandgap energy using relationships presented in chapter three. For example, t_d for an x=0.1 HgMnTe sample would be compared to t_d for an x=0.2 HgCdTe sample. Such a conversion was not possible with HgCaTe and HgSrTe, since no x(ρ) relationship could be determined. t_d times for these materials are presented along with the measured densities of the samples. Comparisons between as-grown and mercury annealed samples can also be made.

Few compositions of as-grown material were available for reflectivity experiments. For HgCdTe, HgMnTe and HgMgTe there is little overlap in composition, as is evident from figure 4-5. The trend with HgCdTe and HgMnTe is to lower values of t_d with larger bandgap material. HgMgTe seems to have a minimum in t_d at approximately 120 meV which is close to the energy of the incident photons. The actual values of t_d for HgMgTe are substantially lower than those for the other two materials in the limited regions of overlap. No compositions of as-grown HgCdTe or HgMnTe were available with E_G near the incident photon energy.

There is some similarity in the behavior of mercury annealed HgCdTe and HgMnTe and as-grown material. In both cases HgCdTe shows a decline in t_d as material compositions approach a bandgap of 100 meV. Likewise in both cases HgMnTe shows a decline in t_d at compositions with a bandgap of just above 200 meV. The t_d values for HgMgTe show much less variation with composition in both as-grown and annealed material than either of its sister materials.

The mercury anneal produced HgMgTe material able to withstand substantially longer exposures to laser irradiation. Values of t_d between 1.25 and 1.75 seconds were measured in this material compared to as-grown material which could tolerate exposures of 0.5 seconds or less. Between 100 and 250 meV both HgMnTe and HgMgTe show values of t_d larger than those for HgCdTe.

Both HgCdTe and HgMnTe show a sharp maximum in t_d at particular compositions. In HgCdTe the maximum occurs at approximately 65 meV while in HgMnTe at 200 meV. It is interesting to note that in HgCdTe larger values of t_d occur in compositions whose minimum bandgap has a value lower than the incident photon energy. This material should strongly absorb the incident radiation by way of photoexcitation of carriers. Stronger absorption should lead to greater surface heating and smaller, not greater, values of t_d In fact substantially smaller values of t_d were measured in compositions of HgCdTe whose minimum bandgap energy is larger, almost by a factor of two, than the incident photon energy. This material should attenu-

ate the incident radiation less strongly, and experience less surface heating and have greater values of t_d. This behavior seems to suggest that there is some other mechanism at work. Such behavior would be expected if the addition of cadmium does indeed weaken the Hg-Te bonds in HgCdTe. Increasing the cadmium above x=0.2 in HgCdTe should produce material that is increasingly transparent to 10.6μm light. Instead the addition of cadmium weakens HgCdTe so that what absorption that does occur is sufficient to cause the loss of mercury.

Two novel materials HgCaTe and HgSrTe were investigated by reflectivity techniques as well. Comparisons between these materials and other better-known HgATe materials are best done carefully since $E_g(x)$ and $\rho(x)$ relationships are not known. Both as-grown and mercury annealed samples of HgCaTe and HgSrTe showed impressive values of t_d. These materials could withstand laser exposures two to three times greater than other materials before showing surface damage. Further, the spread in t_d data is comparatively small indicating that the surfaces of these samples were more uniform than were the surfaces of other materials.

Though density data indicates an amount of calcium and strontium was included in the respective growths, the actual quantity is quite small. A explanation of the large values of t_d could involve the minute amount of substitutional calcium or strontium not affecting the bond strength of HgTe significantly. Or, the explanation could be that small amounts of these two elements strengthen the HgATe material. There is inconclusive data to

predict which of these two is more likely. However, if we assume that bond weakening or strengthening is the primary factor influencing t_d then (as shown in tables 4-1 through 4-4) we can rate the materials in order from strongest Hg-Te bond to weakest, for HgATe materials with $E_g \approx \frac{hc}{10.6\mu m}$. This rating is given in table 6-1.

For HgMnTe and HgMgTe having small spreads in t_d values (i.e. small σ) the averaged exposure times are practically identical. There is one collection of data for HgMnTe with $x \approx 0.10$ with significantly greater t_d but the spread in this particular data makes a definitive conclusion impossible. Clearly though, HgCdTe is substantially (almost 30%) "weaker" in terms of its ability to withstand laser irradiation before damage occurs.

The conclusion then, is that HgMnTe and HgMgTe are better choices, other considerations nonwithstanding, than HgCdTe when device fabrication will involve processing with a cw CO_2 laser. Further, this rating can be thought to give a more general rating of Hg-Te bond strength. In this case HgMnTe and HgMgTe are better candidates for any application involving fabrication techniques which supply enough energy to the material to allow Hg-Te bonds to be broken.

6.4 Electrical -- Hall and Seebeck Measurements

An important understanding, brought forth by the Seebeck mapping work described earlier is that a sample of as-grown material may have adjacent regions of different conductivity types. Figure 4-16 in chapter four, with

TABLE 6-1
Stability Rating for Mercury Annealed HgATe Material

Material	x (%)	E_g (meV)	(t_d)	Std. Deviation σ
HgMnTe	10.0	214	2.70	1.3
HgMnTe	11.0	247	1.87	0.12
HgMgTe	12.0	220	1.89	0.12
HgCdTe	19.5	205.8	1.2	0.34

its associated interpretation, clearly shows this situation in HgMnTe.

The position of a sample in the ingot apparently has a bearing on conductivity type. Bartlett[10] et al relate sample position only to composition. Seebeck results presented in chapter four clearly relate conductivity type to position in bulk HgMnTe.

These considerations are important in the interpretation of Hall data taken from as-grown samples. It may well be the case that data interpreted using a single carrier model is unreliable because of mixed conductivity in the sample.[59] In some cases, for example in the samples mapped in figure 4-16, the arrangement of n-type and p-type regions could perhaps be deduced from van der Pauw data because of the strong dependence these measurements would have on the position of contacts. In this case the van der Pauw F factor[94] would be extremely sensitive to the positioning of the contacts. However, for the type 4 sample mapped in figure 4-14, there is a great deal of symmetry which could result in values of the F factor which are very close to unity.

In an aside it is interesting to note that some recent work[95] has proposed a model to explain anomalous Hall data for HgCdTe. The model assumes the existence of p-type HgCdTe inclusions in an n-type HgCdTe matrix. The Seebeck mapping techniques presented in this investigation give independent corroboration of the presence of adjoining p-type and n-type regions.

As one moves toward the last-to-freeze end of the ingot described above,

a more uniform conductivity prevails. Unfortunately, much of the growth would be wasted if only a portion of an ingot's material could be used. A more reasonable approach might be to subject questionable material, that is material from portions of an ingot known to have mixed conductivity, to an anneal in dynamic vacuum at elevated temperatures, followed by an anneal in mercury overpressure. Maps of samples put through this procedure are given in figure 4-17. The vacuum anneal depletes the surface regions of mercury causing uniform p-type behavior. The subsequent mercury overpressure anneal reintroduces mercury uniformly to the surface. This latter anneal can be stopped after an appropriate length of time to retain p-type conductivity, as was done on the sample mapped in figure 4-17C, or be allowed to continue to produce n-type behavior in surface regions and a buried p-n junction.

Some Hall data was taken on mercury annealed samples of HgCaTe and HgSrTe. The information is presented in chapter four, but can be summarized as inconclusive. The measured mobility and carrier concentrations are typical of HgATe materials. The strongest arguments for continued investigation of these two materials come from the reflectivity data, presented earlier, which show them to be able to withstand very lengthy exposures to laser irradiation.

6.5 Laser Induced Lateral Diffusion

A brief report has been made elsewhere[96] of using pulsed irradiation of n-type HgCdTe to form a p-n junction diode. The mechanisms cited in this report are not consistent with our investigation. In particular, the pulse

energy and duration caused temperatures which were estimated by the investigators as being 600-700C, which are far above those arising from a cw CO_2 exposure, as indicated in chapter five. Further, samples in the cited study were not cooled in any fashion, and no work was done to measure mercury lost from the irradiated surface. Lastly, the samples were epitaxial HgCdTe on CdTe. It is the combination of cooled samples, lengthy exposure times, and significant thermal gradients which seems to provide conditions allowing mercury to diffuse over macroscopic distances.

A necessary step in producing this behavior has been shown to be a particular annealing schedule. Recall that as-grown p-type samples showed no lateral diffusion up to exposure times causing surface damage. The necessary anneals include one at elevated temperatures in dynamic vacuum, followed by one in a mercury overpressure at elevated temperatures. Following these two procedures, an exposure to a lengthy CO_2 laser exposure results in the lateral diffusion of mercury.

The mercury overpressure anneal is known to cause mercury diffusion into samples. Mercury is thought to settle on mercury vacancies reducing the concentration of this doubly ionized acceptor, and introducing mercury interstitials as singly ionized donors.[53] This mechanism taken together with the peculiar annealing schedule necessary to observe subsequent lateral diffusion provides evidence that not all of the mercury interstitials arising from the overpressure anneal are electrically active.

Consider an as-grown p-type sample of HgMnTe with a concentration

of, using the standard notation,[97] mercury interstitials $Hg_i^{\cdot}$. Suppose this concentration is substantially lower than the corresponding concentration arrived at in a similar sample after a sequence of a vacuum anneal and a mercury overpressure which is stopped so as to leave the sample p-type.

In the as-grown sample, laser irradiation does not cause a region of n-type conductivity. This can be explained by mercury atoms from the interstitial "reservoir" being too few in number to overcome the vacancy concentration and provide interstitials in the region into which they have diffused.

In the annealed sample the corresponding mercury interstitial "reservoir" (greater than in the as-grown sample by hypothesis) is sufficient to overcome the vacancy concentration, and provide interstitials to cause n-type behavior. Yet, before the laser irradiation the annealed sample was p-type to a degree similar to the as-grown sample.

The presence of the larger interstitial "reservoir" in the annealed sample is supported by the carrier type inversion caused in this sample by laser exposure. However, the fact that both samples are p-type to (approximately) the same degree indicates that a portion of the mercury interstitials in the annealed sample are not electrically active.

Though no experiments have been conducted it is assumed that any source of heat providing sufficient temperatures and temperature gradients within a sample of HgATe, would be capable of causing mercury diffusion. Thus, if cooling is used to eliminate mercury loss from the surface during processing, ion implantation, wirebonding and other procedures causing

significant temperature gradients may result in lateral diffusion of mercury. It would seem that there is indeed a very narrow fence to be walked.

As discussed in chapter four mercury redistribution in HgTe based materials has not been thoroughly studied. For the fabrication of discrete devices a change in material properties of the range of millimeters may not be of crucial concern. However, with the use of large substrates of epitaxial HgCdTe for photodetector arrays material variations from one region to another could prove to be very important.

6.6 Ion Implantation

The fine control of doping that implantation offers in silicon is far from being realized in any HgATe material including HgCdTe. In this study an implantation of $^{10}B^{+}$ ions in HgMnTe was followed by an annealing procedure using a cw CO_2 laser. Safe exposure times (in terms of mercury loss and material damage) were determined by examining reflectivity (t_d) data. The annealing produced an improvement in the electrical properties in regions of the material to a depth of approximately one micron. Neutron depth profiling indicated that the implants were confined to the one micron region and annealing times and temperatures were insufficient to allow dopant redistribution to greater depths. The characteristics of the implanted/annealed region are that of n^{++} material on n or p material of low mobility.

Extensions of the work would require the implantation of other species

into HgATe material with the hope of activating the implant to cause p-type conductivity. If this can be reliably accomplished then there is the potential for producing high quality n-type material by bulk growth and a mercury overpressure anneal or epitaxial techniques. The implantation/anneal process could then produce the p-type portion of a p-n junction. High power laser annealing to produce this activation seems one viable path.[81,98] The low power laser annealing techniques described in this investigation are another path.[99]

The presence of a threshold in laser exposure time and power, below which material damage and mercury loss is minimal or non-existent, can be exploited. In LN_2 cooled samples this threshold time can be five to twenty seconds. A lengthy annealing time at low power has improved the electrical properties of implanted HgMnTe material; an investigation to determine its usefulness in activating other sorts of implants is the logical next-step. If longer annealing times are shown to be desirable then the use of alternative materials should be attempted.

The damage thresholds during laser annealing have been measured in HgMnTe and HgMgTe, and in both cases, for most compositions, are substantially longer than in HgCdTe. As a measure of the ability of a material to withstand laser induced heating the reflectivity technique described earlier is useful. Further, with additional interpretation, the data obtained can be shown to be supportive of theoretical predictions of bond strength in HgCdTe. Lastly, at the extreme of very lengthy annealing times lies the potential for a thermally induced redistribution of mercury within the

irradiated material.

Seebeck mapping has tracked changes in the electrical characteristics of as-grown and annealed HgMnTe. The mosaic patterns of p-type and n-type regions in as-grown material contribute to questionable Hall results. Uniformity may be brought to samples by a sequence of dynamic vacuum and mercury over-pressure anneals. It is this sort of uniform n-type or p-type material that would, ideally, be subjected to implantation. If this implantation were followed by a long (on the order of one minute), low power laser anneal regions of the sample would experience electrically significant amounts of mercury diffusion. This phenomenon extends to depths of more than 50μm, which is far greater than the one micron implant region. Shorter (under the mercury diffusion regime), low power laser anneals were shown to increase the mobility of n-type HgMnTe.

A further complication seems to be that an amount of mercury diffused into HgMnTe during an overpressure anneal is not electrically active. The interaction of this mercury with implanted species could lead to the formation of defect complexes.

6.7 Summary

The purpose of this investigation was to develop a knowledge base for laser processing techniques as they concern novel HgATe materials, and the better known HgCdTe. In particular it was thought that a thorough study of laser annealing applied to ion implanted material would be possible. A

thorough study of this sort proved impossible, but a scaled-down version was completed with positive results. It proved possible to improve certain electrical characteristics of implanted HgMnTe material if sufficient annealing energy (by way of a cw CO_2 laser) were supplied. One difficulty in pursuing a more elaborate implantation/annealing study was due to the substantial preliminary work which proved necessary.

A detailed knowledge of the various HgATe materials' ability to withstand laser exposure was needed. This sub-study results in an ability to choose laser exposure times and power such that little (if any) material damage or mercury loss results. Further, this work makes possible two additional understandings.

The first is a relative scale of "strength" of the Hg-Te bonds within HgATe material. The second is an indication that under certain conditions lengthy laser exposures (and the thermal gradients they generate within the irradiated HgATe material) can result in electrically significant amounts of mercury diffusing over macroscopic distances. The latter phenomenon was documented using a unique two-probe measurement scheme which is based on the Seebeck effect.

The relative strength scale will be useful if there is interest, as there seems to be, as an argument for utilizing alternative HgATe material for device fabrication. Also, it provides empirical verification of theoretical work that predicted the addition of cadmium to HgTe would systematically weaken the Hg-Te bond strength.

The laser-induced mercury diffusion will be an important consideration in designing fabrication processes in a manner as to avoid this phenomenon. Further, the conditions under which this diffusion was noted to occur seem to suggest that a portion of the mercury introduced to HgATe material by way of a mercury overpressure anneal is not electrically active. This possibility itself suggests some items to be considered for future work.

Two other considerations which were discussed deal with the bandgap versus composition relationships for HgATe materials, and the electrical characteristics of these materials as determined by Hall techniques. The former is an especially important consideration in determining the applicability of epitaxial techniques. It was demonstrated that lattice matching substrates to epilayers (of novel material) which have useful bandgaps can be accomplished. The Hall measurements and analysis were done as a verification that the electrical properties of the novel materials were comparable to those that can be obtained in (for example) HgCdTe. This assumption was at least partially confirmed. With the exception of some better quality HgMnTe the characteristics of most of the novel materials would be disappointing by HgCdTe standards of today but not by similar standards of twenty years ago. The technology surrounding novel HgATe materials is, compared to HgCdTe, in its infancy. It is hoped that this work and subsequent suggestions for future work may both encourage basic and applied investigation of HgMgTe, HgSrTe etc. and demonstrate that such investigation is worthwhile.

6.8 Future Work

Two items in particular need substantial work, the first is an in-depth study of the more exotic HgATe materials. HgCaTe and HgSrTe seem viable options and could easily have topped the "strength" rating given in table 6-1. Work to determine the $\rho(x)$ relationship for $Hg_{1-x}Sr_xTe$ and $Hg_{1-x}Ca_xTe$ is needed along with $E_g(x)$ relationships. This study could be conducted with bulk growth techniques optimized to produce more uniform HgCaTe and HgSrTe. The growths would be followed by detailed determination of lattice parameter and electro-optic or spectroscopic determination of bandgap.

The second item is less straightforward and relates to the discussion in chapter four regarding laser-induced mercury diffusion. The diffusion phenomenon itself needs to be studied thoroughly with an eye to determining a detailed mechanism, and consequently a prediction (for device fabricators) of when thermal gradients and the associated conditions are sufficient to cause this diffusion. A more elaborate and systematic version of the annealing/mapping experiments described in earlier chapters might suffice. Though, a more desirable option would be the direct determination of material composition across a suitably prepared and irradiated material by means of a surface analytical technique.

Related to this diffusion phenomenon is the indication that, with a certain processing history, an amount of interstitial mercury can be electrical inactive. A thorough study of this could result in an important understanding of some of the anomalous results that are frequently obtained during Hall

studies of HgCdTe.[95] Despite its importance this study will prove difficult. Once again it would be a matter of analytical analysis resolving tiny differences ($\approx 10^{18}$) in large numbers ($\approx 10^{22}$).

This latter work (diffusion related) should be of pressing technological interest. Still, it is hoped that the results of this present investigation will also provide a degree of motivation for more basic research on novel HgTe-based semiconductors.

References

1. R. Dornhaus and G. Nimtz, "The Properties and Applications of the HgCdTe Alloy System," in *Semiconductor Physics #76*, Springer-Verlag, 1976.
2. S.-H. Wei and A. Zunger, "Role of Metal d States in II-VI Semiconductors," *Phys. Rev. B*, vol. 37(15), p. 8958, 1988.
3. L.T. Specht, W.E. Hoke, S. Oguz, P.J. Lemonias, V.G. Kreismanis, and R. Korenstein, "High Performance HgCdTe Photoconductive Devices Grown by Metalorganic Chemical Vapor Deposition," *Appl. Phys. Lett.*, vol. 48(6), p. 417, 1986.
4. P. Becla, "Infrared Photovoltaic Detectors Utilizing HgMnTe and HgCdMnTe Alloys," *J. Vac. Sci. Technol. A*, vol. 4(4), p. 2014, 1986.
5. D.T. Cheung, "An Overview on Defect Studies in MCT," *J. Vac. Sci. Technol.*, vol. A3(1), p. 128, 1985.
6. K.C. Dimiduk, W.G. Opyd, J.F. Gibbons, T.W. Sigmon, T.J. Magee, and R.D. Ormond, "Annealing of HgCdTe: Hg loss rates and Annealing of Ion Implantation Damage," *J. Vac. Sci. Technol.*, vol. A1(3), p. 1661, 1983.
7. R.F.C. Farrow, G.R. Jones, G.M. Williams, P.W. Sullivan, W.J.O. Boyle, and J.T.M. Wotherspoon, "The Vaporisation of HgCdTe Crystals - a Case of Gross Incongruency," *J. Phys. D.*, vol. 12, p. L117, 1979.
8. *CRC Handbook of Chemistry and Physics*, 68, p. D213, Chemical Rubber Company, 1987.
9. R. Triboulet, T. Nguyen Duy, and A. Durand, "THM, a Breakthrough in HgCdTe Bulk Metallurgy," *J. Vac. Sci. Technol.*, vol. A3(1), p. 95, 1985.
10. B.E. Bartlett, P. Capper, J.E. Harris, and M.J.T. Quelch, "The Effects of Growth Speed on the Compositional Variations in Crystals of Cadmium Mercury Telluride," *J. Crystal Growth*, vol. 46, p. 623, 1979.
11. M.R. Tamjidi and R.E. Kremer, "Composition Gradients in Bridgman-Grown HgMnTe," *Mater. Lett.*, vol. 4(2), p. 90, 1986.
12. M.R. Tamjidi and R.E. Kremer, "Composition Gradients and Segregation in HgMnTe," *J. Crystal Growth*, vol. 55(3), p. 415, 1986.
13. P.L. Anderson, H.F. Schaake, and J.H. Tregilgas, "Precipitation and Phase Stability of (Hg,Cd)Te," *J. Vac. Sci. Technol.*, vol. 21, p. 125, 1982.
14. H.F. Schaake and J.H. Tregilgas, "The Kinetics of Tellurium Precipitation in HgCdTe," *J. Vac. Sci. Technol. A*, vol. 4(4), p. 2181, 1986.
15. D.J. Williams and A.W. Vere, "Tellurium Precipitation in Bulk-Grown HgCdTe," *J. Vac. Sci. Technol. A*, vol. 4(4), p. 2184, 1986.

16. A. Sher, A. Chen, W.E. Spicer, and C. Shih, "Effects Influencing the Structural Integrity of Semiconductors and Their Alloys," *J. Vac. Sci. Technol. A*, vol. 3, p. 105, 1985.

17. A. Sher, A. Chen, and M. van Schilfgaarde, "Correlations in Pseudobinary Alloys," *J. Vac. Sci. Technol.*, vol. A4, p. 1965, 1986.

18. C.E. Jones, K. James, J. Merz, R. Braunstein, M. Burd, M. Eetemadi, S. Hutton, and J. Drumheller, "Status of Point Defects in HgCdTe," *J. Vac. Sci. Technol.*, vol. A3(1), p. 131, 1985.

19. J.K. Furdyna, "Electrical, Optical and Magnetic Properties of HgMnTe," *J. Vac. Sci. Technol.*, vol. 21(1), p. 220, 1982.

20. J.K. Furdyna, "Diluted Magnetic Semiconductors," *J. Appl. Phys.*, vol. 64(4), p. R29, 1988.

21. A. Wall, C. Caprile, A. Franciosi, R. Reifenberger, and U. Debska, "New Ternary Semiconductors for Infrared Applications: HgMnTe," *J. Vac. Sci. Technol.*, vol. A4(3), p. 818, 1986.

22. J.C. Wooley and B. Ray, "Solid Solution in A(II)B(VI) Tellurides," *J. Phys. Chem. Solids*, vol. 13(1-2), p. 151, 1960.

23. J.K. Furdyna, W. Giriat, D.F. Mitchell, and G.I. Sproule, "The Dependence of the Lattice Parameter and Density of ZnMnTe on Composition," *J. Solid State Chem.*, vol. 46, p. 349, 1983.

24. R.W.G. Wycoff, *Crystal Structures, 2nd Edition,* John Wiley & Sons, 1963.

25. *KWIC Guide to the Powder Diffraction File 1969,* ASTM, 1969. PDIS-19K

26. R.L. Srakar and S. Chatterjee, "Electronic Energy Bands of BeS, BeSe and BeTe," *J. Phys. C: Solid State Phys.*, vol. 10, p. 57, 1977.

27. N.P. Gavaleshko, V.V. Kohmyak, V.M. Frasunyak, L.D. Paranchich, and S. Yu. Paranchich, "Energy Band Parameters of MgHgTe, HgSe and CdHgSe Solid Solutions Determined from the Plasma Reflection Minimum," *Sov. Phys. Semicond.*, vol. 18(9), p. 967, 1984.

28. N.G. Gluzman, L.D. Sabirzyanova, I.M. Tsidilkovskil, N.P. Gavaleshko, and V.M. Frasunyak, "Characteristics of the Shubnikov-de Haas Oscillations in HgMgTe Crystals," *Sov. Phys. Semicond.*, vol. 15(8), p. 957, 1981.

29. T.A. Grzybowski and A.L. Ruoff, "Band-Overlap Metallization of BaTe," *Phys. Rev. Lett.*, vol. 53(5), p. 489, 1984.

30. A. Hasegawa and A. Yanase, "Electronic Structure of Sr Monochalcogenides," *J. Phys. C: Solid St. Phys.*, vol. 13, p. 1995, 1980.

31. L. Vegard, "The Constitution of Mixed Crystals and the Space Occupied by Atoms," *Z. Physik.*, vol. 5, p. 17, 1921.

32. J.C. Brice and P. Capper, *EMIS Datareview, Properties of Mercury Cadmium Telluride,* INSPEC, 1987.

33. P. Becla, "HgMnTe Light Emitting Diodes and Laser Heterostructures," *J. Vac. Sci. Technol. A*, vol. 6(4), p. 2725, 1988.

34. E. Janik and G. Karczewski, "Photovoltaic Effect and Carrier Transport Mechanisms in HgMnTe Diodes," *J. Elect. Mater.*, vol. 16(6), p. 381, 1987.

35. Luigi Colombo, A.J. Syllaios, R.W. Perlaky, and M.J. Brau, "Growth of Large Diameter (Hg,Cd)Te Crystals by Incremental Quenching," *J. Vac. Sci. Technol. A*, vol. 3(1), p. 100, 1985.

36. General Electric Company, *Fused Quartz Products*, p. 13, 1987. publication #7700

37. E.R. Plunkett, *Handbook of Industrial Toxicology*, Chemical Publishing Company, 1966.

38. N.I. Sax, *Dangerous Properties of Industrial Materials*, van Nostrand Reinhold Company, 1984.

39. *Operator's Manual: Series CN-2100*, Omega Engineering, Inc., 1984. publication #M197/074

40. *Semiconductors and Semimetals #18: Mercury Cadmium Telluride*, Academic Press, Inc., 1981.

41. P.R. Griffiths and J.A. de Haseth, *Fourier Transform Infrared Spectrometry*, John Wiley & Sons, 1986.

42. J.A. Mroczkowski and D.A. Nelson, "Optical Absorption Below the Absorption Edge in HgCdTe," *J. Appl. Phys.*, vol. 54(4), p. 2041, 1983.

43. B.D. Cullity, *Elements of X-Ray Diffraction*, Addison-Wesley Publishing Company, Inc., 1967.

44. L.B. Tepper, H.L. Hardy, and R.I. Chamberlin, *Toxicity of Beryllium Compounds*, Elsevier, 1961.

45. J.J. Dubowski, T. Dietl, W. Szymanska, and R.R. Galazka, "Electron Scattering in CdHgTe," *J. Phys.. Chem. Solids*, vol. 42, p. 351, 1981.

46. T.M. Moore, "Electron Microprobe Techniques for Routine compositional Analysis of (Hg,Cd)Te," *J. Vac. Sci. Technol. A*, vol. 1(3), p. 1651, 1983.

47. N.G. Blamires and D.H.J. Totterdell, "Orientation Dependent Surface Damage Observed in Laser Irradiated Cadmium Telluride," *J. Phys. D: Appl. Phys.*, vol. 16, p. 2361, 1983.

48. C. Uzan, R. Legros, Y. Marfaing, and R. Triboulet, "CW laser induced low-temperature decomposition of CdTe crystals," *Appl. Phys. Lett.*, vol. 45, p. 879, 1984.

49. D.J. As and L. Palmetshofer, "Laser-Beam Heating and High-Temperature Luminescence of CdTe," *J. Appl. Phys.*, vol. 62, p. 369, 1987.

50. D.H. Auston, "Dynamics of Laser Annealing," in *Laser-Solid Interactions and Laser Processing-1978*, ed. S.D. Ferris, p. 11, 1978.

51. J.A. Silberman, P. Morgen, I. Lindau, W.E. Spicer, and J.A. Wilson, "Room Temperature Stability of Cleaved HgCdTe," *J. Vac. Sci. Technol.*, vol. 21(1), p. 154, 1982.

52. C.K. Shih, D.J. Friedman, K.A. Dertness, I. Lindau, W.E. Spicer, and J.A. Wilson, "Electron Beam Induced Hg Desorption and the Electronic Structure of the Hg Depleted Surface of HgCdTe," *J. Vac. Sci. Technol.*, vol. A4, p. 1997, 1986.

53. Theodore C. Harman, "Analysis of Junction Depths and Lattice Point Defect Interdiffusion Coefficients in HgCdTe," *J. Vac. Sci. Technol. A*, vol. 5(5), p. 3055, 1987.

54. R. Kalish, R. Fastow, V. Richter, and M. Shaanan, "Rapid Annealing of HgCdTe by Immersion in a Hot Mercury Bath," *Appl. Phys. Lett.*, vol. 51(15), p. 1158, 1987.

55. B.M. Vul, V.M. Sal'man, and V.A. Chapnin, "Infrared Absorption Spectra of p-Type CdTe," *Sov. Phys. Semicond.*, vol. 4(1), p. 52, 1970.

56. D.H. Auston, C.M. Surko, T.N.C. Venkatesan, R.E. Slusher, and J.A. Golovchenko, "Time-resolved Reflectivity of Ion-implanted Silicon During Laser Annealing," *Appl. Phys. Lett.*, vol. 33(5), p. 437, 1978.

57. J.R. Ehrstein, "Two Probe Measurements for Evaluation of Semiconductor Materials and Devices," in *Nondestructive Evaluation of Semiconductor Materials and Devices*, ed. J.N. Zemel, p. 1, 1979.

58. K. Seeger, *Semiconductor Physics,* Springer-Verlag, 1979.

59. L.J. Kroko and A.G. Milnes, "A Modified Thermoelectric Method for Determining the Conductivity Type of High Resistivity SiC Crystals," *Solid-State Electronics*, vol. 8, p. 829, 1965.

60. C.L. Jones, M.J.T. Quelch, P. Capper, and J.J. Gosney, "Effects of Annealing on the Electrical Properties of CdHgTe," *J. Appl. Phys.*, vol. 53(12), p. 9080, 1982.

61. J. Tregilgas, J. Beck, and B. Gnade, "Type Conversion of (Hg,Cd)Te Induced by the Redistribution of Residual Acceptor Impurities," *J. Vac. Sci. Technol. A*, vol. 3(1), p. 150, 1985.

62. R.E. Kremer, Y. Tang, and F.G. Moore, "Thermal Annealing of Narrow-Gap HgTe-Based Alloys," *J. Crystal Growth*, vol. 86, p. 797, 1988.

63. S. Cole, G.P. Carey, J.A. Silberman, W.E. Spicer, and J.A. Wilson, "Surface and Bulk Structural Defects in HgCdTe," *J. Vac. Sci. Technol.*, vol. A3(1), p. 206, 1985.

64. L.L. Polisar, N.M. Boinykh, G.V. Indenbaum, A.V. Vanyukov, and V.P. Schastlivyi, "Dislocation Etch Pits on Different Faces of HgTe Single Crystals," *Izvestiyz VUZ. Fizika*, vol. 11(6), p. 81, 1968.

65. R.K. Bagai, Geeta Mohan, G.L. Seth, and W.N. Borle, "Preferential Etchant for Revealing Crystallographic Defects on (111) Te Surface of CdTe Crystals," *J. Crystal Growth*, vol. 85, p. 386, 1987.

66. P.F. Fewster, S. Cole, A.F.W. Willoughby, and M. Brown, "Crystallographic Polarity and Chemical Etching of CdHgTe," *J. Appl. Phys.*, vol. 52(7), p. 4568, 1981.

67. P. Dobrillo and J.S. Blakemore, "Experimental Requirements for Quantitative Analysis of Mid-gap Flaw Concentration in Semi-insulating GaAs Wafers by Measurement of Near-infrared Transmittance," *J. Appl. Phys.*, vol. 58(1), p. 208, 1985.

68. V.N. Strekalov, "Diffusion in Semiconductors under Laser Annealing Conditions," *Sov. Phys. Semicond.*, vol. 20(2), p. 225, 1986.

69. K. Takita, K. Masuda, H. Kudo, and S. Seki, "Observation of Surface Evaporation of Hg from HgTe Crystals by Means of Energetic Oxygen Ion Backscattering," *Appl. Phys. Lett.*, vol. 37(5), p. 460, 1980.

70. W.G. Opyd, K.C. Dimiduk, T.W. Sigmon, and J.F. Gibbons, "Hg Loss Rate Limitation in HgCdTe Thermal Processing," *J. Vac. Sci. Technol. A*, vol. 3(1), p. 276, 1985.

71. F.G. Moore and R.E. Kremer, "Lateral Diffusion of Mercury During Laser Annealing of HgMnTe and Other HgTe-Based Materials.," *Appl. Phys. Lett.*, vol. 52, p. 1314, 1988.

72. M.C. Gold and D.A. Nelson, "Variable Magnetic Field Hall Effect Measurements and Analyses of High Purity, Hg Vacancy (p-type) HgCdTe," *J. Vac. Sci. Technol. A*, vol. 4(4), p. 2040, 1986.

73. D.E. Lacklison and P. Capper, "Hall Effect Measurements on Bridgman-Grown CdHgTe and Their Analysis," *Semicond. Sci. Technol.*, vol. 2, p. 136, 1987.

74. R.L. Petritz, "Theory of an Experiment for Measuring The Mobility and Density of Carriers in the Space-Charge Region of a Semiconductor Surface," *Phys. Rev.*, vol. 110(6), p. 1254, 1958.

75. G.L. Destefanis, "Indium Ion Implantation in HgCdTe/CdTe," *J. Vac. Sci. Technol. A*, vol. 3(1), p. 171, 1985.

76. L.O. Bubulac, W.E. Tennant, D.S. Lo, D.D. Edwall, J.C. Robinson, J.S. Chen, and G. Bostrup, "Boron and Indium Ion Implanted Junctions in HgCdTe Grown on CdTe and CdTe/Al(2)0(3)," *J. Vac. Sci. Technol.*, vol. A4, p. 2169, 1986.

77. S.Y. Wu, W.J. Choyke, W.J. Takei, A.J. Noreika, M.H. Francombe, and R.B. Irwin, "Effects of Implantation and Annealing Temperatures on Implantation Induced Damage in HgCdTe," *J. Vac. Sci. Technol.*, vol. 21(1), p. 255, 1982.

78. L.O. Bubulac and W.E. Tennant, "Role of Hg in Junction Formation in Ion-Implanted HgCdTe," *Appl. Phys. Lett.*, vol. 51(5), p. 355, 1987.

79. R.C. Bowman, J.F. Knudsen, R.G. Downing, and R.E. Kremer, "Distribution of Boron Atoms in Ion Implanted Compound Semiconductors," *Mat. Res. Soc. Symp. Proc.*, vol. 126, 1988.

80. G.L. Destefanis, "Ion Implantation in HgCdTe," *Nuc. Insts. and Mtds.*, vol. 209/210, p. 567, 1983.

81. R. Kalish, *Laser Annealing of Ion Implanted HgCdTe*, 22 October 1984. Final Scientific Report for Air Force Office of Scientific Research

82. G. Bahir and R. Kalish, "CW CO_2 and Ruby Laser Annealing of Ion-Implanted HgCdTe," *Appl. Phys. Lett.*, vol. 39(9), p. 730, 1981.

83. K.L. Conway, W.G. Opyd, M.E. Greiner, J.F. Gibbons, T.W. Sigmon, and L.O. Bubulac, "Thermal Pulse Annealing of Boron-Implanted HgCdTe," *Appl. Phys. Lett.*, vol. 41(8), p. 750, 1982.

84. M. Lax, "Temperature Rise Induced by a Laser Beam," *J. Appl. Phys.*, vol. 48, p. 3919, 1977.

85. O. Svelto, *Principles of Lasers*, Plenum Press, 1982.

86. I.S. Gradshteyn and I.M. Ryzhik, *Table of Integrals, Series, and Products*, p. 307, Academic Press, 1980.

87. I.S. Gradshteyn and I.M. Ryzhik, *Table of Integrals, Series, and Products*, p. 930, Academic Press, 1980.

88. J.E. Moody and R.A. Hendel, "Temperature Profiles Induced by a Scanning CW Laser Beam," *J. Appl. Phys.*, vol. 53(6), p. 4364, 1982.

89. F. Ferrieu and G. Auvert, "Temperature Evolutions in Silicon Induced by a Scanned CW Laser, Pulsed Laser, or an Electron Beam," *J. Appl. Phys.*, vol. 54(5), p. 2646, 1983.

90. M.L. Burgener and R.E. Reedy, "Temperature Distributions Produced in a Two-Layer Structure by a Scanning CW Laser or Electron Beam," *J. Appl. Phys.*, vol. 53(6), p. 4357, 1982.

91. M. Lax, "Temperature Rise Induced by a Laser Beam II. The Nonlinear Case," *Appl. Phys. Lett.*, vol. 33(8), p. 786, 1978.

92. M. Yamada, K. Nambu, and K. Yamamoto, "Nonlinear Calculation of a Temperature Profile Produced in a Two-Layer Structure by a Scanning CW Elliptical Laser or Electron Beam," *J. Appl. Phys.*, vol. 57(3), p. 965, 1985.

93. I.D. Calder and R. Sue, "Modeling of CW Laser Annealing of Multilayer Structures," *J. Appl. Phys.*, vol. 53(11), p. 7545, 1982.

94. L.J. van der Pauw, "A Method of Measuring Specific Resistivity and Hall Effect of Disks of Arbitrary Shape," *Philips Res. Rep.*, vol. 13, p. 1, 1958.

95. D.S. Pan, Y. Lu, and M. Chu, "Constant-Current-Density Model for the Anomalous Hall Effects in HgCdTe," *Appl. Phys. Lett.*, vol. 53(4), p. 307, 1988.

96. R.V. Lutsiv, V.G. Savitskii, G.V. Playtsko, A.A. Druzhinin, B.K. Kotlyarchuk, N.N. Vasyuk, and S.G. Kiyak, "Action of Laser Radiation Pulses on n-CdHgTe," *Sov. Phys. Semicond.*, vol. 12(3), p. 247, 1978.

97. F.A. Kroger, *The Chemistry of Imperfect Crystals,* 2, North-Holland/American Elsevier, 1974.

98. R. Kalish and G. Bahir, "Formation of p on n Photodiodes in HgCdTe by Ion Implantation and cw CO_2 Laser Annealing," *J. Crystal Growth,* vol. 72, p. 474, 1985.

99. R.E. Kremer, F.G. Moore, M.R. Tamjidi, and Y. Tang, "Laser Annealing of Narrow Gap HgTe-Based Alloys," *Mat. Res. Soc. Symp. Proc.,* vol. 90, p. 241, 1987.

100. G.G. Johnson and E.W. White, *X-ray Emission Wavelengths and KeV Tables for Nondiffractive Analysis,* 1970. ASTM Data Series DS-46

101. R.A. Smith, *Wave Mechanics of Crystalline Solids, 2nd edition,* Chapman and Hall, 1969.

102. A.F. Ioffe, *Physics of Semiconductors,* Academic Press, 1960.

Appendix A

XES Analysis

X-ray energy spectra analysis (XES) is a mature technology, versions of which are invaluable for determining the surface and near-surface elemental composition. Particular forms of this technique have been applied to compositional analysis of HgCdTe.[46] For the purposes of this investigation analysis was done on HgATe materials with the intention of tracking the relative amount of mercury present before and after various processing steps have been carried out. Since no calibration standards are available for the materials that will be investigated, this technique will only be able to track the relative amounts of mercury that is lost.

The system used is made by EG&G Ortec and is mounted to a JEOL JSM-35 scanning electron microscope. The particular type of analysis is known as energy dispersive x-ray analysis or EDX. The basis of the technique is to use a calibrated multichannel analyzer to examine the x-ray spectrum given off by a sample while an electron beam is incident upon it. By knowing the characteristic $K\alpha,\beta$ and $L\alpha,\beta$ spectra of the component elements an area-under-the-curve calculation can be preformed to give the elemental ratios.

An important portion of the analysis is the determination of which regions of the energy spectrum will be tagged as being indicative of a partic-

ular element. Tables are available[100] which list the characteristic emission wavelengths (or energies) of all the elements. Table A-1 lists the spectral regions' definitions for HgMnTe which were used during this investigation.

Strictly speaking most uncapped HgATe materials are not compatible with vacuum. Since XES techniques cannot be used to probe through a capping material, some mercury loss from the surface regions of samples may be unavoidable. This loss was minimized by keeping the analysis times to a minimum, and by using a moderate accelerating potential (15-20 keV), to reduce sample heating.

Appendix B

Hall Analysis

The very simple Hall system that was used is illustrated in figure B-1. As mentioned in chapter four the sample holder is somewhat unique, in that it allows four symmetric pressure contacts to be made which are suitable for van der Pauw analysis, while minimizing damage to the sample. The sample holder arrangement is illustrated in figure B-2.

The system is suitable for measurements at a variety of temperatures from 77K to 325K. No systematic study as a function of temperature was completed and discussion here will be limited to results from room temperature and 77K.

In positioning the sample there is complete rotational freedom. This freedom was used to hand-optimize the Van der Pauw F factor to be as close to unity as possible. With F = 1 behavior with forward and reverse polarity is symmetrical between the appropriate contacts. Typically, samples were measured after achieving $F = 1 \pm 0.005$.

Samples were analyzed using two different models for the Hall data. The first assumed a one-carrier type of conduction, and is reasonably accurate for strongly n-type material. This model would be expected to work well on material that has received an mercury overpressure anneal.

For samples that were implanted a two layer model[74] was adopted. Since neutron depth profiling showed that the implanted species was confined

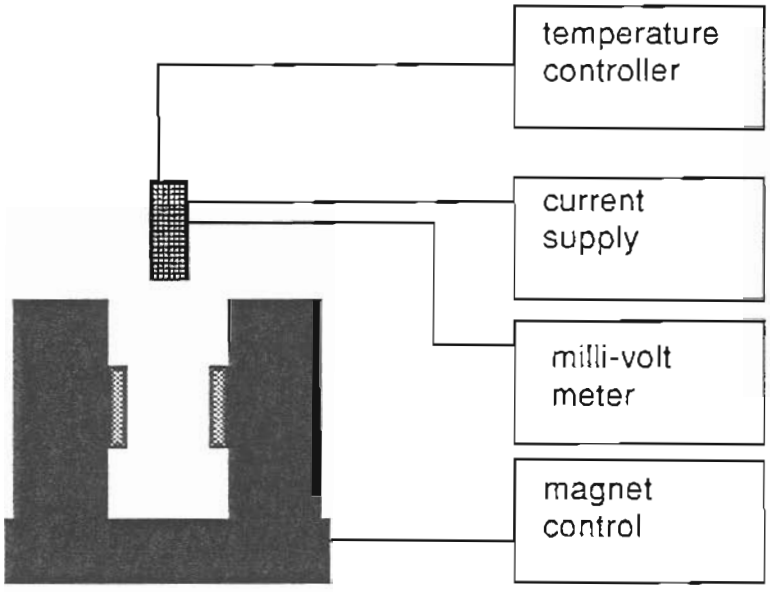

Figure B-1 A simple Hall system capable of taking data at temperatures between 77k and 320k.

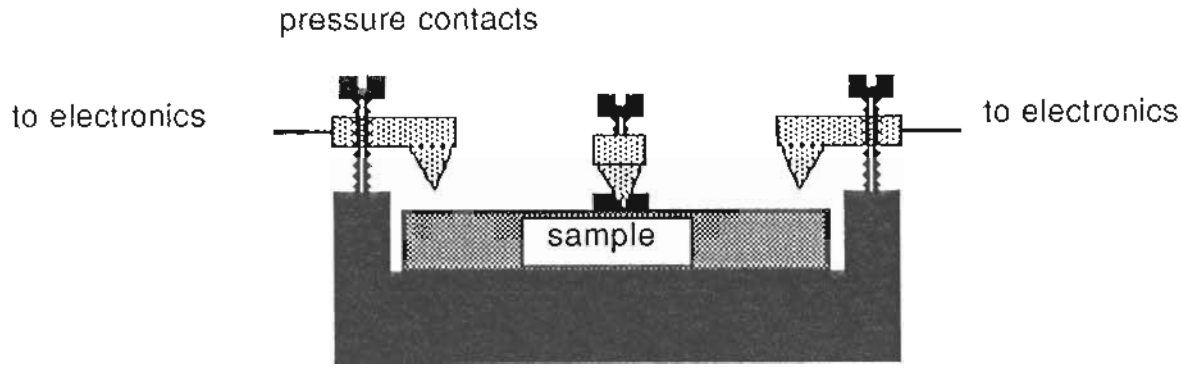

Figure B-2 The Hall sample holder is designed to inflict minimal damage on the samples so Hall data may be taken nondestructively. The four pressure contacts are at right angles to each other and equidistant from the center of the sample (van der Pauw configuration). The contacts are adjusted by hand and their ohmic nature can be maintained at low temperatures if the arrangement is cooled slowly.

to a layer of approximately one micron in thickness, this analysis assumed a thin n-type surface layer of an appropriate thickness and an underlying bulk. The bulk region was assumed to have remained unchanged from its before-implant condition while the surface layer was assumed to be n-type with a fairly low mobility. This data and an interpretation of it is given in chapter four.

Appendix C

X-ray Analysis and Material Composition

X-ray powder diffraction analysis is a technique indirectly suited to compositional studies. In this investigation the technique was used to determine lattice parameters in a variety of HgTe based materials. Since in $Hg_{1-x}A_xTe$ the lattice parameter is a function of x, $a_o = a_o(x)$, these measurements can be used to verify other compositional measurements, and to provide new information about the function $a_o(x)$ itself.

Sample preparation begins by obtaining an amount of high-quality industrial silicon for use as an internal standard. The silicon is then powdered in a mortar and pestal several grams at a time and stored for later use. Subsequent powdering of HgATe material is done in the same mortar and pestal. Before each of these preparations an amount of the previously powdered silicon is introduced and worked in the mortar and pestal with the intention of removing as much of what HgATe material might remain as possible. A small amount of the new HgATe material is added and powdered, this is discarded and finally another slightly larger amount of the same HgATe material is powdered and retained.

A half-and-half mix of the HgTe sample powder is mixed with silicon powder and combined thoroughly on a weighing paper. A sample holder has been fitted with a small amount of clay to hold the powder. The powder mixture is poured onto the clay and arranged in as flat a pattern as possible.

A flat surface, (microscope slides work well) is then put against the powder and used to push the powder into the clay. The sample holder can then be transferred to the diffractometer and data acquisition may begin.

The Siemens D500 system that was used in this investigation is provided with a great deal of software for data acquisition and analysis. In particular there are calibration routines and lattice parameter refinement programs based on algorithms that are something of an industry standard.

The internal standard software will examine a datafile containing peak position and intensity information and search for the peaks that correspond to the known standard. The routine then calculates a correction based on the measured position of the standard peaks. Lastly the routine removes the standard peaks and corrects the remaining peaks. This routine effectively removes errors arising from machine calibration and sample positioning.

Finally a lattice parameter refinement routine is used. Input to this routine consists of a "best guess" of lattice parameter and lattice type (cubic in this case). To provide this routine with a starting point Vegard's law is used in conjunction with density measurements to predict an approximate value of lattice parameter.

Vegard's law was initially proposed for binary systems, but it can be extended to psuedo-binary systems of the form $AB_{1-x}BC_x$. Vegard's law then relates the lattice parameter of the psuedo-binary (i.e. ternary) to those of the two binaries in a linear fashion. Results presented in chapter three indicate that a linear relationship is quite a satisfactory starting point, and

the resulting refinements correspond well with density and spectroscopic measurements.

Appendix D

FTIR Analysis

Fourier transform infrared spectrometry (FTIR) has become common in recent years as a result of advanced computing technology that is able to perform discrete fourier transforms on large data arrays very quickly. The theory and technology behind this technique is discussed at length in many references. The use of this technique is overkill for this study in that it is only used to obtain cut-on wavelength information in a variety of HgATe materials. A Digilab FTS-60 was used in the investigation. The system is capable of far higher resolutions than necessary, and unfortunately tends to present information in terms of wavenumbers with units of cm^{-1} (inverse wavelength) instead of wavelength in microns or angstroms or even energy in electron-volts.

Samples need to be fairly thin, on the order of 100 microns in thickness to achieve sufficient transmission. Further, it is important that the materials be n-type. This latter is necessary because of the discussion in chapter four concerning intra-band transmissions in p-type semiconductors. Samples were prepared by annealing in a mercury overpressure. These samples then had a few microns lapped and polished from one face, the remaining material was removed from the other face in order to eliminate any p-type core of material that might remain.

Several tricks in the data acquisition were used to produce more reason-

able spectra. A beam condenser was used in the Digilab system combined with an increase in source intensity and detector gain. The result of this procedure is that the absolute values of transmission (or absorption) calculated by the system are not accurate, but the position of the cut-on edge remains accurate.

This trickery and the corresponding loss of absolute accuracy in transmission was deemed an acceptable tradeoff for two reasons. First, thinning samples is difficult and half of the samples breaking during thinning to 100 microns is not uncommon. Secondly the reduction of noise to an acceptable level by averaging takes considerable time. This problem can be managed by increasing the intensity of the probe beam beyond the level at which the detector would saturate if there were no sample attenuating the beam.

Appendix E

Sample Preparation

This discussion of sample preparation will attempt to cover in some detail the techniques and tricks that are employed to cut, clean, lap, polish, mount and generally produce a sample arrangement suitable for some sort of investigation. Specifically excluded from this section is the preparation of a powdered sample for x-ray work, this is discussed in appendix C.

The actual storage of samples is of some concern. There have been studies attempting to measure changes in surface composition and structure after long term exposure to ambient laboratory temperatures and atmosphere. Our own investigations have indicated that over periods of time stretching to months there is negligible change in the physical properties of most materials. The exception to this generalization are several samples of the more exotic alternative materials that were grown.

With strontium, calcium and barium based mercury tellurides, portions of the growths were subject to significant degradation over a period of days to weeks. Without exception the initial inspection of these samples indicated that something was amiss. Density measurements indicated that an exceptionally high percentage of mercury had been replaced by the third element. A sample might be measured as having a density 30 percent less than HgTe. The change in density is thus in the direction that would be expected if large amounts of the third element were present.

In HgMnTe and HgMgTe the accepted solubility limit of manganese and magnesium are, respectively, $x \approx 0.35$, and $x \approx 0.2$. Both MnTe and MgTe do not form in the zincblende structure naturally. Since SrTe, BaTe and CaTe are not zincblende is is suspected that there will be a solubility limit and that above this (undetermined) limit mixed crystal phases will be present.

These samples tend to be discolored, pitted and riddled with voids. Many of them began crumbling shortly after the final sectioning was done and have subsequently been reduced to powder. Others have developed what appears to be an oxide layer, but retain their structural shape. No diagnostic work beyond density measurements have been attempted on these samples. If portions of an ingot survive removal from the growth ampoule initial cutting and density measurements (see chapter three), they are mounted to a jig, lapped and polished.

The mounting is facilitated by having at least one reasonably flat sample face. Several mounting techniques have been employed but the one meeting with the most success involves slightly elevated temperatures. The jig is heated slightly to 60-70C by use of a hotplate. The mounting surface of the jig is kept upright and an amount of crystalized phenyl salicylate is allowed to melt on this surface. A reference mark placed on the jig was used to index a number of samples which were placed on the wetted mounting surface. The jig may be left to cool or can be transferred to a holder/heatsink arrangement to speed cooling. When cool the phenyl salicylate will hold the samples firmly on the jig.

Typically several grades of abrasive slurry or wet lapping paper are used followed by a final polish using 0.05 micron alumina oxide on a cloth covered wheel. The mirror finish thus obtained has proven suitable for subsequent investigations. After polishing one side of the sample the jig, with the sample still attached, is cleaned with water and methanol and carefully heated to melt the phenyl salicylate. The samples are turned over, and a small amount of phenyl salicylate may be added and allowed to flow around the samples, and the jig is once again cooled. The above lapping procedure is repeated, but since the first lapping should have established a uniform sample thickness little material should need to be removed. The final polish with alumina oxide is also repeated. The samples are dismounted by heating slightly, and taking care to maintain a known order are washed in methanol. Finally the samples are returned to storage or advanced to the next preparation stage.

For purposes of reflectivity and EDX measurements it proved desirable to cut a polished and lapped sample into subsamples. The samples are typically very fragile and simply mounting them to a graphite cutting block and sawing has proven unsatisfactory. The alternative technique developed is a rather elaborate wax-encasement method that greatly enhances the survival rate of subsamples.

The mold used in this technique is shown in figure E-1. The interior of the mold is coated with silicon based vacuum grease to facilitate removal and the sample is placed on the pedestal. A supply of Kerr "sticky wax", an orange wax with applications in dentistry, is heated until very fluid and poured into the mold. The wax is allowed to cool for several minutes, the

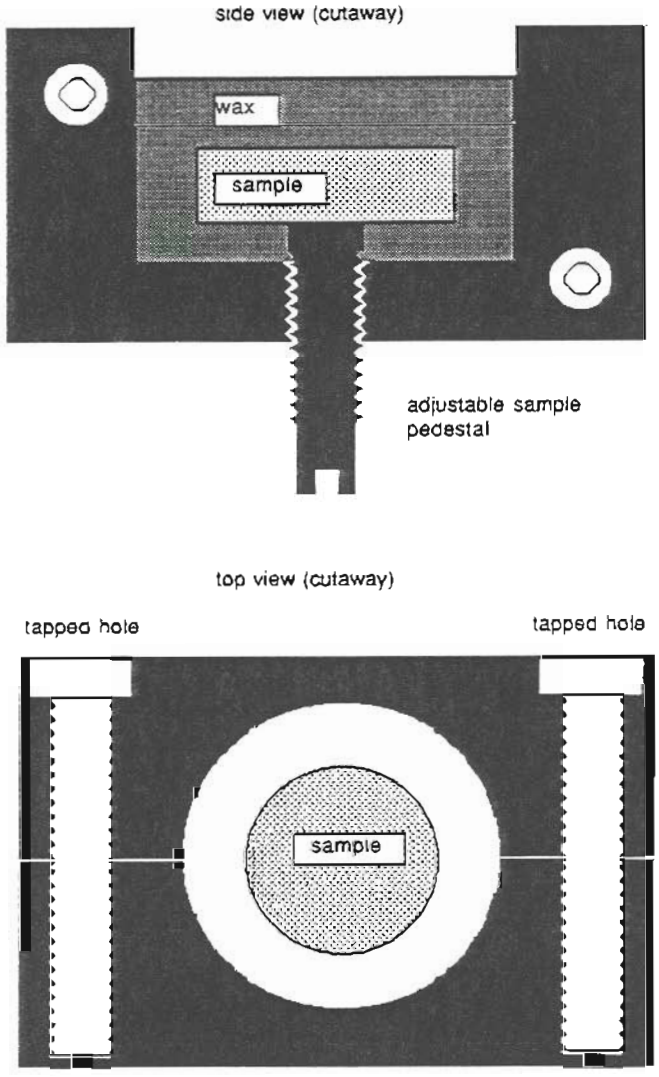

Figure E-1 A sample is placed on the pedestal within the mold and heated wax poured around the specimen. The mold is then removed and the encased sample transferred to a low-speed diamond saw for cutting.

mold is separated, and the casting removed. The encased sample is then placed on a warmed cutting block and allowed to adhere.

An important concern is that the amount of wax poured into the mold above the sample be sufficient to allow the cutting wheel to pass entirely through the sample, several millimeters is sufficient. Secondly, some care is needed in attaching the casting to the cutting block. If the block is overly hot the casting will melt down to the sample and this insufficient backing will prevent the sawblade from cutting through the sample. Thirdly, it is advisable to try and settle the casting onto the cutting block so as to keep the surface of the encased sample parallel to that of the cutting block.

The cutting block with attached casting is next transferred to the low speed diamond saw. Adjusting the cutting speed again requires a practiced hand. A cut through the center (i.e. thickest portion) of the casting should be arranged to take twenty to twenty-five minutes. For a sample one centimeter in diameter sections two millimeters square may be obtained by making four cuts across the casting. When these cuts are made the cuts are blown free of liquid by compressed air and a heated flat edge is passed over the surface of the casting to allow some melted wax to flow into the cuts and aid in holding the casting together. The sample stage is then rotated 90 degrees and four more cuts are made. These last four cuts take less time since some of the sample has already been removed as kerf. Again, adjust the counterweight so as to take twenty to twenty-five minutes to do the center cut.

Removing the subsamples from the casting is a tedious procedure. The wax may be dissolved in heated TCE, but it has proven more expedient to remove some of the wax first. The cutting block is heated slightly and the casting removed. The casting is then placed on a large aluminum block that has been heated to a temperature that allows the wax to melt slowly. Again, a practiced eye is the best judge of this temperature. As the wax slowly melts the subsamples my be removed using a pair of fine tweezers.

The subsamples are washed thoroughly with with deionized water. They are next boiled in TCE over a waterbath for two minutes. The TCE is decanted and the samples are rinsed three times in acetone then three times in methanol, and finally removed.

Subsamples prepared in this manner are typically destined to undergo the reflectivity technique discussed in chapter four and appendix G. To facilitate this subsamples are mounted and labeled. A square or rectangular section of flat quartz is an ideal mounting surface. The number of samples mounted to a single quartz holder may vary but there should be room to label each subsample with a permanent marker. Further the subsamples should be separated by several millimeters to insure that the incident laser beam does not cause any unintentioned heating. Off-the-shelf super-glue works well as an adhesive and a pair of fine tweezers is necessary to position the subsamples on the quartz. The mounting and labeling arrangement is illustrated on the following page in diagram E-2.

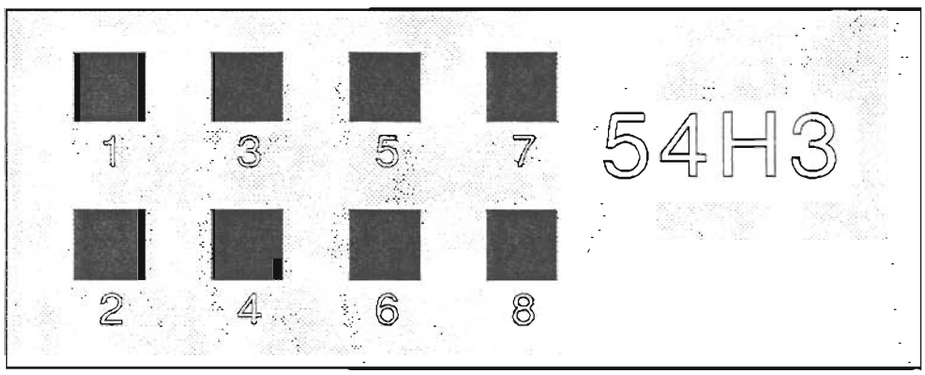

Figure E-2 Sectioned samples (subsamples) are mounted to a piece of flat quartz to facilitate handling. The quartz is labeled with a permanent marker. This arrangement is suitable for mounting subsamples for reflectivity analysis or for EDX analysis.

wards toward the horizontally mounted target. The shutter is equipped with a turning mirror, and a thermal power meter may be arranged so as to meas-

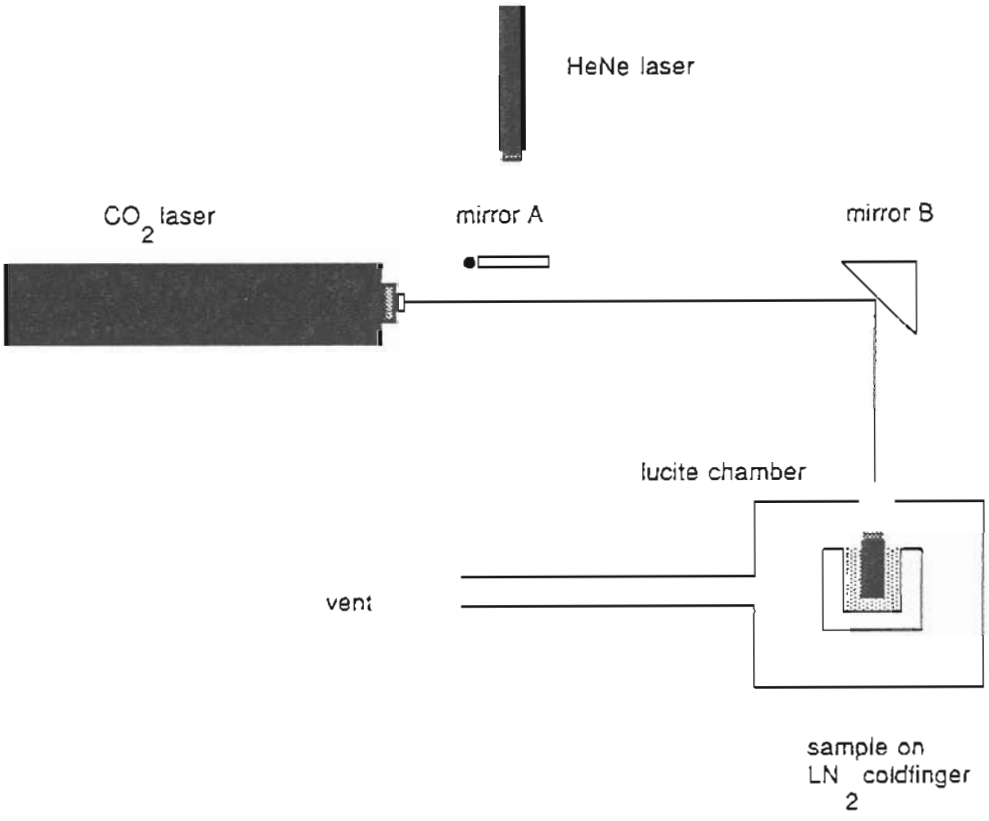

Figure F-1 Laser annealing system using a cw CO_2 laser and a vented sample chamber with a LN_2 coldfinger. The laser is mounted horizontally to an optical bench and a turning mirror directs the beam vertically downward onto the sample. The sample chamber is lucite and is intended to confine any escaping mercury vapor so it can be adequately vented.

ure the beam when the shutter is closed. When activated the shutter drops out of the beam exposing the target. When the exposure is complete the laser itself is powered down. The HeNe is used to align the next target, the shutter is manually reset, the CO_2 laser fired and the cycle repeated if necessary.

The beam diameter ($\frac{1}{e^2}$ point) is specified to be 6 millimeters. No effort has been made to characterize this but the assumed value is consistent with experimental results. The pathlength from output mirror to target surface is 0.75 meters.

The cold finger arrangement allows a sample to be mounted to a large thermal mass (brass), which is in contact with a reservoir of liquid nitrogen. Thermocouples attached to the cold finger with vacuum grease indicate temperatures of between 85-90k on the mounting surface of the cold finger.

Appendix G

Reflectivity Analysis

The reflectivity experiments undertaken within this investigation are based partially on similar techniques used to detect the melting of semiconductor surfaces during laser recrystalization work. In recrystalization work a probe beam, commonly a milliwatt HeNe laser, is made to be coincident on a surface with a beam powerful enough to melt the surface. The reflected intensity of the probe beam is monitored. The reflectivity is observed to increase when melting occurs and to return to its original value if the surface is allow to solidify. With HgTe based material individual subsamples were optically inspected after exposure to CO_2 laser radiation. The samples' surfaces, initially of high optical quality, were seen to lose this quality with sufficient exposure time and/or power.

To measure this degradation as a function of time the instrumentation in figure G-1 was arranged. A probe beam from a milliwatt HeNe laser is incident at approximately 45 degrees. The reflected beam is measured by a photovoltaic detector whose response is insignificant at 10.6μm. The output of the detector is amplified and used to drive the y-axis of a chart recorder. The x-axis of the recorder is driven by a time base. The time base is started by the shutter dropping out of the beam.

Typical traces from a reflectivity run are given in figure 4-4. The traces show a plateau followed by a sudden increase in reflectivity followed by a

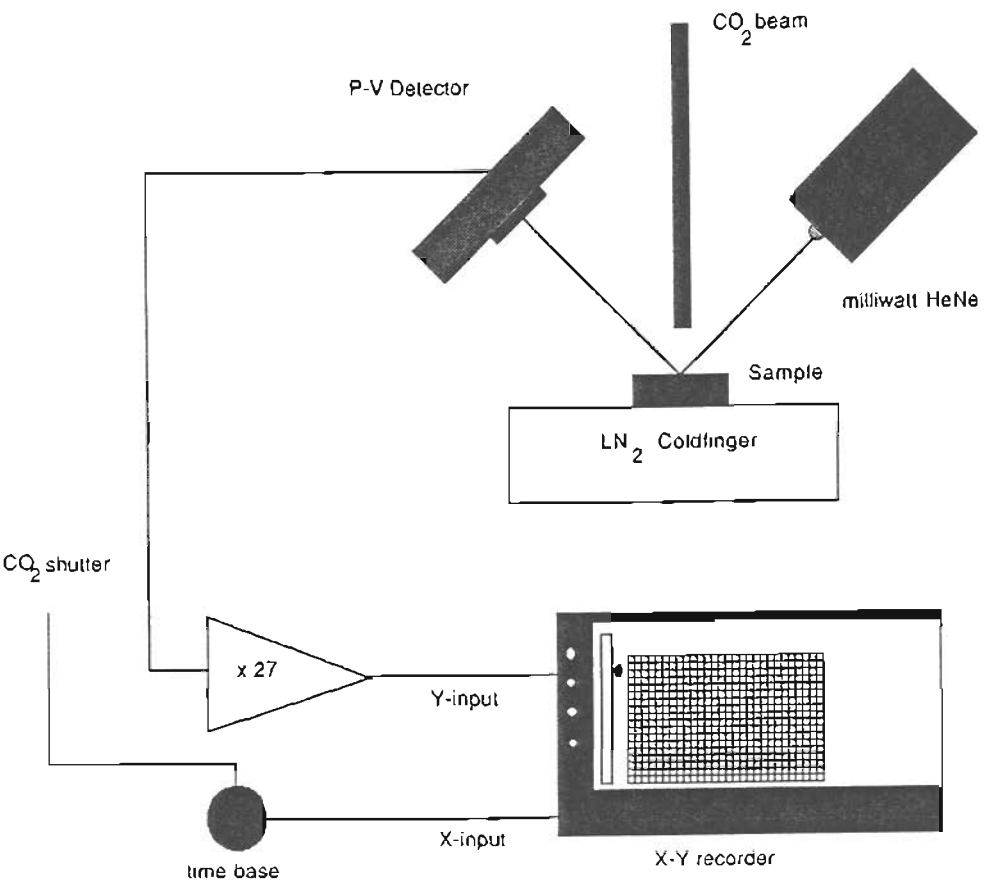

Figure G-1 This arrangement allows a shuttered laser beam to irradiate a sample of HgATe material while the reflected intensity of a HeNe probe beam is monitored by an x-y recorder. As the optical surface of the sample begins to degrade a drop in reflectivity is observed.

drastic and permanent drop in reflectivity. The sudden increase may be attributed to surface melting. The permanent decrease is connected with a dramatic loss of mercury from the surface regions of the sample as is discussed in chapter four.

Appendix H

Thermal Annealing

Two types of thermal anneals were done regularly on HgTe based material. An anneal in dynamic vacuum is done on samples while the vessel containing them it being pumped with a mechanical roughing pump. Typical pressures obtained are in the range of 50 millitorr.

Vacuum anneals are intended to deplete the surface and near surface regions of the sample of mercury. At elevated temperatures mercury diffuses out of the sample and its vapor is evacuated through the roughing pump. These anneals typically last on the order of hours.

The second type of anneal is done at elevated temperatures in the presence of mercury vapor. A special ampoule with a mercury reservoir is used and it is drawn in figure H-1. A drop of mercury is poured into the reservoir the samples are placed in a quartz holder and are introduced to the ampoule. The ampoule is carefully sealed off at atmospheric pressure using a hydrogen-oxygen torch. The ampoule is then positioned in a horizontal furnace which is ramped to temperature, typically 150-300C for times ranging from days to weeks.

Opening the mercury annealing ampoule requires a hydrogen-oxygen torch and a file. The sample holder is carefully caused to slide to one end of the ampoule. The ampoule is then placed on a flat heat-proof surface, scored with the file and heated with the torch in the scored area. As the quartz

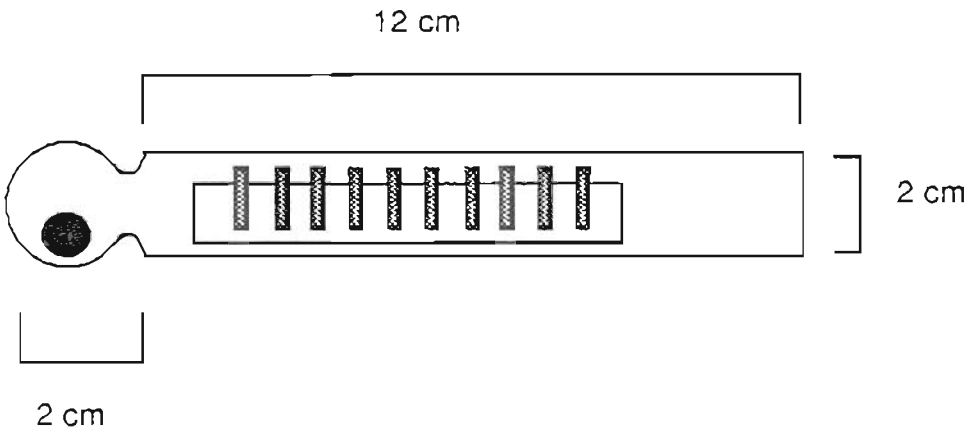

Figure H-1 A drop of mercury is introduced into the ampoule and allowed to come to rest in the rounded end. The samples are then introduced and the ampoule is sealed. The sample holder consists of a piece of quartz tubing, through which partial cuts are made with a high-speed cutoff saw. The kerf is sufficient to allow samples to rest in the resulting cut.

begins to collapse around the score mark the torch is removed and cold water poured onto the hot quartz. A series of fine cracks should result from this procedure. The cracked end of the ampoule is then struck and broken. The sample holder can then be removed after the quartz has cooled.

Appendix I

Seebeck Effect

A standard derivation of the one dimensional Seebeck effect in semiconductors is presented by Smith,[101] and is treated in a slightly different manner by Ioffe.[102] The final result is given by:

$$P = -\frac{k}{e}\left[\frac{n\mu_e\left\{\left(\frac{5}{2} - s\right) + \ln\left(\frac{N_c}{n}\right)\right\} - p\mu_h\left\{\left(\frac{5}{2} - s'\right) + \ln\left(\frac{N_v}{p}\right)\right\}}{n\mu_e + p\mu_h}\right] \qquad \text{H.1}$$

where the density of states N_v and N_e are given by:

$$N_v = 2\left(2\pi m_h \frac{kT}{h^2}\right)^{\frac{3}{2}} \quad \text{and} \quad N_e = 2\left(2\pi m_e \frac{kT}{h^2}\right)^{\frac{3}{2}},$$

and where the ratio $\frac{k}{e}$ has the numeric value of $8.6 \times 10^{-5}\ \frac{V}{C}$. The factors s and s′ are small positive numbers which depend on the scattering that occurs within the semiconductor. Figure I-1 gives a diagram of the arrangement which leads to the generation of a thermoelectric voltage.

When a heated contact is applied to a semiconductor sample a non-zero temperature gradient is established within the material. This gradient leads to a non-symmetrical rearrangement of majority and minority carriers. A space-charge region is thus established and consequently an electric field that eventually halts further rearrangement of carriers. It is the potential drop across this region of non-zero electric field which is measured and alterna-

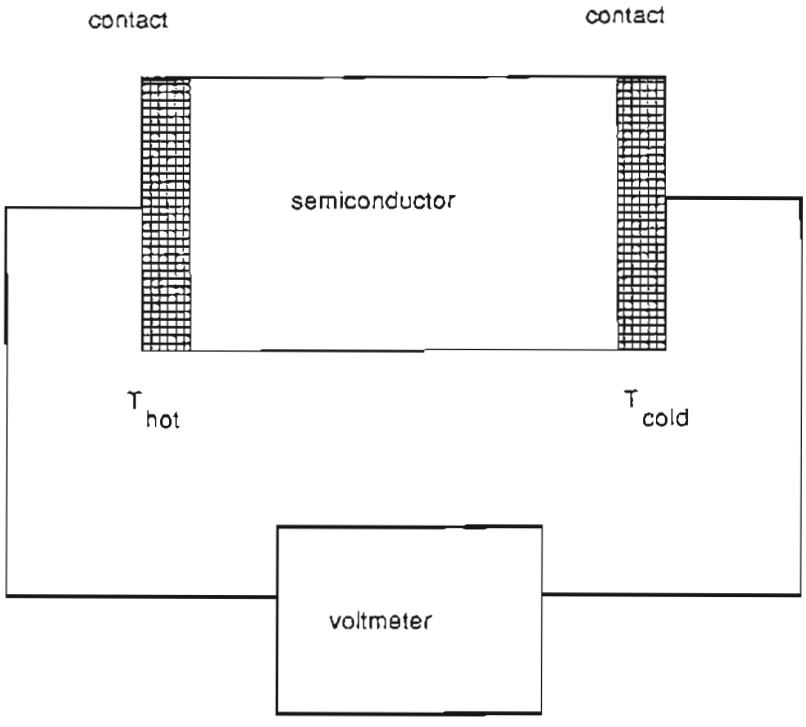

Figure I-1 If no current is allowed to flow this arrangement of contacts on a semiconductor sample gives rise to what is known as the Seebeck voltage. The thermal equilibrium of the material is disturbed and carriers rearrange themselves under the new conditions. This results in a non-zero electric field in the material which can be measured as a potential difference.

tively referred to as a thermoelectric or Seebeck voltage.

The voltage is quite small, on the order of $\frac{k}{e}$ millivolts per degree of temperature difference, and is generated within the region of semiconductor with non-zero temperature gradient. The polarity of the measured voltage depends on the majority carrier type. This is seen more clearly by writing the thermal voltage as:

$$P = \frac{\sigma_e P_e + \sigma_h P_h}{\sigma_e + \sigma_h} \qquad \text{H.2}$$

and realizing that by definition $P_e \geq 0$ while $P_h \leq 0$.

This sort of thermal probing is widely used and is an important complement to Hall measurements since it gives an indication of whether the material in question has adjacent regions of inverted majority/minority carrier types. Though a useful, qualitative technique, it is most difficult to use in a quantitative sense because of the simplifications made to obtain an analytic solution to the Boltzman transport equation. Smith's derivation assumes:

- a one dimensional analysis with no edge effects,
- that carrier scattering varies as E^{-rs},
- a constant thermal gradient $\frac{dT}{dx} = K$,
- the thermal gradient's perturbation of equilibrium is small enough that thermal equilibrium relationships can be used when convenient.

A thorough treatment of this problem goes well beyond the scope of an experimental dissertation. No elaborate interpretation of the precise numerical values of voltage obtained during these measurements will be offered. The reader is referred to the section on Seebeck mapping for a discussion of the qualitative interpretation that can be made.

The experimental system to perform Seebeck mapping is given in figure I-2. The main components of the system include an Apple II+ computer equipped with serial I/O cards and an ADALAB interface card. A Daedal x-y translation stage, translation/control electronics and a linear stepper motor, also controlled by the computer, are used to move sample and to raise and lower the heated probe.

The two types of probe arrangements are detailed in figure I-3. A probe of type A was expected to be more suitable for bulk material whereas the type B probe would be better for epitaxial material or for material whose surface regions had distinct properties. Strangely enough maps obtained from the same samples using different probes are virtually identical.

A typical mapping procedure will begin with the selection of a sample that has been lapped and polished as described in appendix E. The sample is mounted to an aluminum jig that is approximately 2 cm square and several millimeters thick. If probe A is to be used then this mounting must be conductive and is accomplished with a silver paste (DuPont #7941), which cures in 20 minutes at 75C. If probe B is to be used no electrical path through the aluminum jig is necessary, and though the silver paste may be

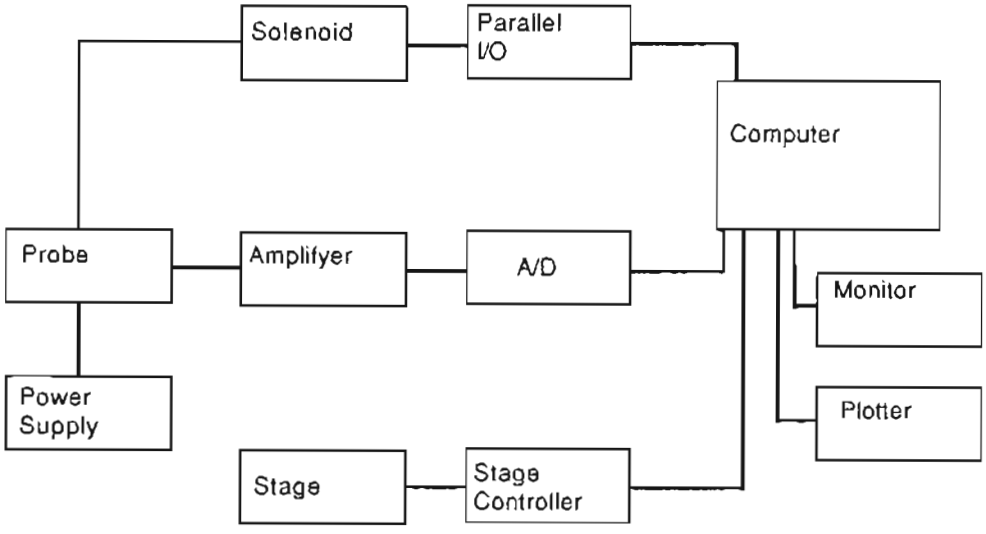

Figure I-2 Instrumentation used for probing across the surface of sample, and measuring the thermoelectric or Seebeck voltage generated at each point. The sample, and probe motion is controlled by computer which also collects and records the measured voltages. Output is provided by means of on-screen graphics or a multicolor plot.

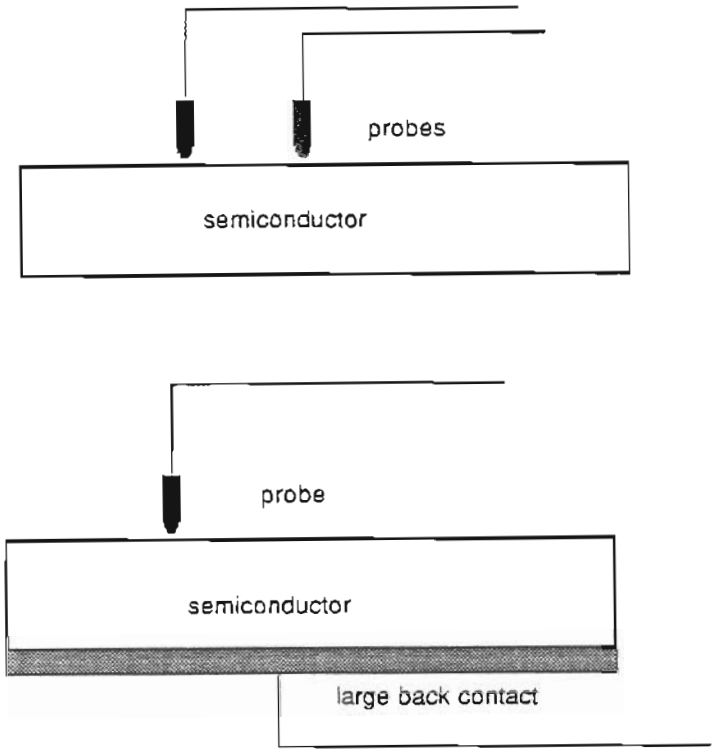

Figure I-3 Both probe arrangements given in the diagram have been used extensively. Since the thermal voltage is generated in a small region around the heated probe the two arrangements tend to give similar results. It was at first thought that the probe in diagram A would be more suitable for analysis of bulk material, and the probe in diagram B for epitaxial material. Both types work well on bulk material, virtually no work was attempted with epitaxial material.

used, standard office-type rubber cement works well. The aluminum jig, with attached sample, is next mounted to the translation stage, which has manually been moved away from the hot probe.

The heating of the probe is accomplished by a wirewound resistor which in turn heats a small thermal mass to which the probe is attached. This arrangement is attached to a linear stepping motor that is controlled by the computer and the appropriate electrical connections are made between the probe and the amplifying and a/d conversion circuits. No feedback has been provided to monitor and control the temperature of the probe. The current passing through the resistive heater is adjusted to provide a probe temperature of 60-65C, and when monitored with a thermocouple this temperature was observed to remain constant to within 2 degrees over the course of several hours.

When the sample is in place and the probe has been heated the computer, translation stage and other instrumentation are turned on. A program is then run that allows the operator to control the motion of the stage and probe. The operator manually positions the stage so that the probe is over is lower and leftmost sampling position. The position readout is zeroed on the stage controller and the manual control program is exited. This control program is included in this appendix and is titled "manmove".

The sampling routine that is next run controls the motion of the stage and the lowering and raising of the probe. The scanning motion is bottom to top, left to right. This routine called "squaresample", first retracts the probe

completely then translates the stage to what it believes to be the center of the sample. The probe is then lowered one step at a time. After each step a voltage reading is taken and compared with one that was taken when the probe was fully retracted. When there is sufficient difference in these values it is assumed the sample has been contacted. The probe is then retracted a fixed number of steps and when it is clear of the sample the stage is moved to the starting position. The probe is then lowered the appropriate number of steps and a number of voltage measurements are taken, averaged and stored in memory. The probe is raised, the stage advanced to the next sample position and the sequence repeats. When sampling is through the user is prompted to a name the data file, which is then written to a data disk.

Several routines are available for providing graphical output of data. The "sqshow" routine uses the limited graphic abilities of the Apple monitor. The screen is divided into square regions representing the data points and each region is then filled in to an extent determined by the measured voltage. Only p-type regions receive any filling, n-type regions appear black. This routine is very quick, but provides limited information. The user supplied parameters are prompted for and are explained in chapter four. The screen can be dumped to the dot-matrix printer if desired.

A multicolor plotter is also available, and is the output device of choice. Though substantially slower, ten to thirty minutes for completion, the resulting plot is much easier to interpret. Several routines are available, the basic difference being the size and number of maps displayed on a single sheet of paper. The program "multisqplot" divides the output paper into six regions

and prompts for individual datafiles and plotting parameters for each region, thus six maps can be displayed. The program "sqplot" prompts for a single datafile with a single set of parameters and produces a map approximately ten centimeters square. The routine "sclsqplot" prompts for a single datafile and set of parameters but then asks for a desired size of the resulting map, and can accommodate maps from two to nineteen centimeters square. The user supplied parameters are again self explanatory and detailed in chapter four. The routines mentioned above are included in this appendix immediately following this page.

program SQSAMPLE

```
10 HIMEM: 36095:D% = 0: DIM C%(5),Q%(5),D%(5)
11 PRINT  CHR$ (4);"BRUN QUICKI/O"
15 HIMEM: 30000
20 DIM ST%(4)
25 MI% = 2
26 DL = 5
27 DS = 10
30 ST%(1) = 9:ST%(2) = 10:ST%(3) = 6:ST%(4) = 5
35 PTR = 30000
40 HOME
70 D$ =  CHR$ (4)
80 POKE 36259,1
90 PRINT D$;"PR#4"
100 PRINT "XB1000H2500A300000YB1000H2500A30000E"
110 PRINT D$;"PR#0"
120 FLASH : PRINT "POSITION STAGE AT LOWERLEFT
CORNER, THEN RETURN": NORMAL
140 INPUT DUMMY$
150 PRINT D$;"PR#4"
160 PRINT "D"
170 P = PTR
180 REM  INITIAL RETRACTION
190 STPS% = 250: GOSUB 850
200 PRINT "YM400KGXM400KG"
210 GOSUB 570: GOSUB 570
220 STPS% = 1
230 & AI0,1: & AI0,1
240 F% = D%(1)
241 DTA% = 20
250 FOR I = 1 TO 250
255 GOSUB 780
260 & AI0,1
270 IF (D%(1) > (F% + DTA%)) OR
(D%(1) < (F% - DTA%)) THEN 310
280 NEXT I
290 PRINT D$;"PR#0"
300 PRINT "EXTENDED WITHOUT CONTACTING SAMPLE"
305 GOTO 920
310 REM  PREPARE TO
320 REM  BACK UP IN PREPARATION FOR LOWER
330 STPS% = DS: GOSUB 850: GOSUB 570
331 GOSUB 570
340 REM   MOVE TO ORIGINAL SPOT
350 PRINT "YM-400KGXM-400KG"
```

```
360 GOSUB 570: GOSUB 570
370 FOR X = 1 TO 25
380 REM   STPS = 20 + DL: GOSUB 780: GOSUB 570
390 FOR Y = 1 TO 25
395 STPS% = DS + DL: GOSUB 780: GOSUB 570
400 GOSUB 600
405 STPS% = DS + DL: GOSUB 850: GOSUB 570
410 PRINT "YM42LG": GOSUB 570
420 SAMPLE = SAMPLE + 2047
430 AD =  INT (SAMPLE -  INT (SAMPLE / 256) * 256)
440 POKE P,AD
450 AD =  INT (SAMPLE / 256)
460 POKE P + 1,AD
470 P = P + 2
480 NEXT Y
490 REM  STPS% = 20 + DL: GOSUB 850: GOSUB 570
500 PRINT "YM-1050KGXM42KG"
510 GOSUB 570: GOSUB 570
520 NEXT X
530 PRINT "XM-1050KG"
540 PRINT D$"PR#0"
550 PRINT "DONE"
560 GOTO 750
570 FOR Z = 1 TO 200
580 NEXT Z
590 RETURN
600 REM  ANALOG SAMPLING ROUTINE
610 REM  THROW AWAY FIRST SAMPLE
620 & AI0
630 FOR Z = 1 TO 5
640 & AI0,Z
650 NEXT Z
660 SUM = 0
670 FOR Z = 1 TO 5
680 SUM = SUM + D%(Z)
690 NEXT Z
700 SAMPLE = SUM / (5)
710 PRINT D$;"PR#0"
720 PRINT X;"  ";Y;"  SAMPLE = ";SAMPLE / 2047
730 PRINT D$;"PR#4"
740 RETURN
750 INPUT "FILE NAME ";NAM$
760 PRINT D$;"BSAVE ";NAM$;",A";
PTR;",L";2 * 25 * 25;",D2"
770 GOTO 920
780 FOR Z = 1 TO STPS%
790 MI% = MI% + 1
```

```
800 IF MI% >  = 5 THEN MI% = 1
810 D% = ST%(MI%)
820 & PO0
830 NEXT Z
840 RETURN
850 FOR Z = 1 TO STPS%
860 MI% = MI% - 1
870 IF MI% = 0 THEN MI% = 4
880 D% = ST%(MI%)
890 & PO0
900 NEXT Z
910 RETURN
920 END
```

program MULTISQPLOT

```
10 HIMEM: 30000
20 DIM P(25,25)
30 DIM PLT(6)
40 DIM NAME$(6)
50 DIM JS(6),FZ(6),ST(6)
60 D$ =  CHR$ (4)
70 T$ =  CHR$ (3)
80 NUM = 0
85 INPUT "LABELS (Y/N, DEFALUT Y) ?";A$
90 NUM = NUM + 1
100 PRINT "INPUTING FOR FILE #";NUM
110 INPUT "FILENAME ? ";NAME$(NUM)
120 IF NAME$(NUM) = "" THEN  GOTO 200
130 INPUT "PLOTNAME ? ";PLT$(NUM)
140 IF PLT$(NUM) = "" THEN PLT$(NUM) = NAME$(NUM)
150 INPUT "JUNCTION SENSITIVITY > ";JS(NUM)
160 INPUT "FALSE ZERO > ";FZ(NUM)
170 INPUT "STEP > ";ST(NUM)
180 IF NUM < 6 THEN  GOTO 90
190 GOTO 210
200 NUM = NUM - 1
210 PRINT D$;"PR#2"
220 PRINT "DI0,1;SI0.2,0.25"
230 PRINT "SP1;PU;"
240 PRINT "PA100,100;"
250 PRINT "PD100,7550,10400,7550,10400,100,100,100;PU;"
260 PRINT "PA600,200;"
269 IF A$ = "N" THEN  GOTO 280
270 PRINT "LBJS = JUNCTION SENSITIVITY
   FZ = FALSE ZERO  S = STEP";T$
280 PRINT "PA900,100;PD900,7550;PU;"
290 PRINT "PA3933,100;PD3933,7550;PU;"
300 PRINT "PA6966,100;PD6966,7550;PU;"
310 PRINT "PA 10000,100;PD10000,7550;PU;"
320 N = 0
330 FOR X = 1 TO 3: FOR Y = 1 TO 2
340 N = N + 1
350 XT = 1100 + (X - 1) * 3033
355 YT = 300 + (Y - 1) * 3725
359 IF A$ = "N" THEN  GOTO 440
360 PRINT "SP1;PA";XT;",";YT;";"
370 PRINT "LBSAMPLE: ";PLT$(N);T$
380 PRINT "PA";XT + 200;",";YT;";"
390 PRINT "LBJS ";JS(N);T$
```

```
400 PRINT "PA";XT + 400;",";YT;";"
410 PRINT "LBFZ = ";FZ(N);T$
420 PRINT "PA";XT + 600;",";YT;";"
430 PRINT "LBS = ";ST(N);T$
440 XC = 2133 + (X - 1) * 3033
450 YC = 300 + (Y - 1) * 3725
460 PRINT "PU;PA";XC;",";YC;";PD;"
470 PRINT "PR1632,0,0,1632,-1632,0,
   0,-1632;PU;PR32,32;"
480 GOSUB 570
490 IF N = NUM THEN  GOTO 510
500 NEXT Y: NEXT X
510 PRINT "PA100,100;SP0;"
520 PRINT D$;"PR#0"
530 INPUT "AGAIN ? (RETURN FOR YES)";B$
540 IF B$ = "" THEN  GOTO 80
550 PRINT D$;"PR#0"
560 GOTO 1030
570 PRINT D$;"BLOAD ";NAME$(N);",D2"
580 PTR = 30000
590 FOR I = 1 TO 25
600 FOR J = 1 TO 25
610 P(I,J) = ( PEEK (PTR) + 256 *
   PEEK (PTR + 1) - 2047) / 2047
620 PTR = PTR + 2
630 NEXT J
640 NEXT I
650 FOR K = 1 TO 2
660 PRINT "SP";K;";PR32,32;"
670 FOR J = 25 TO 1 STEP  - 1
680 FOR I = 1 TO 25
690 C = P(I,J) - FZ(N)
700 IF ((C < FZ(N) AND K = 2) OR
   (C > FZ(N) AND K = 1)) THEN  GOTO 750
710 C =  ABS (C)
720 IF C < JS(N) THEN  GOTO 750
730 IF C > JS(N) + 4 * ST(N) THEN  GOSUB 960: GOTO 750
740 GOSUB 820
750 PRINT "PR0,64;"
760 NEXT I
770 PRINT "PR64,-1600;"
780 NEXT J
790 PRINT "PU;PA";XC + 32;",";YC + 32;"
800 NEXT K
810 RETURN
820 GOSUB 890
830 FOR Z = 1 TO 4
```

```
840 IF C < JS(N) + (Z - 1) * ST(N) THEN  GOTO 870
850 IF C > JS(N) + Z * ST(N) THEN  GOTO 870
860 GOTO 880
870 NEXT Z
880 ON Z GOTO 900,910,910,910
890 PRINT "PR-32,-32;PD0,64,64,
   0,0,-64,-64,0;PU32,32;": RETURN
900 PRINT "PD;PU;": RETURN
910 PRINT "PD-32,0;PU32,-32;PD0,64;PU32,-32;PD-32,0;PU;"
920 IF Z = 2 THEN  RETURN
930 PRINT "PU-32,-32;PD64,64;PU0,-64;PD-64,64;PU32,-32;"
940 IF Z = 3 THEN  RETURN
950 PRINT "PU-16,-16;PD0,32,32,0,0,-32,-32,0;PU16,16;"
955 RETURN
960 PRINT "PU;PR-32,-32;"
970 FOR Z = 1 TO 4
980 PRINT "PD0,64,8,0,0,-64,8,0;"
990 NEXT Z
1000 PRINT "PD0,64;PU-32,-32;"
1010 RETURN
1020 RETURN
1030 END
```

program SQPLOT

```
5 REM ! INTEGER I,J,K
6 HIMEM: 30000
10 D$ =  CHR$ (4)
20 DIM P(25,25)
30 INPUT "FILENAME ? ";A$
40 INPUT "PLOTNAME ? ";N$
50 H = 0
60 S = 10
80 PRINT D$;"BLOAD ";A$;",D2"
100 X = 30000
110 FOR I = 1 TO 25
120 FOR J = 1 TO 25
130 P(I,J) = ( PEEK (X) + 256 *
   PEEK (X + 1) - 2047) / 2047
135 X = X + 2
140 NEXT J
150 NEXT I
170 INPUT "JUNCTION SENSITIVITY ";L
180 INPUT "FALSE ZERO ";H
190 INPUT "STEP ? ";DD
200 PRINT D$;"PR#2"
210 PRINT "SI0.2,0.25;"
220 PRINT "SP1;PA545,939;DI0,1;LBSAMPLE :  ";N$; CHR$ (3)
230 PRINT "PA715,939;LBSQUARE SIZE :  ";S;" mm"; CHR$ (3)
280 PRINT "PA3725,2414;PD3725,5414,6725,
   5414,6725,2414,3725,2414;PU;"
285 FOR K = 1 TO 2
290 PRINT "DI;PA3785,2474;SP";K;";"; CHR$ (3)
300 FOR J = 25 TO 1 STEP  - 1
310 FOR I = 1 TO 25
320 C = P(I,J) - H
324 IF ((C < H AND K = 2) OR (C > H AND K = 1))
   THEN  GOTO 360
326 C =  ABS (C)
330 IF C < L THEN  GOTO 360
340 IF C > L + 4 * DD THEN  GOSUB 540: GOTO 360
350 GOSUB 420
360 PRINT "PR0,120;"
370 NEXT I
380 PRINT "PR120,-3000;"
390 NEXT J
395 NEXT K
400 GOSUB 600
410 PRINT D$;"PR#0": GOTO 3900
```

```
420 GOSUB 470
430 FOR Z = 1 TO 4
440 IF C > L + (Z - 1) * DD AND C < L + Z * DD THEN  GOTO 460
450 NEXT Z
460 ON Z GOTO 480,490,490,490
470 PRINT "PR-60,-60;PD0,120,120,0,0,-120,
   -120,0;PU60,60;": RETURN
480 PRINT "PD;PU;": RETURN
490 PRINT "PD-60,0;PU60,-60;PD0,120;PU60,-60;PD-60,0;PU;"
500 IF Z = 2 THEN  RETURN
510 PRINT "PU-60,-60;PD120,120;PU0,-120;PD-120,120;PU60,-60;"
520 IF Z = 3 THEN  RETURN
530 PRINT "PU-30,-30;PD0,60,60,0,0,-60,-60,
   0;PU30,30;": RETURN
540 PRINT "PU;PR-60,-60;"
550 FOR Z = 1 TO 6
560 PRINT "PD0,120,10,0,0,-120,10,0;"
570 NEXT Z
580 PRINT "PD0,120;PU-60,-60;"
590 RETURN
600 REM  MORE PRINTED INFO GOES HERE
605 PRINT "SP1;"
610 PRINT "DI0,1;PA9000,625;LBJUNCTION
   SENSITIVITY = ";L; CHR$ (3)
620 PRINT "PA9200,625;LBFALSE ZERO = ";H; CHR$ (3)
625 PRINT "PA9400,625;LBSTEP = ";DD; CHR$ (3)
630 PRINT "SP0;PA0,0;"
640 RETURN
3900 INPUT "AGAIN ? (RETURN FOR YES)";B$
3910 IF B$ = "" THEN  GOTO 170
3920 END
```

program MANMOVE

```
1 HIMEM: 36095:D% = 0: DIM C%(5),Q%(5),D%(5)
2 PRINT  CHR$ (4);"BRUN QUICKI/O"
5 DIM ST%(4)
6 ST%(1) = 5:ST%(2) = 6:ST%(3) = 10:ST%(4) = 9
10 HOME
15 D$ =  CHR$ (4)
20 PRINT D$;"PR#4"
25 PRINT "XB1000H1000A100000YB1000H1000A100000"
30 PRINT D$;"PR#0"
35 PRINT "36  PRINT "SPACE BAR STOPS MOTION"
37 PRINT "RETURN RAISES AND LOWERS PROBE"
38 PRINT "HIT ESC KEY TO QUIT"
40 PRINT D$;"PR#4"
50 X =  PEEK ( - 16384)
60 IF X <  = 127 GOTO 50
70 POKE  - 16368,0
75 IF X = 155 THEN  PRINT "XY
80 IF X = 160 THEN  PRINT "XY
90 IF X = 136 THEN  PRINT "XR": GOTO 50
100 IF X = 149 THEN  PRINT "XQ": GOTO 50
110 IF X = 138 THEN  PRINT "YR": GOTO 50
120 IF X = 139 THEN  PRINT "YQ": GOTO 50
124 IF X = 177 GOTO 300
126 IF X = 178 GOTO 400
130 IF X <  > 141 THEN  GOTO 50
135 PRINT "
170 GOTO 50
200 PRINT D$;"PR#0"
210 GOTO 500
300 FOR I = 1 TO 63
310 FOR Z = 4 TO 1 STEP  - 1
320 D% = ST%(Z): & PO0
322 X =  PEEK ( - 16384)
323 IF X >  = 127 THEN  POKE  - 16368,0: GOTO 50
330 NEXT Z: NEXT I
340 GOTO 50
400 FOR I = 1 TO 63
410 FOR Z = 1 TO 4
420 D% = ST%(Z): & PO0
422 X =  PEEK ( - 16384)
423 IF X >  = 127 THEN  POKE  - 16368,0: GOTO 50
430 NEXT Z: NEXT I
440 GOTO 50
500 END
```

program SCLSQPLOT

```
10 REM ! INTEGER I,J,K
20 HIMEM: 30000
30 D$ =  CHR$ (4)
40 DIM P(25,25)
50 INPUT "LABELS (Y/N DEFAULT Y) ? ";Q$
60 INPUT "FILENAME ? ";A$
70 INPUT "PLOTNAME ? ";N$
75 IF N$ = "" THEN N$ = A$
80 INPUT "SQUARE SIZE (CM) MAX IS 19.5 ? ";SQSZ
90 NMPX = SQSZ * 10 / 0.025
100 TPX =  INT (NMPX / 25)
105 IF TPX = NPX / 25 THEN CLSZ = TPX: GOTO 130
109 REM
110 IF (TPX) * 25 > 7800 THEN TPX = TPX - 1: GOTO 109
114 CLSZ = TPX
130 IF  INT (CLSZ / 2) <  > CLSZ / 2 THEN CLSZ = CLSZ - 1
140 PRINT "NEAREST SIZE IS ";CLSZ * 25 * .025 / 10;" CM"
150 INPUT "IS THIS OKAY? (Y/N DEFAULT Y)";ANS$
160 IF ANS$ = "N" THEN  GOTO 80
170 H = 0
180 WIDTH = CLSZ * 25
190 S = 10
200 PRINT D$;"BLOAD ";A$;",D2"
210 X = 30000
220 FOR I = 1 TO 25
230 FOR J = 1 TO 25
240 P(I,J) = ( PEEK (X) + 256 *  PEEK (X + 1) - 2047) / 2047
250 X = X + 2
260 NEXT J
270 NEXT I
280 INPUT "JUNCTION SENSITIVITY ";L
290 INPUT "FALSE ZERO ";H
300 INPUT "STEP ? ";DD
310 REM   GOTO 330
320 PRINT D$;"PR#2"
330 PRINT "SI0.2,0.25;"
340 PRINT "SP1;"
350 IF Q$ = "N" THEN  GOTO 380
360 PRINT "PA545,739,DI0,1;LBSAMPLE :  ";N$; CHR$ (3)
370 PRINT "PA715,739;LBSQUARE SIZE :  ";S;" mm"; CHR$ (3)
380 TCLSZ =  INT (CLSZ / 3)
390 HCLSZ = CLSZ / 2
400 PRINT "PU;PA";5182 - WIDTH / 2;",";3981 -
   WIDTH / 2;";"; CHR$ (3)
```

```
410 PRINT "PD;PR0,";WIDTH;",";WIDTH;",0,0,-";
   WIDTH;",-";WIDTH;",0;PU;"; CHR$ (3)
420 FOR K = 1 TO 2
430 PRINT "DI;PA";5182 - (WIDTH - CLSZ) / 2;",";
   3981 - (WIDTH - CLSZ) / 2;";SP";K;";"; CHR$ (3)
440 FOR J = 25 TO 1 STEP  - 1
450 FOR I = 1 TO 25
460 C = P(I,J)
470 IF ((C < H AND K = 2) OR (C > H AND K = 1))
   THEN  GOTO 520
480 C =  ABS (C)
490 IF C < L THEN  GOTO 520
500 IF C > L + 4 * DD THEN  GOSUB 770: GOTO 520
510 GOSUB 590
520 PRINT "PR0,";CLSZ;";"; CHR$ (3)
530 NEXT I
540 PRINT "PR";CLSZ;",-";WIDTH;";"; CHR$ (3)
550 NEXT J
560 NEXT K
570 GOSUB 840
580 PRINT D$;"PR#0": GOTO 920
590 GOSUB 640
600 FOR Z = 1 TO 4
610 IF C > H + L + (Z - 1) * DD AND C <
   H + L + Z * DD THEN  GOTO 630
620 NEXT Z
630 ON Z GOTO 650,660,660,660
640 PRINT "PR-";HCLSZ;",-";HCLSZ;";PD0,";
   CLSZ;",";CLSZ;",0,0,-";CLSZ;",-";CLSZ;",0;PU";
   HCLSZ;",";HCLSZ;";"; CHR$ (3): RETURN
650 PRINT "PD;PU;": RETURN
660 PRINT "PD-";HCLSZ;",0;PU";HCLSZ;",-";
   HCLSZ;";PD0,";CLSZ;";PU";HCLSZ;",-";HCLSZ;";
   PD-";HCLSZ;",0;PU;"; CHR$ (3)
670 IF Z = 2 THEN  RETURN
680 PRINT "PU-";HCLSZ;",-";HCLSZ;";PD";CLSZ;
   ",";CLSZ;";PU0,-";CLSZ;";PD-"CLSZ;",";CLSZ;
   ";PU";HCLSZ;",-";HCLSZ; CHR$ (3)
690 IF Z = 3 THEN  RETURN
700 PRINT "PU-";TCLSZ;",-";TCLSZ;";"; CHR$ (3)
710 TMP = TCLSZ + 10
720 TMP = TMP - 10
725 T = 2 * TMP
730 PRINT "PD0,";T;",";T;",0,0,-";T;",-";T;",0;"; CHR$ (3)
740 IF TMP >  = 10 THEN  PRINT "PR10,10;": GOTO 720
750 PRINT "PR";TMP;",";TMP;";PU;"; CHR$ (3)
760 RETURN
```

```
410 PRINT "PD;PR0,";WIDTH;",";WIDTH;",0,0,-";
   WIDTH;",-";WIDTH;",0;PU;"; CHR$ (3)
420 FOR K = 1 TO 2
430 PRINT "DI;PA";5182 - (WIDTH - CLSZ) / 2;",";
   3981 - (WIDTH - CLSZ) / 2;";SP";K;";"; CHR$ (3)
440 FOR J = 25 TO 1 STEP  - 1
450 FOR I = 1 TO 25
460 C = P(I,J)
470 IF ((C < H AND K = 2) OR (C > H AND K = 1))
   THEN  GOTO 520
480 C =  ABS (C)
490 IF C < L THEN  GOTO 520
500 IF C > L + 4 * DD THEN  GOSUB 770: GOTO 520
510 GOSUB 590
520 PRINT "PR0,";CLSZ;";"; CHR$ (3)
530 NEXT I
540 PRINT "PR";CLSZ;",-";WIDTH;";"; CHR$ (3)
550 NEXT J
560 NEXT K
570 GOSUB 840
580 PRINT D$;"PR#0": GOTO 920
590 GOSUB 640
600 FOR Z = 1 TO 4
610 IF C > H + L + (Z - 1) * DD AND C <
   H + L + Z * DD THEN  GOTO 630
620 NEXT Z
630 ON Z GOTO 650,660,660,660
640 PRINT "PR-";HCLSZ;",-";HCLSZ;";PD0,";
   CLSZ;",";CLSZ;",0,0,-";CLSZ;",-";CLSZ;",0;PU";
   HCLSZ;",";HCLSZ;";"; CHR$ (3): RETURN
650 PRINT "PD;PU;": RETURN
660 PRINT "PD-";HCLSZ;",0;PU";HCLSZ;",-";
   HCLSZ;";PD0,";CLSZ;";PU";HCLSZ;",-";HCLSZ;";
   PD-";HCLSZ;",0;PU;"; CHR$ (3)
670 IF Z = 2 THEN  RETURN
680 PRINT "PU-";HCLSZ;",-";HCLSZ;";PD";CLSZ;
   ",";CLSZ;";PU0,-";CLSZ;";PD-"CLSZ;",";CLSZ;
   ";PU";HCLSZ;",-";HCLSZ; CHR$ (3)
690 IF Z = 3 THEN  RETURN
700 PRINT "PU-";TCLSZ;",-";TCLSZ;";"; CHR$ (3)
710 TMP = TCLSZ + 10
720 TMP = TMP - 10
725 T = 2 * TMP
730 PRINT "PD0,";T;",";T;",0,0,-";T;",-";T;",0;"; CHR$ (3)
740 IF TMP >  = 10 THEN  PRINT "PR10,10;": GOTO 720
750 PRINT "PR";TMP;",";TMP;";PU;"; CHR$ (3)
760 RETURN
```

```
770 TMP = HCLSZ + 10
780 PRINT "PU-";TMP - 10;",-";TMP - 10;";"; CHR$ (3)
790 TMP = TMP - 10
795 T = 2 * TMP
800 PRINT "PD0,";T;",";T;",0,0,-";T;",-";T;",0;"; CHR$ (3)
810 IF TMP > = 10 THEN PRINT "PR10,10;": GOTO 790
820 PRINT "PR";TMP;",";TMP;";PU;"; CHR$ (3)
830 RETURN
840 REM MORE PRINTED INFO GOES HERE
850 IF Q$ = "N" THEN GOTO 900
860 PRINT "SP1;"
870 PRINT "DI0,1;PA9000,625;LBJUNCTION
   SENSITIVITY = ";L; CHR$ (3)
880 PRINT "PA9200,625;LBFALSE ZERO = ";H; CHR$ (3)
890 PRINT "PA9400,625;LBSTEP = ";DD; CHR$ (3)
900 PRINT "SP0;PA0,0;"
910 RETURN
920 INPUT "AGAIN ? (RETURN FOR YES)";B$
930 IF B$ = "" THEN GOTO 280
940 END
```

BIOGRAPHICAL NOTE

The author was born on 21 June 1961, in Ketchikan, Alaska. In 1967 he moved to Anacortes, Washington and attended public schools, graduating from Anacortes Senior High School in 1979. He then entered Lewis and Clark College in Portland, Oregon where he received two Bachelor of Arts degrees (Physics and Mathematics) in June 1983.

In April 1983 the author accepted a teaching assistantship in the Physics Department at the University of Utah, and entered graduate school there in September 1983. After two quarters of graduate coursework he left the University of Utah and returned to Portland, Oregon to accept employment with the Advanced Research Laboratory at Tektronix Incorporated. The author was employed by Tektronix until May 1985, when he left the company, intending to return to graduate school.

In September 1985 the author began study at the Oregon Graduate Center where he completed the requirements for the degree Doctor of Philosophy (Applied Physics) in December 1988.

The author has been married since July 1987 to Sara (neé Noble) Moore. The couple has no children, no dogs and no cats.

He is leaving the Oregon Graduate Center to accept a National Research Council Postdoctoral Fellowship in Washington D.C. at the Naval Research Laboratory.